SIMULATING THE UNIVERSE: NONLINEAR FORMATION AND EVOLUTION OF COSMIC
STRUCTURE

by

Jeffrey David Emberson

A thesis submitted in conformity with the requirements
for the degree of Doctor of Philosophy
Graduate Department of Astronomy and Astrophysics
University of Toronto

Abstract

Simulating the Universe: Nonlinear Formation and Evolution of Cosmic Structure

Jeffrey David Emberson
Doctor of Philosophy
Graduate Department of Astronomy and Astrophysics
University of Toronto
2016

In this thesis, we harness the power of modern scientific computing to explore the formation and evolution of cosmological structure in a wide variety of astrophysical scenarios. We explore the nonlinear dynamics associated with the interplay between cold dark matter (CDM), baryons, ionizing radiation, and cosmic neutrinos, within regimes where analytic calculations necessarily fail. We begin by providing an overview of structure formation and its connections to the fields of study considered here: the epoch of reionization, galactic substructure evolution, and cosmic neutrinos. We then present a rigorous numerical convergence study of cosmological hydrodynamics simulations post-possessed with radiative transfer to study the impact of small-scale absorption systems within the intergalactic medium (IGM) during the onset of reionization. We present converged statistics of the IGM on smaller scales and earlier times than previously considered. Moreover, we provide strict resolution limits for hydrodynamic simulations to properly resolve the unheated IGM. Next we study the infall and dynamical evolution of CDM halos in a galactic host. We find the behaviour of low-mass subhalos is qualitatively different than previously described for high-mass subhalos. In particular, the evolution of low-mass subhalos, with masses less than 0.1 per cent that of the host, is mainly driven by their concentration. This presents an opportunity to use concentration as a predictive indicator of substructure evolution. We finish this thesis with an investigation of a recently proposed method for constraining individual neutrino mass from cosmological observations. Such a detection depends on the ability to reconstruct the CDM-neutrino relative velocity, which we show can be accomplished using linear transformations of an observed galaxy field. Based on this, we perform the world's largest cosmological N-body simulation and present preliminary results for the observational prospects of cosmic neutrinos.

To my parents and grandparents,
my teachers in life.

Acknowledgements

This thesis represents the culmination of my Ph.D. research at the University of Toronto. The work presented here would not have been possible without the thoughtful guidance and support of my supervisor, Ue-Li Pen, and co-supervisor, Marcelo Alvarez. It has been an absolute pleasure working closely with the two of you over the past five years. I would like to extend my gratitude for the tremendous patience and insight you have shared with me. I have inherited a wealth of knowledge and skills from this experience.

There were many people here that made this journey an unforgettable one. I would especially like to thank my astronomy cohort, Etsuko Mieda, Yevgeni Kissin, and Charles Zhu. I cherish the friendship we have developed over our time here together. Thank you for helping me pass the quals. I would also like to thank my academic brothers, Joachim Harnois-Déraps, Derek Inman, and Hao-Ran Yu, for always offering help and sharing your knowledge.

I could not have made it this far without the continual support of my family and friends. Mom and dad, you were there when I started kindergarten, and may now finally see me finish school. Thank you for always offering emotional (and financial) assistance and for the infinity of other things you do for me. Thank you to my siblings, Jenny, Josh, Jake, and Joanne, for helping to shape the person I am today. Nana, thank you for being my best, best friend. Thank you to the rest of my family and friends for your motivation and support.

Finally, I would like to thank my wife, Katelyn. You have been a source of strength and support over the past decade. Thank you for your patience and enthusiastic willingness to help me through this. I look forward to continuing this journey in life with you.

Contents

List of Tables

List of Figures

Chapter 1

Introduction

Astronomy is considered to be the oldest science known to humankind. Ancient civilizations across the globe gazed into the night sky with a sense of wonder and curiosity of our place in the cosmos. Since then we have developed an increasingly sophisticated picture of our surrounding universe. The modern cosmological picture is that of a universe starting with a big bang some 14 billion years ago. The primordial soup of fundamental particles in the early universe evolved over time into an intricate network of cosmological structure containing an endless number of planets, stars, and galaxies. There is even more than meets the eye: beneath the network of luminous sources hides a dark sector of the universe. We now know of the existence of dark matter, a mysterious form of matter that dominates the mass of galaxies, and of dark energy, that drives an accelerated expansion of the cosmos. The modern picture of cosmology seems to become more intriguing the deeper we probe the universe.

We are now in the era of precision cosmology where technological advances allow us to understand the nature of the universe at an increasing pace. An assortment of ground- and space-based telescopes have measured the composition of the current universe in extreme detail. Dark energy dominates the universal energy budget at a level of 70% with dark matter coming second at a level of 25%. Regular baryonic matter, making up the familiar elements on the periodic table, constitutes only 5% of the universe! Upcoming observations that plan to map the three-dimensional structure around us will further refine our understanding of the universe. On the theoretical side, much has been learned in recent decades due to advancements in scientific computing. High performance supercomputers continue to represent an indispensable tool in scientific discovery, enabling complex computations that would otherwise remain beyond our reach. Of particular interest here are cosmological simulations that trace the nonlinear dynamics of structure formation within regimes where analytic calculations fail.

This thesis is broadly concerned with the nonlinear formation and evolution of cosmic structure. This is studied in the context of various astrophysical scenarios including the epoch of reionization, galactic substructure evolution, and cosmic neutrinos. The underlying connection between each of the research projects presented here is the the study of nonlinear structure formation with the aid of cosmological simulations. In this Chapter, we provide the reader

with an introduction to the field of cosmological structure formation. Afterward, we provide an overview of each of the astrophysical scenarios studied in this thesis.

1.1 Cosmological Structure Formation

This section provides an overview of cosmological structure formation. This material provides an underlying framework of the modern picture of cosmology and is thus well documented in standard text books (e.g., Peebles, 1980; Dodelson, 2003; Schneider, 2006).

We begin with the cosmological principle, which asserts that the universe is homogeneous and isotropic on large scales. This assumption is empirically justified by measurements of the cosmic microwave background (CMB) and large-scale distribution of galaxies. We also know from redshifted light of nearby galaxies that the universe is expanding. The notion of distance in such a universe is specified by the Friedmann-Lemîatre-Robertson-Walker (FLRW) metric:

$$ds^2 = -dt^2 + a(t)^2 \left[dr^2 + S_k(r)^2 \left(d\theta^2 + \sin^2\theta d\phi^2 \right) \right], \tag{1.1}$$

where (r, θ, ϕ) represent a comoving spherical coordinate system and we have chosen units such that the speed of light $c = 1$. The function $S_k(r)$ depends on the spatial curvature of the universe; current evidence suggests a spatially flat universe for which $S_k(r) = r$. The scale factor, $a(t)$, describes the compression or expansion of the coordinate system with time and is normalized such that $a(t_0) = 1$ at the present time. The scale factor is related to the cosmological redshift, $a = (1 + z)^{-1}$, with z denoting the relative change in the wavelength of emitted light observed from a distant object due to cosmic expansion.

The scale factor provides information on the expansion history of the universe. General relativity can be used to relate $a(t)$ to the energy content of the universe based on the FLRW metric. For a flat universe, this yields expressions for the first and second derivatives of a, collectively known as the Friedmann equations:

$$\left(\frac{\dot{a}}{a} \right)^2 = \frac{8\pi G}{3} \rho_{\text{tot}},$$
$$\frac{\ddot{a}}{a} = -\frac{4\pi G}{3} \left(\rho_{\text{tot}} + 3p_{\text{tot}} \right), \tag{1.2}$$

where ρ_{tot} and p_{tot} are the total energy density and pressure summed over all constituents of the universe. We can further derive an expression for energy conservation by substituting the derivate of the first Friedmann equation into the second equation:

$$\dot{\rho}_{\text{tot}} = -3\frac{\dot{a}}{a}(\rho_{\text{tot}} + p_{\text{tot}}). \tag{1.3}$$

We live in a universe containing contributions from radiation (ρ_r), non-relativistic matter (ρ_m), and dark energy (ρ_Λ). Each of these components has an equation of state, $p = w\rho$, where w

is 1/3, 0, and -1 for radiation, non-relativistic matter, and dark energy, respectively. Plugging this form into equation (1.3) shows that $\rho \propto a^{-\alpha}$ where $\alpha = 3(1 + w)$. Hence, radiation and non-relativistic matter evolve as $\rho_r \propto a^{-4}$ and $\rho_m \propto a^{-3}$, respectively, while ρ_Λ is constant in time. We may rearrange the first Friedmann equation to define a critical density:

$$\rho_{\text{crit}} = \frac{3H^2}{8\pi G} \tag{1.4}$$

In this expression we have defined the Hubble parameter, $H \equiv \dot{a}/a$, which we parameterize with the dimensionless number h such that $H_0 = H(t_0) = 100h$ km Mpc^{-1} s^{-1} at the current time. It is often convenient to normalize the energy density of each species to the present-day critical density. In this case, we define the quantity $\Omega_i \equiv \rho_i/\rho_{\text{crit},0}$. The sum over Ω_i is unity for the flat universe assumed here.

With this framework in hand, we may describe the formation of cosmological structure. Our goal is to model the evolution of density perturbations under the influence of gravity. In many cases, it is sufficient to assume a universe containing only pressure-less dust representing the dark matter component of the universe. The standard approach is to model the evolution in density, ρ, and proper velocity, $\mathbf{v} = d\mathbf{r}/dt$, using the fluid approximation for which we have three coupled differential equations:

$$\begin{aligned}
\frac{\partial \rho}{\partial t} + \nabla \cdot (\rho \mathbf{v}) &= 0, \\
\frac{\partial \mathbf{v}}{\partial t} + (\mathbf{v} \cdot \nabla)\mathbf{v} &= -\frac{\nabla P}{\rho} - \nabla \Phi, \\
\nabla^2 \Phi &= 4\pi G\rho.
\end{aligned} \tag{1.5}$$

These are the continuity, Euler, and Poisson equations, describing mass conservation, momentum conservation, and self-gravity of the fluid, respectively. In the case of pressure-less dust, we set the ∇P term in the Euler equation to zero.

In general, equations (1.5) cannot be solved analytically. However, under a certain set of assumptions, we can solve them exactly using linear perturbation theory. We begin by with a homogeneous universe of background density, $\bar{\rho}$, and append small perturbations, $\delta \equiv \rho/\bar{\rho} - 1$. Next, we switch to a comoving coordinate system, $\mathbf{x} = \mathbf{r}/a$, and transform derivatives accordingly. We consider evolution in only the small perturbations, δ, and its potential, $\nabla^2\hat{\Phi}$. Applying these changes to equations (1.5) and keeping only terms of linear order in δ and $\dot{\mathbf{x}}$ yields:

$$\begin{aligned}
\frac{\partial \delta}{\partial t} + \nabla \cdot \dot{\mathbf{x}} &= 0, \\
\ddot{\mathbf{x}} + 2\frac{\dot{a}}{a}\dot{\mathbf{x}} &= \frac{\nabla \hat{\Phi}}{a^2}, \\
\frac{\nabla^2 \hat{\Phi}}{a^2} &= 4\pi G\bar{\rho}\delta.
\end{aligned} \tag{1.6}$$

These equations can be solved to a more succinct form:

$$\ddot{\delta} + 2\frac{\dot{a}}{a}\dot{\delta} = 4\pi G\bar{\rho}\delta. \tag{1.7}$$

This expression contains neither partial derivatives with respect to spatial coordinate nor co-efficients that depend on $\mathbf{x}$. As such, we can factorize the spatial and temporal components so that we have solutions of the form $\delta(t) = D(t)\delta_0$. There are two such solutions, one for which δ grows in time, and one for which it decays. For cosmological purposes, the decaying solution becomes subdominant at late times and can be ignored. For the growing solution, we call the function $D(t)$ the linear growth factor.

We can use this result to describe the growth of density perturbations over time. In this case, it is useful to speak in terms of the power spectrum, $P(k)$, defined in Fourier space as

$$P(k) = \langle |\delta(k)|^2 \rangle. \tag{1.8}$$

The power spectrum provides a complete statistical description of the density field for the Gaussian random fields predicted from basic inflationary models. In linear theory, Fourier modes evolve independently and we say that $P(k,t)$ is related to some initial power spectrum, $P_0(k) = P(k, t = 0)$, convolved with the linear growth factor and transfer function:

$$P(k,t) = D^2(t)T^2(k)P_0(k). \tag{1.9}$$

The transfer function, $T(k)$, encodes the transformation of the initial power spectrum based on scale-dependent growth between horizon crossing and matter-radiation equality. Inflationary models predict a primordial power spectrum, $P_0 \propto k^{n_s}$, with power-law index $n_s \sim 1$.

We have used linear perturbation theory to derive an analytic solution to the growth of cosmological structure. However, this solution becomes increasingly inaccurate as δ continues to grow and completely breaks down when $\delta \gg 1$. At the present epoch, this condition is already broken on the scale of galaxy clusters (~ 5 Mpc) and is even worse on smaller scales. We must thus rely on methods outside of linear perturbation theory if we hope to provide an accurate picture of cosmological structure formation on all scales. This is conventionally achieved using cosmological N-body simulations that solve the fluid equations numerically.

The N-body setup begins with an initial realization of the matter density field. The idea is to generate initial conditions at sufficiently early time that linear theory is valid and equation (1.9) can be used to create a realization of the cosmology specified by the functions $D(t)$, $T(k)$, and $P_0(k)$. This is achieved in Fourier space by sampling $\delta(\mathbf{k}) = n(\mathbf{k})\sqrt{P(k)}$ where $n(\mathbf{k})$ is a random white noise field satisfying $\langle |n(k)|^2 \rangle = 1$. This result is inverse Fourier transformed to provide the density field in real space. The standard approach is to then perturb N-body particles from an uniform lattice based on the gravitational potential generated by the sampled density field. Particles are subsequently evolved forward in time using a repetitive process of computing

gravity, moving particles, computing gravity, etc. The gravitational force is computed using some combination of particle-particle, particle-mesh, and tree algorithms (see, e.g., Hockney & Eastwood, 1988).

Cosmological N-body simulations provide an invaluable tool for studying the nonlinear growth of collisionless dark matter. In many cases, however, it is important to include the physics of collisional baryonic gas. This is accomplished with hydrodynamic simulations that discretize the baryonic fluid into either volume elements (e.g., Bryan et al., 2014) or smoothed particles (e.g., Springel, 2005). In this case, the fluid equations are supplemented with the first law of thermodynamics describing the internal energy, u, of the gas:

$$\frac{\partial u}{\partial t} + (\mathbf{v} \cdot \nabla)u = -\frac{P}{\rho}\nabla \cdot \mathbf{v} - \frac{\Lambda(u, \rho)}{\rho}. \tag{1.10}$$

Here the function Λ describes external sinks and sources of thermal energy. The gas is modelled as an ideal gas with equation of state, $P = (\gamma - 1)\rho u$, where γ is the adiabatic exponent. Modern hydrodynamic simulations often contain prescriptions for various baryonic physics including radiative cooling and heating, star formation, and feedback from supernovae and/or active galactic nuclei.

1.2 The Epoch of Reionization

The epoch of cosmic reionization represents a major evolutionary transition in the physical state of the universe. This period was marked by the formation of the first luminous sources, putting an end to the cosmological dark ages, and initiating a process whereby ionizing photons gradually transformed the intergalactic medium (IGM) from being mostly neutral to predominately ionized. This epoch is aptly named as reionization reverts the matter content of the universe to the ionized form that existed after the big bang and up to the epoch recombination. The progression of reionization is strongly driven by this history of ionizing sources within the early universe. Studying the epoch of reionization thus presents the opportunity to learn about the first cosmic structures and how they eventually relate to the present-day universe.

Observational constraints on the duration of reionization place it within the redshift range $6 \lesssim z \lesssim 15$. The lower bound comes from the absence of the Gunn-Peterson trough (Gunn & Peterson, 1965) in the absorption spectra of high-redshift quasars (Fan et al., 2006), indicating that the IGM is highly ionized at lower redshift. The upper bound arises from measurements of the optical depth to Thomson scattering, with $\tau \sim 0.09$ from the Wilkinson Microwave Anisotropy Probe (WMAP) suggesting the IGM had already been significantly ionized by $z \sim 10$ (Hinshaw et al., 2013). Note, however, that recent measurements of $\tau \sim 0.07$ from the Planck satellite may push this upper bound to lower redshift (Planck Collaboration et al., 2015). In either case, the Thomson scattering optical depth provides only an integral constraint on the ionization history, so a wide variety of reionization morphologies are possible within current
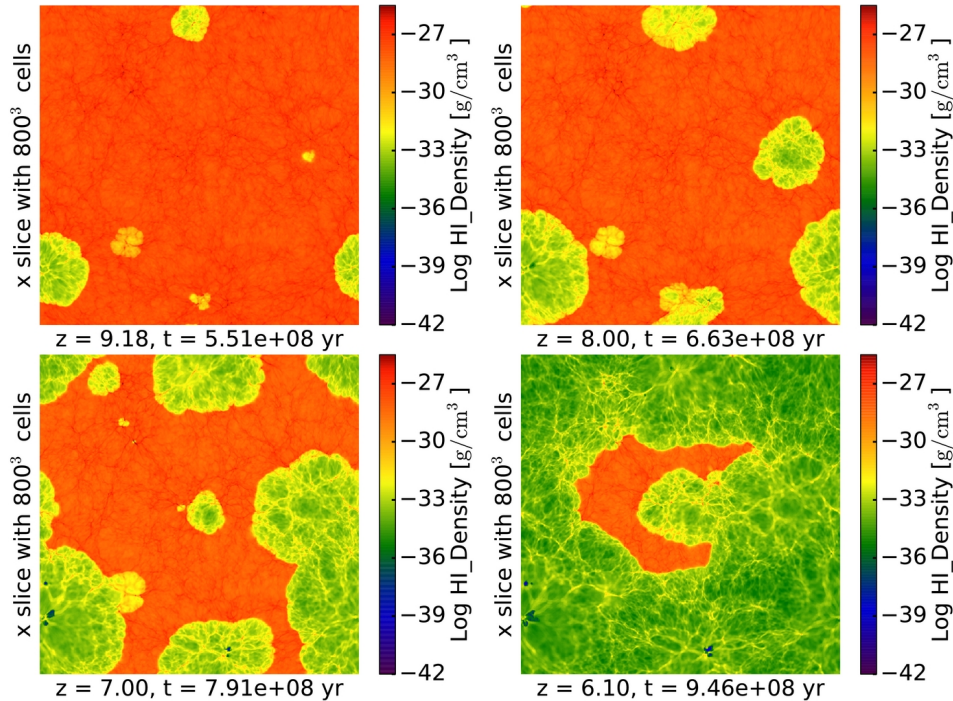
Figure 1.1: Image from So et al. (2014) showing neutral hydrogen density slices at redshifts $z = 9.18$, 8.00, 7.00, and 6.10 (clockwise from top left) from a hydrodynamic plus radiative transfer simulation of reionization. This image depicts the evolutionary progression of reionization that starts with individual H II regions around luminous sources that grow, overlap, and eventually percolate all space. The simulation box of width 20 Mpc box was resolved with 800^3 mesh cells; slices are one cell thick.

limits. Upcoming 21 cm observations (e.g., Mesinger et al., 2015) that directly trace the three-dimensional distribution of neutral hydrogen in the universe offer the most promising prospect to shed light on the detailed evolution of reionization.

In the meantime, theorists have made progress on understanding the process of reionization using both semi-analytical (e.g., Miralda-Escudé et al., 2000; Furlanetto et al., 2004; Zahn et al., 2005; Mesinger & Furlanetto, 2007; Geil & Wyithe, 2008; Alvarez et al., 2009; Santos et al., 2010; Battaglia et al., 2013) and numerical (e.g., Gnedin, 2000; Ciardi et al., 2003; Iliev et al., 2006; Trac et al., 2008; Finlator et al., 2009; Aubert & Teyssier, 2010; So et al., 2014) treatments. The general picture of reionization begins with the first luminous sources forming in rare overdensity peaks in the matter density field. Ionizing photons propagate outward from each source, first clearing through the neutral hydrogen associated with their own interstellar medium (ISM), then escaping into the surrounding IGM. This establishes a patchy network of cosmological H II regions surrounding each source. Over time, individual H II regions grow in size and eventually overlap to percolate all space so that any point in the IGM is exposed to multiple sources of ionizing radiation. During this time, the volume fraction of ionized gas in the IGM approaches unity, marking the completion of reionization. We depict this process visually in Figure 1.1, showing snapshots of the neutral hydrogen density field from the hydrodynamic

plus radiative transfer simulation of So et al. (2014).

In a more rigorous yet simple treatment, reionization can be thought of as a balance between the sources and sinks of ionizing photons (see, e.g., Kaurov & Gnedin, 2014). In particular, suppose we denote N_i as the number of ionizations per hydrogen atom required to keep some volume of the universe ionized. The condition for reionization to occur is:

$$N_\gamma = N_i, \tag{1.11}$$

where N_γ is the number of ionizing photons per hydrogen atom present within that volume. In the naive situation where hydrogen recombinations do not occur, $N_i = 1$. With recombinations,

$$
\begin{aligned}
N_i(t) &= 1 + \int_0^t \mathcal{R} dt \\
&= 1 + \frac{1}{N_H} \int_0^t \alpha \langle n_e n_{HII} \rangle dt,
\end{aligned}
\tag{1.12}
$$

where the recombination rate, $\mathcal{R} = \alpha n_e n_{HII}$, depends on the product of the recombination coefficient, α, with the number density of electrons, n_e, and ionized hydrogen, n_{HII}. In equation (1.12) angle brackets denote volume averages and N_H represents the total number of hydrogen nuclei in the region. Assuming $n_e = n_{HII}$, the condition for reionization becomes:

$$N_\gamma = 1 + \frac{1}{N_H} \int_0^t \alpha \langle n_e^2 \rangle dt. \tag{1.13}$$

The left-hand side of equation (1.13) represents the *source* term which can be described by the spatial clustering and spectral energy distribution of luminous sources. The right-hand side denotes the *sink* term which is dominated by dense absorption systems with enhanced recombination rates in the IGM (Miralda-Escudé et al., 2000). These absorption systems are able to consume ionizing radiation from nearby sources while remaining neutral. As a result, they act to impede the growth of cosmological H II regions, thus acting as important obstacles to the percolation phase of reionization (Gnedin & Fan, 2006; Choudhury et al., 2009; Alvarez & Abel, 2012). From this simple description, it is easy to see that any model of reionization should properly take into account *both* the sources and sinks of ionizing photons.

The distribution of absorption systems within the IGM is intimately connected to structure formation. The smallest scale at which gaseous structures form is set by the cosmological Jeans scale. This is defined as the scale below which pressure gradient forces of the gas resist gravitational collapse. For an *unheated* IGM, the Jeans scale occurs at $k_J \sim 1$ kpc with a corresponding Jeans mass of $M_J \sim 10^4\ M_\odot$ setting the minimum mass threshold for gaseous structure (see, e.g., Barkana & Loeb, 2001). Low-mass halos forming near the Jeans mass are often referred to as minihalos (MHs) and are too small to form stars via hydrogen line cooling. Instead, molecular hydrogen cooling is possible, though this will become suppressed once the first luminous sources output enough ultraviolet (UV) radiation to dissociate molecular

hydrogen (Haiman et al., 2000). Hence, we expect a collection of dark, dense MHs within the IGM that act as important sinks of ionizing photons. However, MHs are not expected to survive forever due to photoheating from ionizing sources (e.g., Shapiro et al., 2004; Iliev et al., 2005b). Photoionized electrons inject kinetic energy into the IGM, which raises the gas temperature to $\sim 10^4$ K and increases the Jeans mass to $M_J \sim 10^8 \ M_\odot$. Once substantial heating occurs, gas in MHs becomes unbound and eventually disperses into the surrounding IGM.

In principle, the interaction between the sources and sinks of reionization can be modelled using numerical simulations that capture the relevant scales and physics of interest. Unfortunately, the computational demands of such simulations will remain beyond our technological capability for the foreseeable future. In order to capture the global landscape of ionizing sources, box sizes of width $\gtrsim 100$ Mpc are required, while spatial resolutions $\lesssim 1$ kpc are needed to resolve MHs. Hence, on the order of $\gtrsim 10^{15}$ volume elements are required! To circumvent these demands, large-scale simulations of reionization tend to incorporate the effects of absorption systems using sub-grid models calibrated from smaller, high-resolution simulations.

A popular quantity employed in sub-grid models is the "clumping factor", defined as

$$c_l = \langle n_e^2 \rangle / \langle n_e \rangle^2. \tag{1.14}$$

The clumping factor represents the enhancement in the recombination rate due to the presence of unresolved absorption systems in the IGM. It can be used to rewrite the condition for reionization as

$$N_\gamma = 1 + \frac{1}{N_{\rm H}} \int_0^t \alpha c_l \langle n_e \rangle^2 dt. \tag{1.15}$$

Recent simulations have converged on the value of $c_l \sim 3$ at $z = 6$ (Pawlik et al., 2009; McQuinn et al., 2011; Shull et al., 2012; Finlator et al., 2012; Sobacchi & Mesinger, 2014). At this redshift, the IGM has been effectively smoothed below the Jeans mass of the heated IGM making numerical convergence possible due to more lenient resolution requirements. At higher redshift, pertaining to the onset of reionization when the IGM is still cold, the value of c_l is much less certain. In order to quantitatively assess the importance of MHs as photon sinks during reionization, numerical simulations must converge on the value of c_l during the initial stages of reionization.

1.3 Galactic Substructure Evolution

The standard cosmological model predicts that small-scale cold dark matter (CDM) perturbations are the first structures to collapse and initiate nonlinear structure formation. Afterward, a hierarchical assembly of these small building blocks leads to the formation of objects of increasingly larger scale. Galaxies are expected to contain a nested level of substructure leftover from this assembly process. This prediction is frequently confirmed in cosmological N-body simulations. For example, Figure 1.2 shows the output of the Via Lactea I simulation (Diemand

Figure 1.2: Image from Diemand et al. (2007a) showing the projected CDM density squared for a MW analog host halo at $z = 0$. The host halo has a mass of 1.8×10^{12} $M_\odot$ and a virial radius of 390 kpc. The projection covers a region 600×800 kpc and has a depth of 600 kpc. The colour scale is logarithmic in density squared and covers 20 orders of magnitude. A high level of CDM substructure is evident within the immediate environment of the host.

et al., 2007a), which followed the formation and evolution of an analog Milky Way (MW) halo. A tremendous level of substructure is clearly visible in this image: roughly 10^4 subhalos are identified within the virial radius of the host halo.

The level of substructure seen in Figure 1.2 is in stark contrast to the abundance of luminous satellites observed around the MW. This is an example of the so-called *missing satellites problem*. This refers to the statement that N-body simulations predict roughly an order of magnitude more dwarf galaxies around the MW than the ~ 10 actually observed (Klypin et al., 1999; Moore et al., 1999). One solution to this problem is that abundant substructure does exist, but the majority of subhalos are not associated with luminous objects, due to inhibited star formation. Other solutions include modifications to the matter power spectrum that suppress structure formation on small scales. This can be accomplished, for instance, in warm dark matter scenarios (e.g., Lovell et al., 2012) or models of broken scale invariance in the initial power spectrum (e.g., Kamionkowski & Liddle, 2000). The current consensus in the cosmological community favours the first solution. The idea is that star formation is inhibited in small subhalos due to a combination of photoheating from reionization and energetic feedback from supernovae and stellar winds (see, e.g., Weinberg et al., 2013).

In any event, galactic substructure contains a wealth of astrophysical information. Due to

the hierarchical nature of structure formation, subhalos provide important clues for the process of galaxy formation. Moreover, measuring the abundance of substructure offers a unique probe into the nature of dark matter on small scales. While luminous subhalos can be monitored directly, the prospects for detecting dark substructure include gravitational lensing (Keeton & Moustakas, 2009) and gamma-ray emission from potential dark matter annihilation (Pieri et al., 2008). As is always the case, gleaning information from such observations will require accurate predictions from theoretical modelling.

In this vein, it is instructive to consider the main physical processes affecting substructure evolution. First, is dynamical friction, which describes the gravitational drag exerted on a massive object passing through a uniform background of small objects. Chandrasekhar (1943) showed that the magnitude of the dynamical friction force is

$$f_{\text{fric}} = -4\pi G^2 \ln\Lambda \frac{m_{\text{sub}}^2 \rho_{\text{host}}}{v_{\text{sub}}^2}, \tag{1.16}$$

where m_{sub} is the mass of the subhalo, ρ_{host} is the background density of the host, and v_{sub} is the orbital speed of the subhalo. The factor $\ln\Lambda$, known as the Coulomb logarithm, represents the logarithm of the ratio between the maximum and minimum impact parameters of background particles contributing to the drag. Dynamical friction acts tangentially to the orbit, in the direction opposite the subhalo's motion. The timescale at which the subhalo is dragged to the centre of the host can be evaluated by equating the torque caused by equation (1.16) to the loss of orbital angular momentum. The result is (see, e.g., Binney & Tremaine, 1987)

$$t_{\text{fric}} = \frac{1.17}{\ln\Lambda} \frac{M_{\text{host}}}{m_{\text{sub}}} t_{\text{cross}}, \tag{1.17}$$

where M_{host} is the mass of the host and $t_{\text{cross}} = R_{\text{host}}/v_{\text{sub}}$ is the crossing time at the radius of the host. The dynamical friction merging time-scale is $t_{\text{fric}} \propto \mu^{-1}$ where $\mu \equiv m_{\text{sub}}/M_{\text{host}}$ is the mass ratio between the subhalo and host. That is, dynamical friction has decreasing importance for less massive subhalos. In particular, dynamical friction can be effectively ignored for $\mu \lesssim 10^{-3}$ as t_{fric} becomes much larger than the Hubble time (Boylan-Kolchin et al., 2008).

The next physical processes affecting subhalo evolution are tidal stripping and heating. These act to remove bound material from a subhalo in response to tidal forces from the host. Tidal stripping occurs in the limit of slowly-varying tidal forces. In this case, a critical radius, known as the *tidal radius*, is established at the boundary where the inward gravitational force of the subhalo exactly balances the outward tidal force of the host. For spherically symmetric density profiles, the tidal radius can be easily computed as

$$r_{\text{tid}} = \left[\frac{Gm_{\text{sub}}(< r_{\text{tid}})}{\omega^2 - \mathrm{d}^2\Phi/\mathrm{d}r^2}\right]^{1/3}, \tag{1.18}$$

where ω is the angular speed of the subhalo and Φ is the potential of the host. Tidal forces

from the host act to remove subhalo material outside r_{tid}. If the subhalo orbit is decaying from dynamical friction, r_{tid} shrinks in time and progressively more mass is lost. Tidal heating is a related process operating in the limit when a subhalo is exposed to a tidal force that varies on a time-scale shorter than its crossing time. In this case, gravitational shocks inject kinetic energy into the subhalo causing it to puff outwards (e.g., Hayashi et al., 2003). The central density of the subhalo diminishes making it more prone to further mass loss. Tidal heating is an important consideration, for example, during pericentre passage of highly eccentric obits or during close encounters with other substructure.

In general, predicting substructure statistics at the present epoch is a nontrivial task due to the extreme nonlinearity of the physical processes described above. Even when baryonic physics are ignored, the roles of dynamical friction, tidal stripping, and tidal heating are complicated by the fact that both the host and its subhalos will in general be inhomogeneous and anisotropic as a result of hierarchical structure formation. In principle, self-consistent computations can be achieved using N-body simulations where all physical processes are inherently captured. However, the computational cost of such simulations makes them limited in number (e.g., Diemand et al., 2008; Springel et al., 2008; Garrison-Kimmel et al., 2014) and the range of model and parameter space they sample. As an alternative, there exist semi-analytic models of substructure evolution (e.g. Taylor & Babul, 2004; Zentner et al., 2005; Gan et al., 2010; Jiang & van den Bosch, 2014b; Pullen et al., 2014) that employ various assumptions and simplifying approximations in order to make fast calculations. For example, it is common practice in semi-analytic models to treat subhalos as isolated systems (i.e., subhalos do not interact) within a spherically symmetric and possibly static host potential. Analytic prescriptions for dynamical friction, tidal stripping, and tidal heating are then used to integrate individual subhalo orbits forward in time.

Numerical simulations and semi-analytic models have given rise to a number of interesting features of substructure evolution. For example, we know that a dichotomy exists between the evolution of low- and high-mass subhalos due to the relative importance of dynamical friction between the two groups. The general picture of high-mass ($\mu \gtrsim 10^{-3}$) subhalo evolution, where dynamical friction is strong, is that of quick descent and disruption within the central depths of the host. Low-mass subhalos, on the other hand, exhibit more of a slow and steady descent within the host. Mass is thus the main driver of evolution for high-mass subhalos, but it is unclear whether the same is true for low-mass subhalos. In Chapter 3 we consider whether any physical (e.g., mass, concentration) or orbital (e.g., energy, angular momentum) properties may be used as predictive indicators of low-mass subhalo evolution.

1.4 Cosmic Neutrinos

The standard model of particle physics predicts the existence of three neutrino flavours (electron, muon, tau) that exist as superpositions of three mass eigenstates (denoted ν_1, ν_2, ν_3). The

generic prediction of the standard model is that the mass eigenstates have identically zero mass. However, extended models exist for which the mass eigenstates can be non-zero (see Lesgourgues & Pastor, 2006, and references therein). In this case, Pontecorvo (1958) showed it is possible that flavour is not conserved, allowing neutrinos to oscillate between flavour with time. This phenomena was firmly established by observations of the flux of electron neutrinos from the Sun that were roughly three times smaller than predicted based on theoretical predictions (e.g., Cleveland et al., 1998; Ahmad et al., 2002). The resolution is that electron neutrinos, the only flavour produced in the Sun, oscillate between muon and tau flavours during their passage through the Sun, leading to a suppressed flux of electron neutrinos when they arrive at Earth (Wolfenstein, 1978; Mikheyev & Smirnov, 1985). The existence of neutrino oscillations have also been verified from the flux of electron and muon neutrinos produced from cosmic ray collisions in the Earth's atmosphere (e.g., Hirata et al., 1992; Becker-Szendy et al., 1992). These experiments conclusively confirm the existence of at least two massive neutrinos.

Solar and atmospheric oscillations are able to place constraints on the mass-squared differences between neutrino eigenstates. The current constraints are (Fogli et al., 2012):

$$\Delta m_{21}^2 \equiv m_2^2 - m_1^2 = \quad 7.5 \times 10^{-5} \text{ eV}^2$$
$$\Delta m_{31}^2 \equiv m_3^2 - (m_1^2 + m_2^2)/2 = \quad 2.4 \times 10^{-3} \text{ eV}^2. \quad (1.19)$$

Since these experiments are only sensitive to mass-squared splittings, they are unable to provide information on the absolute mass scale of neutrinos. In particular, if the mass splittings are comparable to the individual masses, then it is unknown whether neutrinos exist in the *normal* (i.e., two light and one massive neutrino) or *inverted* (i.e., one light and two massive neutrinos) hierarchy. Conversely, if the mass splittings are much smaller than individual masses, then the hierarchy is indistinguishable and neutrinos are said to be *quasi-degenerate*. The mass splittings shown above imply lower limits on the sum of neutrino masses as $\sum m_i \gtrsim 0.05$ eV and $\sum m_i \gtrsim 0.1$ eV for the normal and inverted hierarchies, respectively. Particle physicists are working to constrain individual neutrino masses through experiments that measure the kinematics of electrons emitted during β decay reactions. Current constraints place an upper limit on the mass of the electron neutrino at $m_{\nu_e} \leq 2.3$ eV (Kraus et al., 2005) while the upcoming KATRIN experiment is expected to reduce this bound to ~ 0.35 eV (Eitel, 2005). Below we consider the prospect of measuring neutrino mass from cosmological observations.

Neutrinos are expected to play an important role in cosmology through the existence of the cosmic neutrino background (CNB) predicted from the standard big bang scenario. The CNB, in analogy to the CMB, contains relic neutrinos that last interacted with matter when they decoupled from the early universe plasma. The time of neutrino decoupling occurred when the weak interaction rate fell below the Hubble expansion rate. This took place when the universe had a temperature of $T \approx 1$ MeV and was $t \approx 1$ second old (Lesgourgues & Pastor, 2006). The mass constraints above place neutrinos on the $m_\nu \lesssim 1$ eV scale meaning they were ultra-

relativistic at the time of decoupling. Neutrinos therefore contributed to the radiation content of the universe at this time. After decoupling, the neutrino temperature redshifted adiabatically, decaying in proportion to the scale factor. Today, the CNB temperature is $T_\nu \approx 1.9$ K. This is slightly lower than the CMB temperature, $T_\gamma \approx 2.7$ K, since neutrinos decoupled prior to the electron-positron annihilation, which boosted the photon temperature relative to that of neutrinos (see, e.g., Dodelson, 2003).

The present CNB temperature implies that at least two neutrinos are non-relativistic today since both $|\Delta m_{21}|$ and $|\Delta m_{31}|$ are larger than $T_\nu \approx 10^{-4}$ eV. The non-relativistic transition occurs approximately when the momentum, $p \propto a^{-1}$, drops below m_ν. The redshift at which this occurs thus depends on both the mass eigenstate and distribution in neutrino momenta. For a Fermi-Dirac momentum distribution, roughly 50% of neutrinos of mass m_ν become non-relativistic at the redshift

$$z_{\mathrm{nr}} \simeq 2000 \left(\frac{m_\nu}{1 \text{ eV}} \right). \tag{1.20}$$

Once neutrinos become non-relativistic, they contribute to the matter content of the universe, with an energy density at $z = 0$ proportional to their mass (Mangano et al., 2005):

$$\Omega_\nu = \frac{m_\nu}{93.14 h^2 \text{ eV}} \tag{1.21}$$

Neutrinos within the present mass bounds constitute a form of hot dark matter (HDM) due to their larger thermal velocities. The mean velocity of a neutrino of mass m_ν at redshift z can be derived from the Fermi-Dirac 2distribution:

$$\langle v \rangle \simeq 160 \ (1+z) \left(\frac{1 \text{ ev}}{m_\nu} \right) \text{ km s}^{-1}. \tag{1.22}$$

For comparison, galaxies have velocity dispersion $\sigma_v \sim 100$ km s^{-1} while clusters have $\sigma_v \sim 1000$ km s^{-1}. Hence, even at low z, sub-eV neutrinos have sufficient thermal velocity to inhibit their collapse into small-scale CDM structures.

The combined feebleness of the weak interaction and small limits on neutrino mass will continue to make direct detection of relic neutrinos difficult for the next few decades (Ringwald & Wong, 2004). Instead, we are forced to rely on indirect detections of the CNB. During the early universe, neutrinos contributed to the radiation content of the universe, influencing the background expansion, and having implications for both big bang nucleosynthesis and CMB anisotropies. Recent results from the Planck satellite place an upper bound on the sum of neutrino masses at $\sum m_\nu < 0.194$ eV (Planck Collaboration et al., 2015). Other attempts at indirectly observing the CNB include measuring the small-scale suppression of the matter power spectrum induced by neutrino free-streaming. Recent constraints obtained from galaxy surveys place an upper limit of $\sum m_\nu \lesssim 0.30$ eV (e.g., Xia et al., 2012; de Putter et al., 2012). While these cosmological observations are making good progress to lower the bound on $\sum m_\nu$, they are still insensitive to the hierarchy of individual masses.

Recently, Zhu et al. (2014b) proposed an alternative approach for measuring *individual* neutrino mass from cosmological observations. This method exploits the fact that neutrino free-streaming establishes a relative bulk flow between CDM and neutrinos on small (~ 10 Mpc) scales. As a result, neutrinos become systematically offset from CDM, giving rise to a unique dipole distortion in the matter density field. One can visualize this by considering a bulk flow of neutrinos being gravitational focused into a high density wake downstream of a large CDM halo. The result is a dipole distortion in the neutrino density field in the direction of the relative velocity between CDM and neutrinos. The magnitude and direction of this wake depend sensitively on m_ν meaning that each mass eigenstate produces its own signal. In principle, the total signal can be separated into each component to provide individual constraints on m_ν. The only required information is knowledge of the direction of the relative velocity vector. It is possible that this may be obtained by applying linear transformations to the observed density field. Properly addressing the efficacy of this approach, however, requires the use of cosmological simulations that trace the nonlinear evolution of both CDM and neutrinos.

1.5   Thesis Outline

In Chapter 2 we employ a numerical convergence study to determine the resolution requirements of hydrodynamic simulations to properly model the opacity of the unheated IGM during the onset of reionization. This project was done in collaboration with Rajat Thomas and Marcelo Alvarez. Our work has been published in the Astrophysical Journal (Emberson et al., 2013). My contribution to the project included running the hydrodynamic simulation suite, writing and running the radiative transfer code, and analyzing the results of the convergence study. Writing of our paper was mainly split amongst Marcelo and I.

In Chapter 3 we study the role played by concentration in the dynamical evolution of low-mass subhalos within a galactic host. This project was done in collaboration with Takeshi Kobayashi and Marcelo Alvarez. Our work has been published in the Astrophysical Journal (Emberson et al., 2015). My contribution to the project included analyzing the public Via Lactea II (Diemand et al., 2008) halo catalogue and interpreting the results in the context of subhalo evolution. The majority of the paper was written by myself.

In Chapter 4 we investigate the accuracy of using linear transformations to reconstruct the CDM-neutrino relative velocity field. This work was done in collaboration with Derek Inman, Ue-Li Pen, Alban Farchi, Hao-Ran Yu, and Joachim Harnois-Déraps. Our work was published in Physical Review D (Inman et al., 2015). My contributions included sharing in the development of the cosmology code CUBEP³M (Harnois-Déraps et al., 2013) to incorporate N-body neutrino particles as well as the running and analysis of the neutrino simulations. I played a secondary role in the writing of our paper.

In Chapter 5 we present preliminary results from the analysis of a recent CDM plus neutrino N-body simulation. This simulation, containing $\simeq 3 \times 10^{12}$ particles, is presently the world's

largest cosmological N-body simulation. This work was done in collaboration with Hao-Ran Yu, Derek Inman, Tong-Jie Zhang, Ue-Li Pen, Joachim Harnois-Déraps, Shuo Yuan, Hong-Ming Zhu, Xuelei Chen, Huan-Yu Teng, and Zhi-Zhong Xing. We are currently in the process of drafting a manuscript to be submitted for publication. My contributions included profiling and optimizing CUBEP^{3}M to scale to $\gtrsim 300,000$ cores and the analysis of halo catalogues for the calculation of neutrino bias.

Chapter 2

The opacity of the intergalactic medium during reionization: resolving small-scale structure

2.1   Chapter Overview

Early in the reionization process, the intergalactic medium (IGM) would have been quite inhomogeneous on small scales, due to the low Jeans mass in the neutral IGM and the hierarchical growth of structure in a cold dark matter Universe. This small-scale structure acted as an important sink during the epoch of reionization, impeding the progress of the ionization fronts that swept out from the first sources of ionizing radiation. Here we present results of high-resolution cosmological hydrodynamics simulations that resolve the cosmological Jeans mass of the neutral IGM in representative volumes several Mpc across. The adiabatic hydrodynamics we follow are appropriate in an *unheated* IGM, before the gas has had a chance to respond to the photoionization heating. Our focus is determination of the resolution required in cosmological simulations in order to sufficiently sample and resolve small-scale structure regulating the opacity of an unheated IGM. We find that a dark matter particle mass of $m_{\rm dm} \lesssim 50\ M_\odot$ and box size of $L \gtrsim 1$ Mpc are required. With our converged results we show how the mean free path of ionizing radiation and clumping factor of ionized hydrogen depends upon the ultraviolet background (UVB) flux and redshift. We find, for example at $z = 10$, clumping factors typically of 10 to 20 for an ionization rate of $\Gamma \sim 0.3 - 3 \times 10^{-12}{\rm s}^{-1}$, with corresponding mean free paths of $\sim 3 - 15$ Mpc, extending previous work on the evolving mean free path to considerably

smaller scales and earlier times.

2.2   Introduction

The fact that the most abundant sources of radiation during reionization are likely to be currently undetectable (e.g., Trenti et al., 2010; Oesch et al., 2012; Alvarez et al., 2012) means that the details of the reionization process are beyond most current observational probes. The notable exceptions are observations of the polarization of the cosmic microwave background (CMB), which imply an optical depth to Thomson scattering of $\tau \sim 0.09$ (Komatsu et al., 2011), and the appearance of a Gunn-Peterson trough in the spectra of distant quasars (Fan et al., 2006), indicating that reionization was largely complete by $z \sim 6$. Reionization is therefore thought to have mainly taken place over the redshift range $z \sim 6 - 15$. Due to the lack of more specific constraints, much of our current understanding about the epoch of reionization comes from theoretical studies in the context of the ΛCDM cosmology.

The picture which always emerges is of small-scale gaseous structures forming at $z > 20$, due to the collapse of dark matter halos at the Jeans scale, roughly 10^4 $M_\odot$ (e.g., Peebles & Dicke, 1968; Couchman & Rees, 1986; Shapiro et al., 1994; Gnedin & Hui, 1998). The gas was just cool enough to fall into halos at this mass, leading to strong inhomogenities on a scale of tens of comoving parsecs. At the same time, slightly more massive halos, with masses on the order of $\sim 10^6$ $M_\odot$, formed enough H_2 molecules in their cores to cool efficiently, leading to the formation of the first stars in the Universe (e.g., Tegmark et al., 1997; Abel et al., 2002; Bromm et al., 2002; Yoshida et al., 2003). The ionizing radiation from these stars is thought to have created substantial, yet short-lived H II regions, which were shaped by the surrounding inhomogeneity of the gas distribution (Alvarez et al., 2006; Abel et al., 2007; Yoshida et al., 2007).

Eventually, sufficiently large halos formed that triggered the formation of the first galaxies (Johnson et al., 2007; Wise & Abel, 2008; Greif et al., 2008). These nascent dwarf galaxies would have created longer-lived and isolated H II regions (Wise & Cen, 2009; Wise et al., 2012). It is unclear how these galaxies evolved into the much more luminous ones that have been observed at redshifts as high as $z \sim 8$ (e.g., Bouwens et al., 2010). Nevertheless, it is widely believed that as the first galaxies grew and merged, their collective radiative output created a large and complex patchwork of ionized bubbles, with characteristic sizes on the order of tens to hundreds of comoving Mpc (e.g., Barkana & Loeb, 2004; Furlanetto et al., 2004; Iliev et al., 2006). During this time, dense systems in the IGM likely impeded the progress of ionization fronts (Barkana & Loeb, 1999; Haiman et al., 2001; Shapiro et al., 2004; Iliev et al., 2005a; Ciardi et al., 2006). At the end of reionization the so-called "Lyman-limit" systems, dense clouds of gas optically-thick to ionizing radiation observed in the spectra of quasars at $z < 6$ (e.g., Storrie-Lombardi et al., 1994; Prochaska et al., 2010), dominated the overall opacity of the IGM to ionizing radiation. These systems crucially influenced the percolation phase of reionization (Gnedin & Fan, 2006;

Choudhury et al., 2009; Alvarez & Abel, 2012), which in turn determined the evolution and structure of the ionizing background (e.g., Haardt & Madau, 1996; Bolton & Haehnelt, 2007; McQuinn et al., 2011).

Thus, the progress of reionization depended not only on the properties of the sources of ionizing radiation, but also on the *sinks*. Theoretical models of reionization must describe not just the spectral energy distribution, abundance, and clustering of early sources of ionizing radiation, but also the inhomogeneity of the intergalactic medium (IGM) in the space between the sources. It is this latter description that is the goal of the present work.

Early descriptions of reionization took into account inhomogeneities in the IGM through a "clumping factor", c_l, by which the recombination rate is boosted relative to the homogeneous case. This allows one to write a global ionization rate, equal to the ionizing photon emmissivity minus the recombination rate of a clumpy IGM, and thereby determine the reionization history for a given ionizing source population. Shapiro & Giroux (1987) used such a model to show that the observed population of QSOs were insufficient to have reionized the Universe by $z \sim 5$. Their assumption of $c_l \sim 1$ would have been conservative, in that that additional recombinations would have made it even more difficult for quasars alone to reionize the Universe.

In addition to being useful in modelling the reionization history, the clumping factor is also important in estimating the necessary number of ionizing photons per baryon to *maintain* an ionized Universe. The necessary and sufficient condition for maintaining an ionized Universe is that the ionizing photon emissivity should be greater than or equal to the recombination rate of the IGM. Madau et al. (1999) used this fact to derive a critical star formation rate, above which the rate of ionizing photons is enough to maintain the Universe in an ionized state.

Gnedin & Ostriker (1997) used hydrodynamic simulations with a treatment of photoionization in the "local optical depth" approximation to determine the clumping factor of the ionized component of the IGM, finding a value of $c_l \sim 30$ at $z = 6$. They also pointed out that the actual clumping factor of the IGM would have been larger due to structure on smaller scales than they resolved. More recently, Miralda-Escudé et al. (2000) built a semi-analytical model for the reionization of an inhomogenous IGM, in which the underlying gas density distribution was determined by numerical simulations. They argued that in addition to specifying the clumping factor of the ionized medium, it is also necessary to describe the distribution of high-density gas clouds that are able to self-shield against ionizing radiation.

McQuinn et al. (2011) followed a similar approach to that of Miralda-Escudé et al. (2000) to explain the evolution of the ionizing background radiation at redshifts less than $z \sim 6$, using more realistic numerical simulations which were post-processed with radiative transfer. These works were focused on the large scales relevant in the post-reionization IGM, after photoionization heating has "ironed out" the clumpiness of the IGM on the smallest scales. The timescale over which this smoothing occurs is on the order of $10 - 100$ Myr (Iliev et al., 2005b). Although the recombination rate in the homogenous IGM is on the order of 1 Gyr, small-scale inhomogeneities increase recombinations by at least an order of magnitude, making the recombination

time of the high-redshift IGM comparable to the smoothing time. Our work here is focused on the higher redshifts and smaller scales that were most relevant early in reionization before much smoothing has occurred.

We seek to obtain convergence in the quantities that describe the inhomogeneity of the *unheated* IGM during the epoch of reionization, such as the mean free path, λ, clumping factor, c_l, and density threshold above which gas is self-shielded, Δ_{crit}, by spanning the parameter space of redshift and ionizing background intensity, j_ν. To do this, we post-process cosmological adiabatic hydrodynamics simulations with radiative transfer calculations along different lines of sight through the simulated volume. Radiative feedback raises the Jeans mass of the IGM, thereby increasing the scale of inhomogeneities. Therefore, the resolutions we find in our adiabatic simulations that are necessary to resolve structure in the unheated IGM are also sufficient to model radiative feedback at all times.

The outline of the paper is as follows. Details of the simulation setup and radiative transfer are described in §2.3. In §2.4 we present our numerical results, followed by §2.5, where we present the results of our convergence tests. §2.6 concludes with a discussion of our main results.

2.3 Numerical Approach

Here we describe our numerical approach, in which we perform a suite of cosmological adiabatic[1] hydrodynamics simulations using the publicly available SPH code Gadget-2 (Springel, 2005). We then postprocess each simulation with multifrequency radiative transfer of hydrogen ionizing radiation, assuming photoionization equilibrium, to determine the dependence of basic quantities, like the ionizing photon mean free path and clumping factor, on redshift and intensity of the background radiation field. The mean free path presented here is used to quantify the opacity of the IGM to ionizing radiation and should be considered a local quantity that depends on the spatial variation of the UVB flux during patchy reionization.

2.3.1 Cosmological Hydrodynamic Simulations

The cosmological simulations are parameterized by box size, L, and total number of dark matter and gas particles, N. Table 2.1 summarizes these parameters for our suite of simulations and lists their corresponding dark matter particle masses, m_{dm}, along with the comoving gravitational softening length, r_{soft}. The simulations were evolved from redshift $z = 200$ to $z = 6$, except for simulations C1 through C4 which, due to computational limitations, were terminated early at $z = 10$. Initial conditions were generated separately for dark matter and baryons using transfer functions computed by CAMB for each component, with the same random phases.

---

[1]In this case the gas cools adiabatically with the expansion of space while radiative heating and cooling processes that would otherwise affect its temperature are ignored. The justification and consequences for assuming this choice are discussed in the text.

Table 2.1: Simulation Parameters

Simulation	N	L (Mpc)	m_{dm} $(M_\odot)$	r_{soft} (pc)
A1	2×256^3	0.25	31	30
A3	2×256^3	1	2.0×10^3	120
A4	2×256^3	2	1.6×10^4	240
A6	2×256^3	8	1.0×10^6	960
B1	2×512^3	0.25	3.8	15
B2	2×512^3	0.5	31	30
B3	2×512^3	1	240	60
B4	2×512^3	2	2.0×10^3	120
B5	2×512^3	4	1.6×10^4	240
B6	2×512^3	8	1.3×10^5	480
C1	2×1024^3	0.25	0.5	7.5
C2	2×1024^3	0.5	3.8	15
C3	2×1024^3	1	31	30
C4	2×1024^3	2	240	60
C6	2×1024^3	8	1.6×10^4	240

Throughout our work we assume the set of cosmological parameters $(\Omega_{\mathrm{DM}}, \Omega_{\mathrm{b}}, \Omega_\Lambda, h) = (0.228, 0.042, 0.73, 0.72)$.

A quantitative test of the simulated structure formation is to identify dark matter halos to construct mass functions, dn/dM, which can be compared to analytic models. Figure 2.1 shows the mass functions obtained from a friends-of-friends (FOF) halo identification scheme with linking length of 0.2 mean interparticle spacings, at redshifts $z = 10$ and 20 for two groups of simulations sharing common mass resolutions of $m_{\mathrm{dm}} = 31\ M_\odot$ and $1.6 \times 10^4\ M_\odot$. A common fitting function to compare to is the Warren et al. (2006) mass function. When doing so, however, it is important to note that this model assumes a Universe with infinite spatial extent; something that cannot be achieved using numerical simulations. It is therefore useful to compute Warren et al. mass functions using a modified variance of the form $\sigma_{\mathrm{eff}}^2 \equiv \sigma^2 - \sigma^2(M_{\mathrm{box}})$, where M_{box} is the total mass contained within the simulated volume. This has the effect of removing contributions from mass fluctuations on scales larger than that of the simulated volume. With this correction we find that the Warren et al. mass function is generally well-matched by the numerical simulations.

There is one important feature worth noting in Figure 2.1: For fixed mass resolution, simulations with larger volumes tend to trace the analytic curves more closely. This is most noticeable in the top panel for $z = 20$. We can attribute this to the fact that at fixed resolution, simulations with larger volumes will contain a more statistically representative collection of halos. In §2.5 we will show how sample variance in small boxes has important consequences for numerical convergence. Even though a simulation may have a sufficient mass resolution to resolve low-mass halos within the IGM, its volume may be so small that sample variance causes noticeable variation in computed quantities between different random realizations. Recall that we used a
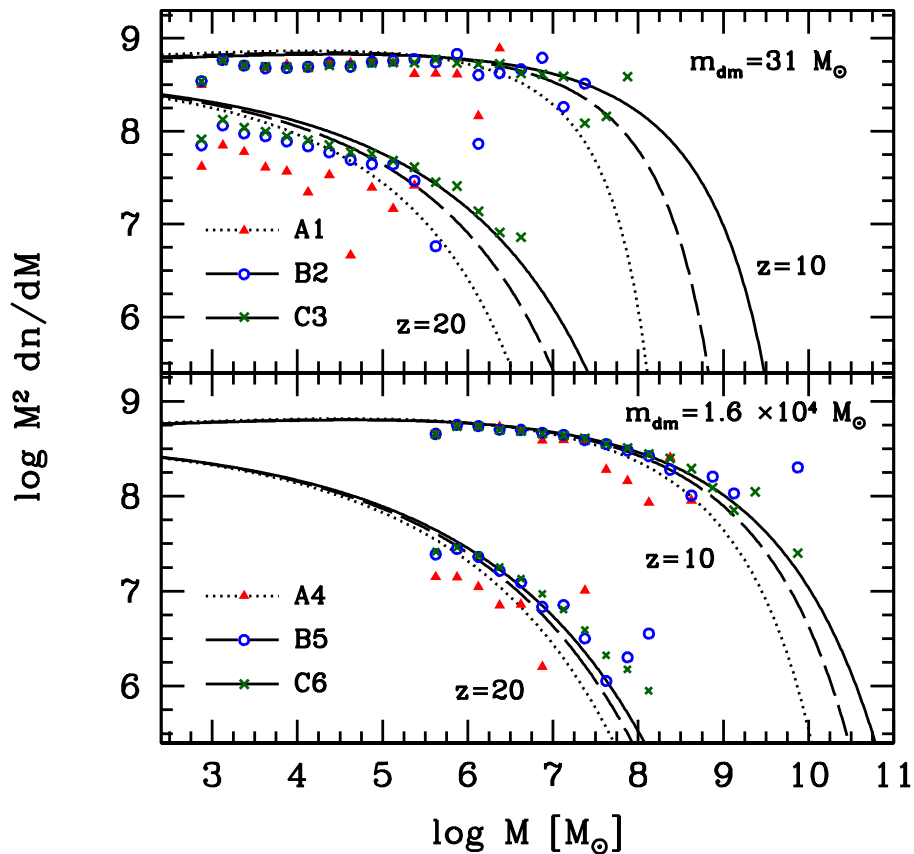
Figure 2.1: Halo mass functions from six simulations are compared to their Warren et al. counterparts using the variance $\sigma^2_{\mathrm{eff}} \equiv \sigma^2 - \sigma^2(M_{\mathrm{box}})$ at redshifts 10 and 20. The top panel plots simulations A1, B2, and C3 each containing dark matter masses of $m_{\mathrm{dm}} = 31\ M_{\odot}$ while the lower panel plots simulations A4, B5, and C6 with $m_{\mathrm{dm}} = 1.6 \times 10^4\ M_{\odot}$. In each case, points denote halo mass functions obtained from the simulations while the lines trace the corresponding Warren et al. curves.

modified variance σ^2_{eff} when computing the analytic curves of Figure 2.1 in order to compensate for missing large-scale power in the finite volume boxes. Though not necessary for our purposes here, we point out to the reader that Reed et al. (2007) present an additional correction that can be used to adjust simulated mass functions for sample variance from small volumes.

It is well known that the inhomogeneous nature of the IGM plays an important role in the progression of the reionization epoch. This was emphasized by Miralda-Escudé et al. (2000) who presented an evolutionary model of reionization based on the gas density distribution observed in numerical simulations. It is therefore useful to examine the density distribution of baryons within cosmological simulations, through the use of the probability density function (PDF), $P(\Delta)$, defined to be the normalized distribution of gas in terms of overdensity $\Delta \equiv \rho/\bar{\rho}$.

In Figure 2.2 we plot volume-weighted gas PDFs from our fiducial simulation B2 which contains 2×512^3 dark matter plus gas particles in a box of comoving length 0.5 Mpc. More

precisely, we plot $\Delta^{2.5} P(\Delta)$ which is expected to approach a constant at $\Delta > \Delta_{\mathrm{vir}} = 18\pi^2$ if gas at those densities is collapsed within halos described by a density profile $\rho \propto r^{-2}$. As time evolves, the fraction of gas collapsed within halos increases, though only for $z \lesssim 10$ does the high-density tail of the PDF appear to approach a constant value.

Recall that the PDFs shown here correspond to adiabatic simulations for which radiative heating and cooling processes are ignored. We expect that heating would evolve the gas distribution in such a way as to decrease the amplitude of $P(\Delta)$ at large values of Δ as gas boils out of overdense regions. In this work we are concerned with the initial phase of reionization before substantial heating occurs, and discuss at length in §2.6 how heating would affect our results. In contrast, radiative cooling would act to promote $P(\Delta)$ at large values of Δ from the enhanced collapse of gas into overdense halos. However, our work is primarily concerned with determining the resolution requirements for minihalos with masses on the order of $10^4 \ M_\odot$. For these halos, H_2 cooling is the dominant mechanism, but this is rapidly suppressed once an UVB is established within the IGM (Haiman et al., 2000). Radiative cooling is thus most relevant for the easily resolved large halos, and our choice to omit cooling should not qualitatively affect our conclusions with respect to convergence of small-scale structure.

2.3.2 Post-processed Ionization Calculation

In order to simulate the effects of self-shielding by absorption systems, we postprocess the SPH density field with a multifrequency radiative transfer algorithm. This involves tracing the attenuation of the ionizing radiation along different lines of sight throughout the volume while assuming photoionization equilibrium.

Ultraviolet Background Spectrum

We consider a background ionizing intensity I_ν, so that the flux of photons capable of ionizing hydrogen is

$$F = \int d\Omega \int_{\nu_{\mathrm{HI}}}^{4\nu_{\mathrm{HI}}} \frac{I_\nu}{h\nu} d\nu, \tag{2.1}$$

where $h\nu_{\mathrm{HI}} = 13.6$ eV is the photon energy at the Lyman edge. The upper limit in the integral corresponds to the ionizing threshold for fully ionizing helium – we assume helium is singly ionized along with hydrogen, and therefore only consider photons below the He II Lyman edge.

We adopt a power-law UVB spectrum,

$$I_\nu = I_o \left(\frac{\nu}{\nu_{\mathrm{HI}}} \right)^{-\alpha}, \tag{2.2}$$

where $\nu_{\mathrm{HI}} \leq \nu \leq 4\nu_{\mathrm{HI}}$ and I_o is the intensity at the Lyman edge. In our analysis we have sampled a region of parameter space for which $1 \leq \alpha \leq 3$. Our fiducial value of $\alpha = 2$ is chosen to be consistent with the spectral index we would expect for an ionizing background produced from a mixture of galaxies and quasars (e.g., Bolton & Haehnelt, 2007). Our results
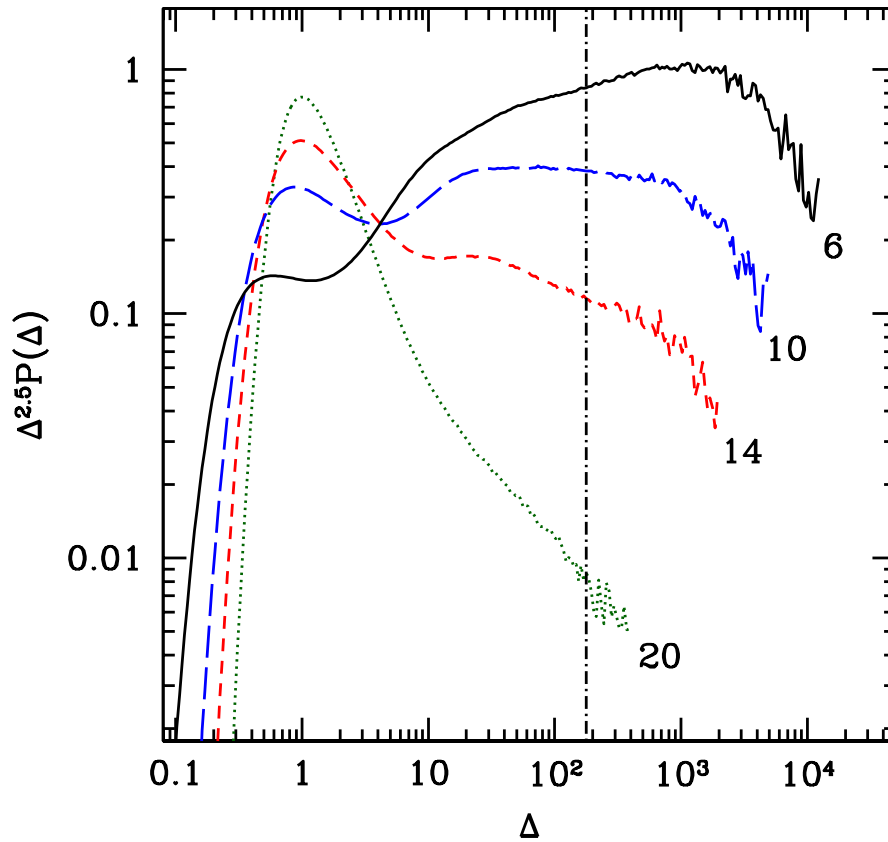
Figure 2.2: Gas PDFs for our fiducial simulation B2 (512^3, 0.5 Mpc) at different redshifts, as labelled beside the curves. The vertical dot-dashed line delineates the overdensity $\Delta_{\mathrm{vir}} = 18\pi^2$ of a virialized isothermal sphere. If collapsed structures have a density profile of the form $\rho \propto r^{-2}$, for $\Delta_{\mathrm{vir}} < \rho/\bar{\rho} < \Delta_{\mathrm{max}}$, then $P(\Delta) \propto \Delta^{-2.5}$ for $\Delta_{\mathrm{vir}} < \Delta < \Delta_{\mathrm{max}}$. We plot the PDF multiplied by $\Delta^{2.5}$ so that the curve should approach a constant for $\Delta > \Delta_{\mathrm{vir}}$ if gas is collapsed within these structures.

exhibit only a minor dependence on spectral index in this range, as also found by McQuinn et al. (2011). For this reason we henceforth refer only to our fiducial case of $\alpha = 2$.

The intensity is often expressed in terms of the quantity J_{-21}, defined to be the isotropic equivalent of I_o, $(\int I_0 d\Omega)/(4\pi)$, in units of 10^{-21} erg cm^{-2}s^{-1}Hz^{-1}ster^{-1}. For the form expressed in equation (2.2), we can integrate equation (2.1) to relate J_{-21} to the flux of ionizing photons. For $\alpha = 2$, we obtain:

$$J_{-21} = 0.09 \left(\frac{F}{10^5 \text{ cm}^{-2}\text{s}^{-1}} \right). \tag{2.3}$$

Another useful quantity to describe the UVB is Γ_{-12}, defined to be the ionization rate per atom, in units of 10^{-12} s^{-1}:

$$\Gamma_{-12} = 0.3 \left(\frac{F}{10^5 \text{ cm}^{-2}\text{s}^{-1}} \right). \tag{2.4}$$

Note that this refers to the ionization rate corresponding to a given background, and not the mean ionization rate per atom along our rays, which is lower due to attenuation and includes the neutral component of the IGM.

We calculate the ionization state of the volume for a broad range of background flux with the fiducial value of $F = 10^5$ cm^{-2}s^{-1} taken to be consistent with the value of $\Gamma_{-12} \sim 0.3$ inferred from the optical depth of the Lyα forest seen in quasar spectra (e.g., Bolton & Haehnelt, 2007). Due to its common usage in the literature, we will report our results in terms of Γ_{-12}, though it should be remembered that its conversion to flux simply follows equation (2.4).

Ray-tracing

In our ray-based approach, the UVB has a plane-parallel direction dependence, so that $I_\nu = F_\nu \delta(\hat{n})$, where $\hat{n}$ is the direction of propagation of the radiation and F_ν is the spectral flux density. This is appropriate especially in the beginning stages of reionization, where a given patch of the IGM is initially exposed to a one-sided flux from the downstream direction of the ionization front. In addition, we use the "case B" recombination coefficient which assumes that recombinations to the ground state are quickly cancelled by subsequent photoionizations and implies that rays can be treated independently. In reality, ionizing radiation produced by recombinations directly to the ground state becomes part of the UVB, changing the spectral shape that we adopt in equation (2.2), but not the total ionizing photon flux. Given the relative insensitivity we find to the spectral shape, using case B recombination rates should be a good approximation. Finally, because the equilibration time is very short compared to the Hubble time, we use photoionization equilibrium, which allows us to calculate the ionization state and attenuation of the background self-consistently by sequentially iterating along the ray in the direction $\hat{n}$.

To obtain an unbiased sample of the gas density field and minimize noise, the rays are assigned starting points uniformly distributed in a plane with orientations perpendicular to the plane. We use three orthogonal planes in order to sample different directions. Each ray segment corresponds to a cubic volume element, within which the mean density is obtained from the SPH particle data by the mass-conserving spline interpolation outlined in Alvarez et al. (2006). The ray segments have lengths given by $L/N_{\rm ray}$, where L is the box size, so that the number of rays is proportional to $N_{\rm ray}^2$, while the number of segments along a given ray is proportional to $N_{\rm ray}$. We check for convergence in our radiative transfer calculations by interpolating to a variety of values for $N_{\rm ray}$. From this we find that it is necessary to interpolate to $N_{\rm ray} = 1024$ for the 256^3 and 512^3 particle simulations and to $N_{\rm ray} = 2048$ for the 1024^3 particle simulations.

Equilibrium Radiative Transfer

The equation of radiative transfer for I_ν is

$$\frac{dI_\nu}{ds} = -n_{\rm HI}\sigma_\nu I_\nu + \epsilon_\nu, \qquad (2.5)$$

where s is the proper distance and n_{HI} is the proper number density of neutral hydrogen. Here we are concerned with the transfer of ionizing radiation through a patch of IGM in which there are no sources, and therefore set $\epsilon_\nu = 0$.

The ionization rate within a given ray segment is related to the background intensity and neutral hydrogen column density, N_{HI}, integrated along a given ray by using the solution of equation (2.5):

$$\Gamma = 4\pi \int_{\nu_{\mathrm{HI}}}^{4\nu_{\mathrm{HI}}} \frac{I_\nu}{h\nu} \sigma_\nu e^{-N_{\mathrm{HI}}\sigma_\nu} d\nu, \tag{2.6}$$

where σ_ν is the absorption cross section, with mean value

$$\bar{\sigma} \equiv \frac{\int_{\nu_{\mathrm{HI}}}^{4\nu_{\mathrm{HI}}} \sigma_\nu \frac{I_\nu}{h\nu} d\nu}{\int_{\nu_{\mathrm{HI}}}^{4\nu_{\mathrm{HI}}} \frac{I_\nu}{h\nu} d\nu} = 2.84 \times 10^{-18} \text{ cm}^2. \tag{2.7}$$

The flux of ionizing photons is diminished along the ray through absorption by intervening neutral hydrogen, and the spectrum steepens as softer photons are preferentially absorbed.

To determine the opacity along the ray self-consistently, we iterate along the ray, using the total H I column density from the previous ray segments to calculate the photoionization rate at the current segment using equation (2.6). This is then used to determine the neutral hydrogen density in the current segment under the assumption of photoionization equilibrium:

$$\Gamma n_{\mathrm{HI}} = \alpha_B n_{\mathrm{HII}} n_e, \tag{2.8}$$

where n_{HI}, n_{HII} and n_e are the number densities of neutral hydrogen, ionized hydrogen, and electrons within that segment. The resulting value of H I density is then used to update the total column density, and the procedure is repeated until the end of the ray is reached.

Equation (2.8) assumes a uniform radiation field within each ray segment. This assumption breaks down if the segment becomes sufficiently optically thick that Γ changes significantly across it. To address this issue, individual ray segments are split into plane-parallel subsegments in the direction $\hat{n}$ with widths chosen such that the flux passing through each subsegment is attenuated by no more than 2% of its initial value. Photoionization equilibrium is applied in sequence to each subsegment and global quantities pertaining to the segment as a whole are computed as volume averages over each subsegment.

We assume that all free electrons within the volume come from hydrogen and consider a uniform gas temperature of $T_{\mathrm{gas}} = 10^4$ K so that $\alpha_B = 2.6 \times 10^{-13}$ cm^{3}s^{-1}. Including helium in our calculations would lead to small corrections in the hardening of the radiation at high optical depths, due to the slightly different frequency dependence of the He I absorption cross-section relative to that of H I. Given the insensitivity of our results to varying the spectral slope α, inclusion of helium radiative transfer would not improve the accuracy of our results, while needlessly complicating their interpretation, so we neglect it.

Optimal Ray Length and the Mean Free Path

The opacity of the IGM can be written in terms of the mean free path, with the equation of transfer for the flux of ionizing photons given by

$$\frac{dF}{ds} = -\frac{F(1+z)}{\lambda}, \tag{2.9}$$

where F is the total flux of ionizing photons in units of $\text{cm}^{-2}\text{s}^{-1}$, and the factor $1+z$ accounts for the fact that we define the mean free path to be in comoving units, and is the definition we use throughout this paper. We calculate the mean free path along a given ray as the solution to equation (2.9):

$$\lambda = -\frac{s}{\ln(F_{\text{out}}/F)}, \tag{2.10}$$

where s is now the comoving length of the ray, F is the incident flux at the start of the ray, and F_{out} is the attenuated flux leaving the last ray segment. The total mean free path is determined by first averaging F_{out} over all rays, then applying equation (2.10).

Naively, we may choose to set $s = L$ so that each ray samples the entire length of the box. However, we must be careful since the use of equation (2.10) is not physically meaningful in the optically thick limit where F_{out} can tend to 0. In other words, we want to determine the opacity of the IGM due to small-scale structure at a fixed background flux, but including the cumulative effect of this shielding over distances approaching the mean free path would correspond to a *lower* flux than what we assume.

An easy way to avoid this problem is to send photons along shorter rays. Of course, this has the disadvantage of sampling smaller portions of the IGM, possibly missing individual self-shielded structures. It is thus optimal to choose a ray length such that the rays on average remain optically thin, while still sampling a sufficiently long distance to take into account the self-shielding of individual dense structures. We achieve this by first calculating λ as a function of s, and then choose the optimal ray length to be the largest value of s for which $s \leq \lambda(s)/5$. A lower cutoff of $s \geq L/32$ is also applied. If this condition cannot be satisfied we flag the given region of parameter space and omit its inclusion in our analysis. For ray lengths $s < L$, the usage of the box is maximized by resetting the intensity along each ray after a distance of s, until the ray has traversed a distance L.

Figure 2.3 demonstrates our procedure of selecting ray lengths at different fluxes for simulation B6 at $z = 10$. The mean free path converges in the optically thin limit where $\lambda \gtrsim s$ but begins to deviate strongly during the transition to the optically thick transition when λ approaches s. It is clear from the plot that an erroneous value for λ would be obtained for an improper choice of s. The convergence of λ in the optically thin limit shows that our choice of picking s to be bounded by $\lambda/5$ is robust in changing this fraction by a factor of a few.
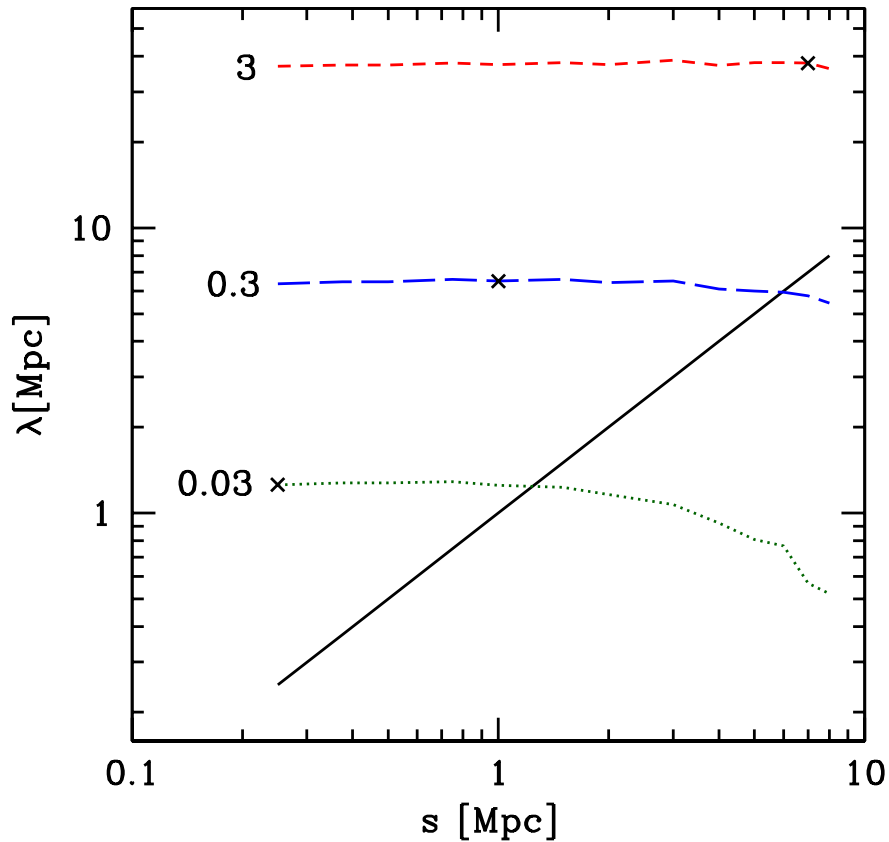
Figure 2.3: Here we demonstrate our procedure for choosing the optimal ray length that adequately samples the IGM while remaining optically thin. The data pertains to simulation B6 (512^3, 8 Mpc) taken at redshift $z = 10$. The nearly horizontal lines show λ as a function of ray length s for different photoionization rates where the labels denote Γ_{-12} in units of 10^{-12} s^{-1}. For each of these lines, the optimal ray length is chosen as the largest value of s for which $s \leq \lambda(s)/5$ and is denoted by a black cross. For comparison, the diagonal line traces out $\lambda = s$ so that portions rightward of this curve belong to the optically thick regime where the mean free path changes significantly.

2.4   Simulation Results

We first describe the dependence of clumping factor, c_l, of ionized gas on redshift and photoionization rate. Next, we use the gas PDF matched to the clumping factors we have obtained, to define a critical overdensity, Δ_{crit}, above which gas remains self-shielded and neutral. The opacity of the IGM to ionizing radiation, expressed in terms of the mean free path, λ, is described next. We first discuss its overall properties and then show how it can be used to relate the emissivity of ionizing sources to the photoionizing background that they produce. Finally, we compare the clumping factors and mean free paths obtained here to those which would be expected for an optically thin model of the IGM.

The main goal of this work is to assess the small-scale convergence of numerical quantities during the initial phase of reionization. This is presented in §2.5 where we show simulation C3 (1024^3, 1 Mpc) to be our "converged" simulation. However, since C3 was only evolved to $z = 10$, we show here results from our fiducial simulation B2 (512^3, 0.5 Mpc) in order to present results down to $z = 6$. Table 2.2 summarizes the clumping factors, critical overdensities, and mean free paths at select redshifts and photoionization rates for simulation B2. These values are within 6% of those from the converged simulation C3 for all $z \geq 10$.

2.4.1   Clumping Factor

Studies of reionization typically make use of the clumping factor of ionized gas, defined as

$$c_l \equiv \langle n_e^2 \rangle / \langle n_e \rangle^2, \tag{2.11}$$

where n_e is the number density of free elections and angled brackets denote volume averages over space. The clumping factor describes the enhancement of the recombination rate relative to a uniform gas distribution, and is therefore crucial in understanding the role of inhomogeneities in the ionizing photon budget during and after reionization.

Before proceeding to discuss the clumping factors obtained here, it is first useful to make some comments regarding the form of equation (2.11). This equation involves a volume average over the free electron density in each ray segment of the box without applying any density cutoffs in considering which electrons contribute to recombinations within the IGM. We have made this choice to facilitate the use of equation (2.12) which allows us to determine the critical overdensity required for self-shielding within a patch of the IGM that does not contain any reionizing sources. This can then be applied in studies that simulate self-shielding by turning off an optically thin flux above a threshold overdensity. Another choice would be to compute the clumping factor based only on gas with overdensity below some cutoff that is assumed to represent the maximum density for which recombinations occur within the IGM. This is ideal for the scenario where one is interested in separating recombinations occurring within the IGM from those occurring within the interstellar medium (ISM) of ionizing sources. The latter can be accounted for through the use of an escape fraction describing the fraction of ionizing photons that escape the ISM of reionizing sources into the surrounding IGM. It is important to note that the numerical value obtained for the clumping factor depends on the particular definition that is used. Regardless, the convergence tests described in §2.5, which are based on the clumping factor described above, remain robust to whatever definition of clumping factor is assumed. For more detailed discussions of the clumping factor and comparisons between different definitions we refer the reader to the recent works of Shull et al. (2012) and Finlator et al. (2012).

We now proceed to discuss the clumping factor obtained from the radiative transfer calculations performed on our fiducial simulation B2. This is shown in Figure 2.4 where we plot c_l
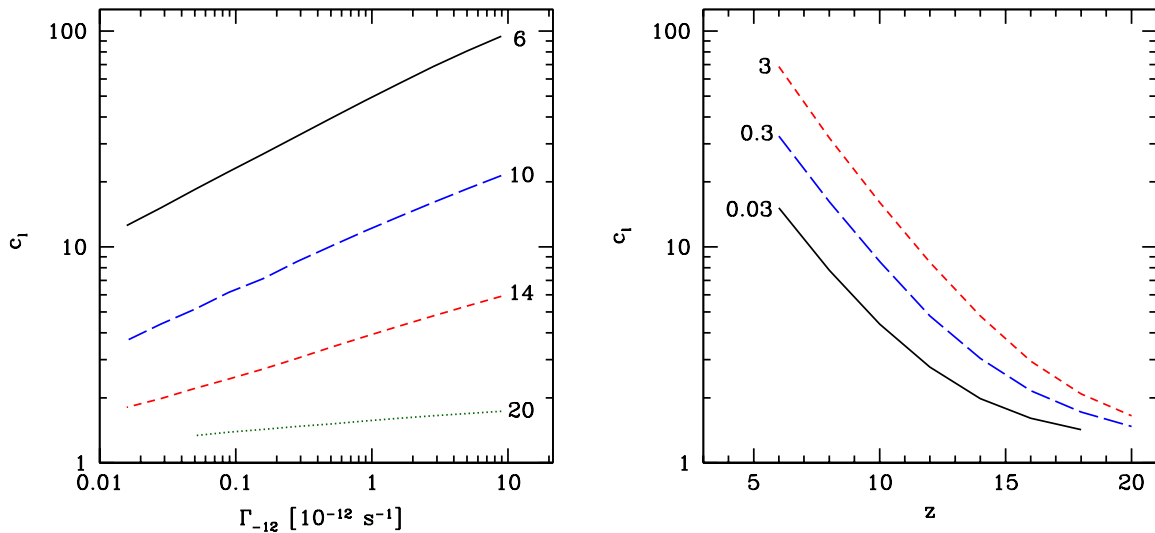
Figure 2.4: (left) Clumping factor versus photoionization rate Γ_{-12} in units of 10^{-12} s^{-1} for different redshifts, as labelled beside the curves. (right) Clumping factor versus redshift for different photoionization rates with labels denoting the value of Γ_{-12}. In both cases the data pertains to our fiducial simulation B2 (512^3, 0.5 Mpc) and regions of parameter space ($z > 18$ and $\Gamma_{-12} < 0.05$) that do not satisfy the ray length criterion described in §2.3.2 are omitted.

for a variety of redshifts and fluxes. Some general trends of the clumping factor are shown by comparing the two panels of this figure. In the first place, at fixed photoionization rate, c_l increases with decreasing redshift which is consistent with ongoing structure formation within the IGM. Furthermore, at fixed redshift, c_l increases with the strength of the ionizing background as the flux of ionizing photons are able to penetrate further into thick gas clouds, exposing their dense interiors where the recombination rate is greatest. Eventually, at large enough flux of $\Gamma_{-12} \gtrsim 1000$, the clumping factor plateaus as the ionization state of the box saturates and all the gas has been ionized. At this point c_l tends to the total clumping factor of gas in the box as n_e approaches n.

Historically, clumping factors of $c_l \sim 30$ at $z \sim 6$ have been found to be appropriate (e.g., Gnedin & Ostriker, 1997), though more recently there has been a growing trend towards values an order of magnitude smaller. It thus appears contrary to historical development that we reproduce $c_l \sim 30$ at $z = 6$ with our fiducial case of $\Gamma_{-12} = 0.3$, and find even larger values with increased flux. However, as explained by Pawlik et al. (2009), the passage of an ionization front through the IGM will photoevaporate the smallest halos in the box and consequently suppress the evolution of the clumping factor at small scales as the gas is dispersed back into the diffuse IGM. Since we do not include such hydrodynamic feedback processes in our analysis, the values reported here cannot be used in reference to an IGM that has been heated through photoionization. Nevertheless, our values are perfectly applicable to the early stages of reionization, before the gas has had time to respond to the ionizing radiation field. Moreover, as

Table 2.2: Opacity of the Unheated IGM at Select Values

z	Γ_{-12} [10^{-12} s^{-1}]	c_l	Δ_{crit}	n_{crit} [cm^{-3}]	λ [Mpc]
18	0.03	1.4	6.1	0.008	0.1
14	0.03	2.0	14	0.009	0.3
10	0.03	4.4	34	0.008	0.7
8	0.03	7.8	55	0.007	1.1
6	0.03	15	100	0.006	2.1
18	0.3	1.7	25	0.031	0.9
14	0.3	3.0	52	0.032	1.6
10	0.3	8.6	120	0.029	3.0
8	0.3	16	200	0.027	4.5
6	0.3	33	390	0.025	8.3
18	3	2.1	110	0.14	7.1
14	3	4.8	210	0.13	10
10	3	16	470	0.11	15
8	3	32	760	0.10	21
6	3	68	1400	0.09	36

discussed in §2.6, previous simulations have underestimated the clumping factor by a factor of ~ 3 during this period, and may therefore be underestimating its subsequent evolution and the impact that unresolved small-scale structure had in regulating the early stages of reionization.

2.4.2 Critical Overdensity for Ionization

Since the clumping factor describes the distribution of ionized gas within the volume, it is in principle derivable from knowledge of the gas PDF and details of the photoionizing radiation field. In a simplified description, we assume that all gas within the box with overdensity $\Delta < \Delta_{\mathrm{crit}}$ is ionized, while the rest is neutral. This is obviously an idealized description of reality where a gradual transition between ionized and neutral regions will necessarily occur. Any departures from the simplified model reflect variations in the local ionizing background and degree of self-shielding and shadowing within the inhomogeneous IGM (Miralda-Escudé et al., 2000).

In the simplified model the clumping factor of ionized gas is related to the total gas PDF through the following expression:

$$c_l = \frac{\int_0^{\Delta_{\mathrm{crit}}} \Delta^2 P(\Delta) \, d\Delta}{\left(\int_0^{\Delta_{\mathrm{crit}}} \Delta P(\Delta) \, d\Delta \right)^2}, \tag{2.12}$$

where Δ_{crit} is interpreted as the critical overdensity above which self-shielding prevents the gas from becoming ionized. It is often useful to assume the form of equation (2.12) taken with some nominal choice for Δ_{crit} in order to compute c_l from a given gas PDF. For example, Chiu et al. (2003) consider a model where all gas within collapsed halos is self-shielded while all

remaining gas is subject to ionization from an UVB. In this case, $\Delta_{\text{crit}} = 6\pi^2$ corresponding to the overdensity at the virial radius of an isothermal sphere with a mean overdensity of $\Delta_{\text{vir}} = 18\pi^2$.

Since we compute the clumping factor directly from our radiative transfer calculations, we take the opposite approach, inverting equation (2.12) in order to compute Δ_{crit} from knowledge of $P(\Delta)$ and c_l. In doing so, we observe the expected trend that Δ_{crit} increases when the photoionization rate is increased, making the medium more susceptible to ionization. In fact, we find the rough proportionality $\Delta_{\text{crit}} \propto \Gamma_{-12}^{2/3}$ which, from equation (4) of McQuinn et al. (2011), is expected for a PDF satisfying $P(\Delta) \propto \Delta^{-2.5}$. We showed in Figure 2.2 that our PDFs satisfy this power-law at $z \lesssim 10$ for $\Delta > \Delta_{\text{vir}}$. This is consistent with the model where gas at these densities is collapsed in isothermal spheres. Around our fiducial value of $\Gamma_{-12} = 0.3$, we further find that Δ_{crit} is roughly proportional to $(1+z)^{-3}$, indicating that the critical proper hydrogen number density, n_{crit}, is rather insensitive to redshift. A good value to take is $n_{\text{crit}} \sim 0.1 \text{ cm}^{-3} \, \Gamma_{-12}^{2/3}$.

The validity of the idealized model where all gas with overdensity $\Delta < \Delta_{\text{crit}}$ is ionized is tested in Figure 2.6. Here we plot the total gas PDF along with the ionized and neutral PDFs obtained from our radiative transfer calculation using our fiducial parameters $\Gamma_{-12} = 0.3$ and $z = 10$ for simulation B2. The vertical dot-dashed line shows the corresponding value of Δ_{crit} – its role in delineating the neutral and ionized portions of the gas is clearly visible. As anticipated, the transition between ionized and neutral regions is not sharp, but rather gradual as a consequence of the spatially varying ionizing background and self-shielding due to dense gas pockets. Nevertheless, our findings indicate that the approximation that Δ_{crit} represents the critical overdensity above which self-shielding maintains the neutral state of the IGM is generally a good one.

2.4.3   Mean Free Path

We quantify the opacity of the IGM to the exposed UVB through the use of the mean free path of ionizing radiation. Conceptually, one can consider the mean free path to be affected by two components: a diffuse gaseous phase that pervades the IGM and thick gas clouds embedded within collapsed dark matter halos. The latter make up a significant fraction of absorption systems that have neutral hydrogen column densities $N_{\text{HI}} \gtrsim 1/\bar{\sigma} \approx 10^{17} \text{ cm}^2$ allowing them to self-shield against ionizing radiation. It is within these optically-thick structures where the global recombination rate of the IGM is dominated and the majority of ionizing photons are absorbed (Miralda-Escudé et al., 2000). As a result, they can significantly impede the progress of reionization.

The mean free path obtained from our radiative transfer calculations is computed through the use of equation (2.10) which naturally encompasses both the clumpy IGM and halo components. In Figure 2.5 we plot the mean free path as a function of photoionization rate for fixed redshift and also as a function of redshift for fixed photoionization rate. Some general trends
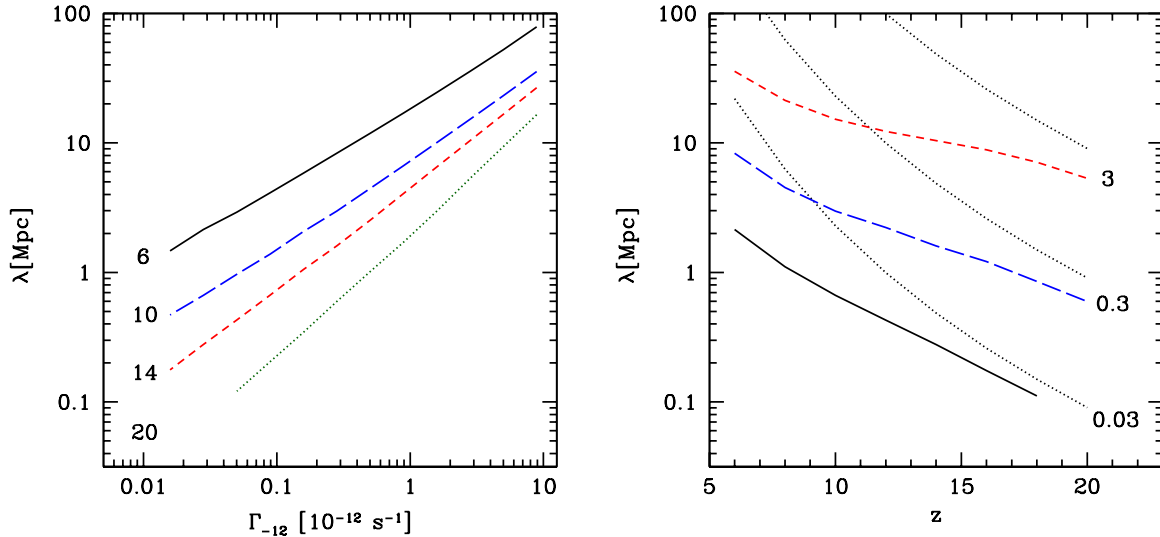
Figure 2.5: (left) The mean fee path versus photoionization rate Γ_{-12} in units of 10^{-12} s^{-1} for different redshifts, as labelled. (right) Mean free path versus redshift for different photoionization rates with labels indicating the value of Γ_{-12}. In both cases the data pertains to our fiducial simulation B2 (512^3, 0.5 Mpc) and regions of parameter space ($z > 18$ and $\Gamma_{-12} < 0.05$) that do not satisfy the ray length criterion described in §2.3.2 are omitted. The dotted black curves in the right panel show the mean free path expected for an optically thin, completely ionized, and homogeneous IGM as expressed in equation (2.17). From bottom to top in the plot, the dotted lines take $\Gamma_{-12} = 0.03$, 0.3, and 3, and are each calculated using $x = c_l = 1$. We expect the dotted lines to converge with our results at high redshift when the medium approaches homogeneity. At low redshift we observe a large suppression in the calculated mean free path that results from increased structure formation within the inhomogeneous IGM.

are immediately clear in this plot. In the first place, at fixed redshift we see that the mean free path increases with the strength of the ionizing background. A stronger flux of ionizing photons will naturally penetrate further through a diffuse IGM and overcome thicker self-shielding structures, consistent with the previous observation that $\Delta_{\mathrm{crit}} \propto \Gamma_{-12}^{2/3}$. In addition, when the ionizing background is held constant, the mean free path is found to increase with decreasing redshift.

It is important to note that there are two competing factors affecting the redshift evolution of λ. On the one hand, the expansion of the Universe continually dilutes the density of hydrogen, hence favouring a strong increase in λ with decreasing z. On the other hand, increased structure formation at low redshift enhances the distribution of Lyman-limit systems that strongly inhibit the distance an ionizing photon can propagate through the IGM before being absorbed. In the right panel of Figure 2.5 we compare λ obtained here to equation (2.17) for the same set of photoionization rates. Taking $x = c_l = 1$ in this equation yields the mean free path we would obtain in an optically thin, homogeneous, and completely ionized medium. In such a model the mean free path evolves rapidly with redshift as $\lambda \propto (1+z)^{-5}$. Instead, we observe a strong

Table 2.3: Power law index of $\Gamma \propto \dot{n}_{\mathrm{ion}}^{\gamma}$

	z							
	6	8	10	12	14	16	18	20
γ	2.6	2.9	3.1	3.7	4.5	6.7	10	14

suppression in mean free path at low redshift compared to equation (2.17). This highlights the important contribution from inhomogeneities in the IGM.

2.4.4   Relationship Between Emissivity and Photoionization Rate

In the context of reionization it is desirable to know the ionizing background produced by some population of sources with known emissivity. This relationship can be found by solving

$$\Gamma = \dot{n}_{\mathrm{ion}}(1 + z)^2 \lambda(\Gamma, z)\bar{\sigma}, \tag{2.13}$$

where $\dot{n}_{\mathrm{ion}}$ is the comoving ionizing emissivity and $\lambda(\Gamma, z)$ is the comoving mean free path that depends on both the ionizing background and redshift. In Figure 2.7 we show the dependence of Γ on $\dot{n}_{\mathrm{ion}}$ by solving equation (2.13) with the mean free paths taken from our radiative transfer calculations. We find that Γ exhibits a rather steep dependence on emissivity and appears to diverge at large values of $\dot{n}_{\mathrm{ion}}$. This behaviour is attributed to the fact that not only are there more ionizing photons as the emissivity rises, but also their ability to penetrate further through the IGM increases.

We can relate this behaviour back to the dependency of λ on Γ. For instance, suppose we have the simple relation $\lambda \propto \Gamma^{\beta}$ at some redshift. Then from equation (2.13) we will have that $\Gamma \propto \dot{n}_{\mathrm{ion}}^{\gamma}$ where $\gamma = (1-\beta)^{-1}$. In Table 2.3 we list the values of γ obtained by fitting a power-law to our fiducial mean free paths within the range $0.1 \leq \Gamma_{-12} \leq 1$ at different redshifts. This flux range is considered to emphasize the relationship between Γ and $\dot{n}_{\mathrm{ion}}$ around our fiducial value of $\Gamma_{-12} = 0.3$. We find that the relationship between Γ and $\dot{n}_{\mathrm{ion}}$ strengthens as the redshift increases – γ varies from 2.6 to 14 between redshifts 6 and 20 respectively. This occurs because the slope β rises as the IGM becomes more uniform, approaching a limiting value of unity for a completely homogeneous Universe with $c_l = 1$ in equation (2.17) – a manifestation of "Olber's Paradox".

From this trend we can deduce that decreasing the simulation resolution should steepen the curves in Figure 2.7 as the density distribution becomes more homogenous. Indeed, this relation is observed between our suite of simulations where we find $\gamma = 3.2$ at $z = 6$ for our worst-resolved simulation A6 (256^3, 8 Mpc), compared to $\gamma = 2.6$ for simulation B2. McQuinn et al. (2011) report the value of $\gamma \sim 4$ at $z = 6$. The discrepancy with our result likely arises from a combination of our increased resolution and our omission of photoheating which would suppress accretion of gas onto low-mass halos and promote homogeneity.

The photoionization rate after reionization can be derived from measurements of the Lyα
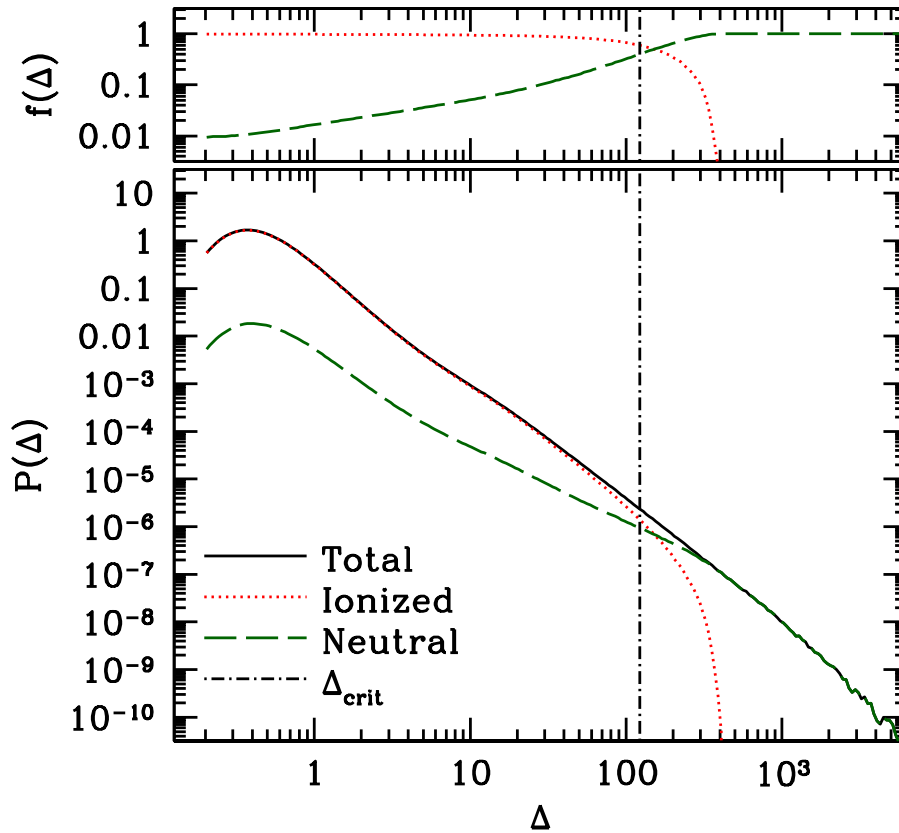
Figure 2.6: The bottom panel compares the total gas PDF of our fiducial simulation B2 (512^3, 0.5 Mpc) to the PDFs of neutral and ionized gas within the box after radiative transfer is applied. Ray segments are labelled as ionized if they have an ionized fraction greater than 0.5 and are labelled neutral otherwise. The data corresponds to a snapshot at $z = 10$ with an ionizing background of $\Gamma_{-12} = 0.3$. The vertical dot-dashed line denotes Δ_{crit} determined by comparing c_l obtained from the radiative transfer calculation to the total gas PDF through equation (2.12). The top panel shows the corresponding volume fraction of neutral and ionized gas as a function of Δ.

forest. This was done by Kuhlen & Faucher-Giguère (2012) who list the values of Γ and $\dot{n}_{\mathrm{ion}}$ for redshifts between 2 and 6. The quoted values at $z = 6$ are $\Gamma_{-12} < 0.19$ and $\dot{n}_{\mathrm{ion}} < 2.6 \times 10^{50}$ s^{-1} Mpc^{-3}. Looking at Figure 2.7 we see that our $z = 6$ curve predicts an emissivity an order of magnitude too large when $\Gamma_{-12} = 0.19$. As we discuss in §2.6, our results at $z \lesssim 10$ are hindered by the omission of radiative feedback that would otherwise smooth inhomogeneities on small scales. Photoheating suppresses structure growth within the IGM thereby increasing the mean free path at fixed conditions as ionizing photons travel further before encountering an optically thick absorption system. From equation (2.13) a larger mean free path produces a higher ionization rate at fixed emissivity, implying that the $z = 6$ curve in Figure 2.7 would shift upwards in the presence of heating. If this shift were to bring us into agreement with
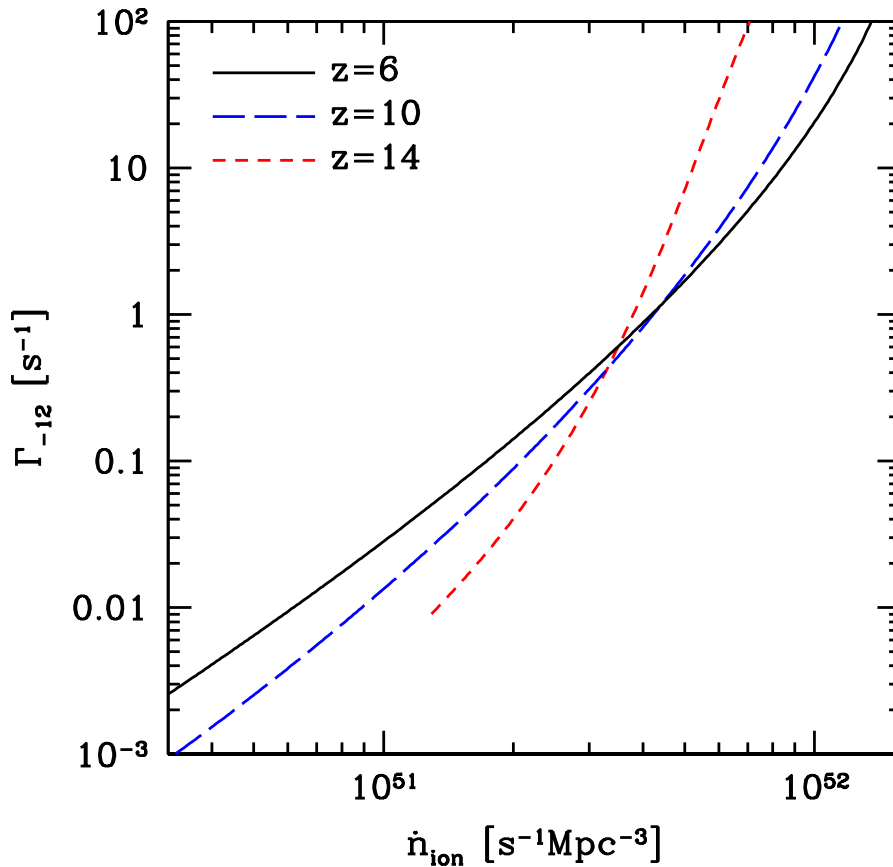
Figure 2.7: The photoionization rate, expressed in terms of Γ_{-12}, as a function of the comoving ionizing emissivity at different redshifts. These curves are evaluated by solving equation (2.13) using $\lambda(\Gamma, z)$ obtained from our radiative transfer calculations performed on our fiducial simulation B2 (512^3, 0.5 Mpc). At low flux we truncate the $z = 14$ curve when it enters the optically thick domain where it no longer satisfies the ray length criterion described in §2.3.2.

observations we would require that our calculated mean free path at $\Gamma_{-12} = 0.19$ increase by an order of magnitude to allow for an order of magnitude reduction in the emissivity required to produce such a background. In Figure 2.5 we find $\lambda \approx 7$ Mpc at $z = 6$ for $\Gamma_{-12} = 0.19$. This means that a mean free path of 70 Mpc would be required in a *heated* IGM to bring us into agreement with observations of the Lyα forest. This is in reasonable agreement with the value of $\lambda = 49 \pm 14$ Mpc reported by Kuhlen & Faucher-Giguère (2012) as the mean free path at the Lyman edge. Note that at redshifts $z \gtrsim 10$, before photoheating is important, the curves in Figure 2.7 should be correct. Of course, reionization becomes patchy at high redshift, making a description in terms of an IGM with a single UVB flux and mean free path less accurate.

The strong scaling relations observed here suggest that small changes in $\dot{n}_{\rm ion}$ can boost Γ by substantial amounts. McQuinn et al. (2011) use this to argue that the rapid evolution in Γ observed by Fan et al. (2006) at $z \approx 6$ can be explained by a small change in the emissivity of the ionizing background rather than attributing this effect to the overlap phase of reionization.

2.4.5   Relationship Between Mean Free Path and Clumping Factor

Suppose there is an infinitesimally thin slab of width ds whose area element dA is exposed to some flux F. In ionization equilibrium, the number of ionizations occurring per unit time balance the number of recombinations:

$$dFdA = \alpha_B n_e n_{\text{HII}} dA ds, \tag{2.14}$$

where dF is the attenuation of flux passing through the slab. Dividing both sides of this expression by $dAds$, substituting equation (2.9), and taking $n_e = n_{\text{HII}}$ implies

$$F(1+z)/\lambda = \alpha_{\text{B}} n_e^2. \tag{2.15}$$

Finally, taking the clumping factor defined in equation (2.11) and the ionized fraction $x \equiv \langle n_e \rangle / \langle n_H \rangle$ we obtain:

$$F(1+z)/\lambda = c_l \alpha_{\text{B}} x^2 \langle n_H \rangle^2. \tag{2.16}$$

For an ionized gas temperature of $T_{\text{gas}} = 10^4$ K,

$$\lambda \simeq \frac{23 \text{ Mpc}}{x^2 c_l} \left(\frac{\Gamma_{-12}}{0.3 \ 10^{-12} \ \text{s}^{-1}} \right) \left(\frac{1+z}{11} \right)^{-5}, \tag{2.17}$$

where we have made use of equation (2.4) for the conversion from flux to photoionization rate.

In Figure 2.8 we plot c_l versus λ and $x^2 c_l$ versus λ from our radiative transfer calculations at $z = 10$ with $\Gamma_{-12} = 0.3$ for each of the simulations listed in Table 2.1. In each panel the dotted line traces equation (2.17) that we would expect for an optically thin IGM exposed to the given flux. The overall agreement between λ and the simulation points in the bottom panel indicates consistency in the definition of the mean free path and detailed balance between absorptions and ionizations. The minor deviations between the data points and the dotted curve arise because our rays have a finite length, s, so the mean free path evaluated in equation (2.17) will not correspond exactly to equation (2.10), which is strictly correct only in the limit where $s \longrightarrow 0$.

The simulations span a large range of values in Figure 2.8 with c_l ranging from 2.6 to 8.8 and λ from 2.9 to 9.5 Mpc. This spread arises from the broad variation in spatial and mass resolution exhibited by the suite of simulations. In spite of this, there is a clear grouping of points at $c_l \sim 8$ and $\lambda \sim 3$ Mpc. This reflects the trend towards numerically converging to the "correct" clumping factor and mean free path and is our next topic of focus.

2.5   Numerical Convergence

In this section, we attempt to answer the following question: *What mass resolution and box sizes are necessary in cosmological hydrodynamics simulations, in order to obtain accurate re-*
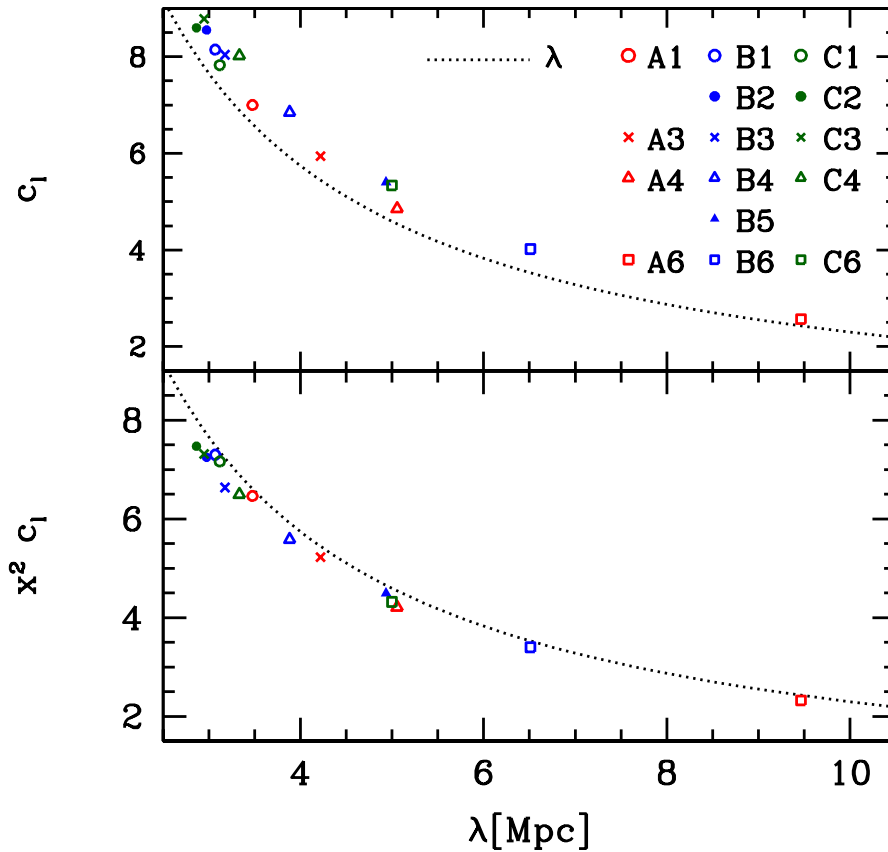
Figure 2.8: c_l versus λ (top panel) and $x^2 c_l$ versus λ (bottom panel) for all simulations taken at $z = 10$ with a photoionization rate $\Gamma_{-12} = 0.3$. In each panel points denote simulation values according to the legend in the top right corner of the plot. Traced by the dotted line is equation (2.17) which describes the relationship between mean free path and clumping factor for an optically thin IGM.

sults for the inhomogeneity of an unheated IGM? Clearly, simulations must have sufficient mass resolution to resolve the internal structure of the lowest mass halos that can contain gas. In addition, however, such simulations must cover a large enough volume to contain a representative sample of the low-mass halos that dominate the opacity of the IGM.

In Figure 2.9 we plot the clumping factors and mean free paths obtained from the radiative transfer calculations performed on each of the simulations listed in Table 2.1. To obtain a picture of convergence we display how c_l and λ vary as functions of simulation box size, L, (left panels) and dark matter particle mass, $m_{\rm dm}$, (right panels) for our fiducial redshift $z = 10$ and photoionization rate $\Gamma_{-12} = 0.3$. Though the discussion below pertains explicitly to these fiducial values we have checked that the picture remains consistent for $10 \leq z \leq 20$ and $0.01 \leq \Gamma_{-12} \leq 10$.

Starting in the top right panel of Figure 2.9 we show how c_l changes as the mass resolution of the simulations is varied. As expected, the clumping factor increases as the resolution is refined
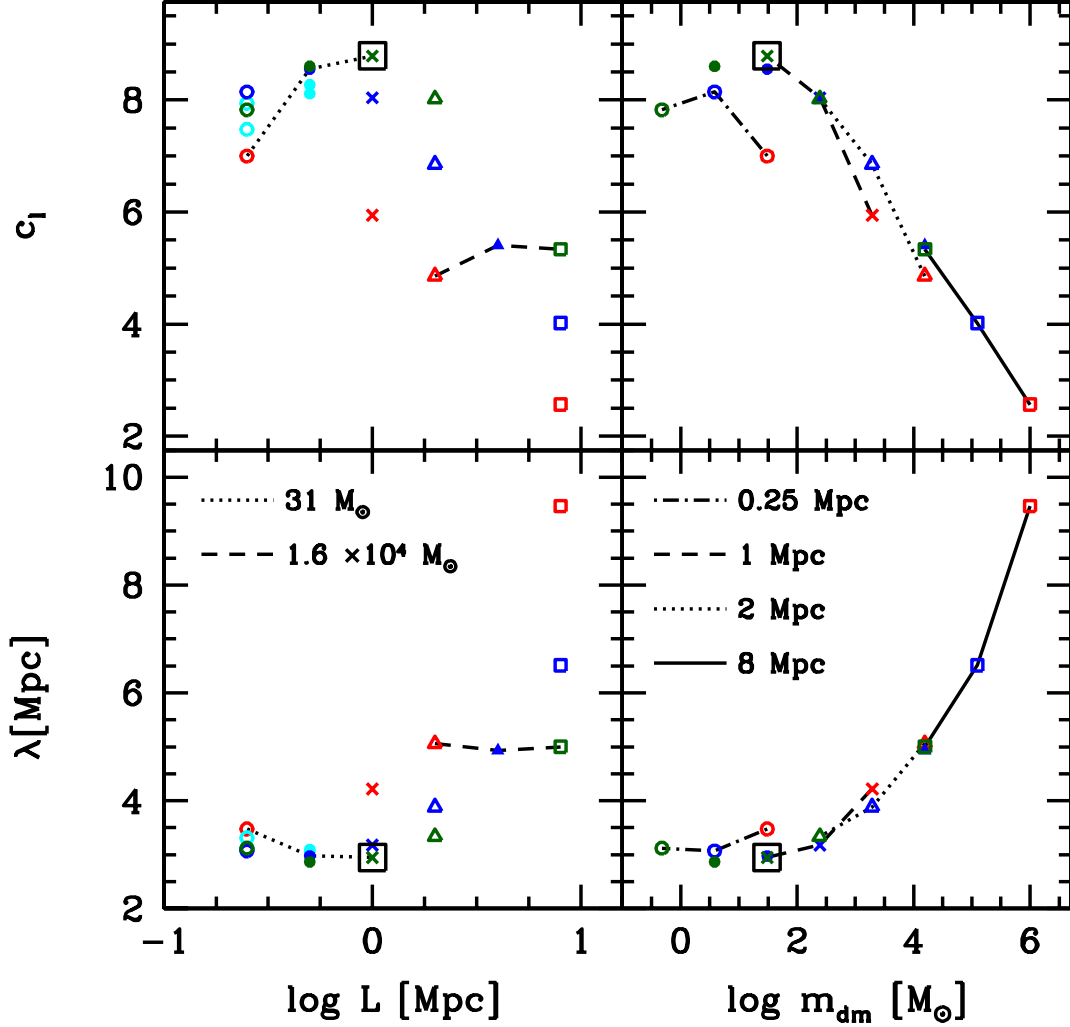
Figure 2.9: Clumping factor and mean free path versus simulation box size (left panels) and dark matter particle mass (right panels) for $z = 10$ and $\Gamma_{-12} = 0.3$. In each panel point types distinguish between different simulations and follow the legend in Figure 2.8. Lines in the left panels connect simulations with fixed particle mass, while lines in the right panels connect simulations with fixed volume. The converged simulation C3 (1024^3, 1 Mpc) is denoted by a green cross and is highlighted by a black square for easy identification. In the two left panels, open cyan circles and closed cyan circles denote the values of c_l and λ obtained from different random realizations of simulations B1 and B2 respectively.

and begins to plateau to a common value of $c_l \sim 8.8$ at $m_{\mathrm{dm}} \sim 30~M_\odot$, when a sufficiently low particle mass required to resolve the smallest gaseous structures in the box is reached. Simulations with larger particle mass are unable to resolve the smallest inhomogeneities contributing to the clumpiness of the IGM and consequently imply clumping factors up to a few times smaller than the converged result. In the opposite limit we find that simulations with $m_{\mathrm{dm}} < 5~M_\odot$ are

also yielding smaller clumping factors of $c_l \sim 8$. This appears counterintuitive at first glance since these simulations should have no problem resolving the Jeans scale of the IGM. However, their inability to converge on c_l is attributed to their small box size, as explained below. The three smallest simulations with $L = 0.25$ Mpc are connected by a dot-dashed line and all display conspicuously unconverged values.

The dependence of clumping factor on box size is shown in the top left panel of Figure 2.9. In this case we expect to find a minimum box size above which simulations converge on c_l. Smaller boxes fail to capture power from large-scale modes and should therefore have reduced clumping factors. Larger boxes that are able to capture a representative collection of absorption systems within their volume should converge provided that they have sufficient mass resolution. These general trends can be identified by the behaviour shown in the top left panel of Figure 2.9. There is a clear convergence of points near $L \sim 1$ Mpc and $c_l \sim 8.8$ with c_l falling off on either side. Simulations with $L \lesssim 1$ Mpc have insufficient volumes to converge with this result, while those with $L \gtrsim 1$ Mpc have insufficient mass resolutions. Convergence occurs in the middle ground where both a sufficient volume and mass resolution are attained.

We find similar behaviour by comparing how λ changes between simulations. From the bottom panels of Figure 2.9 we see that the resultant behaviour is essentially an inversion of that described for c_l. Firstly, simulations with coarse mass resolutions overestimate λ. These runs are unable to resolve small-scale inhomogeneities and the degree of self-shielding that would otherwise inhibit the propagation of ionizing photons through neutral patches of the IGM. Secondly, the smallest boxes also produce values of λ that are too large. As mentioned above, these simulations underproduce the collection of halos that shield against the propagation of an ionization front through the IGM.

The simulations shown here have relatively small volumes in a cosmological context. One issue that must be considered with these small boxes is that of sample variance. In the left panels of Figure 2.9, we plot c_l and λ obtained from simulations B1 (512^3, 0.25 Mpc) and B2 (512^3, 0.5 Mpc) that were run using two different random realizations of the same initial density field. The clumping factors over all three random realizations vary by 9% and 5% for B1 and B2 respectively, indicating that sample variance is somewhat important within these volumes. This may explain the unexpected result that c_l for simulation C1 (1024^3, 0.25 Mpc) is smaller than that of simulation B1. Normally, at fixed volume, increasing the mass resolution should enhance the clumping factor (e.g., as seen by comparing c_l between simulations A3, B3, and C3, which are connected by the dashed curve in the top right panel of Figure 2.9). However, we may not expect to observe this trend with only one realization of a small box with large sample variance, and must also keep this in mind when interpreting the results of our convergence test.

The above results indicate that convergence in c_l and λ is attained by simulation C3 (1024^3, 1 Mpc) with $m_{\mathrm{dm}} = 31 \ M_{\odot}$. This simulation has a fine enough mass resolution to resolve small-scale inhomogeneities, and has a large enough volume that sample variance should be unimportant and large-scale modes should be captured. In order to make this claim more

rigorous we would have to compare against a box with larger volume and finer particle mass than currently feasible. Nevertheless, the data presented in Figure 2.9 provides compelling evidence that numerical convergence is being approached, and we suspect that deviations in our values for c_l and λ from their "true" values are small enough to claim convergence in simulation C3. Based on this we find that the necessary requirements for describing the inhomogeneity of an unheated IGM using cosmological hydrodynamics simulations is to use box sizes $L \gtrsim 1$ Mpc with dark matter particle masses $m_{\rm dm} \lesssim 50~M_\odot$. Smaller boxes are troubled by sample variance while coarser mass resolutions are unable to resolve the mass scale where gaseous halos are dominating the opacity of the IGM.

2.6 Discussion

We have performed high-resolution, cosmological simulations of structure formation at redshifts $z > 6$, including adiabatic hydrodynamics. By post-processing the resulting density fields with a radiative transfer algorithm for hydrogen ionizing radiation, we have determined the opacity of the unheated IGM, in terms of the mean free path to ionizing radiation, λ, as a function of redshift and ionizing background intensity. These results are relevant (1) as converged solutions for the opacity of the IGM early in the reionization process, before photoheating has evaporated small-scale structure and (2) in determining what mass and length resolutions are necessary to correctly model the propagation of ionization fronts into the neutral IGM. We derive values of $n_{\rm crit}$, the proper hydrogen number density above which gas remains neutral, that are for the most part a function of only Γ_{-12}. Simulations that mimic the effect of self-shielding by turning off the optically-thin flux at high densities should use $n_{\rm crit} \sim 0.1~{\rm cm}^{-3}~\Gamma_{-12}^{2/3}$, independent of redshift.

Our post-processing approach neglects the hydrodynamic feedback of photoheating on the density evolution. These results therefore indicate what the initial degree of inhomogeneity should be as ionization fronts propagate into the IGM. In addition, they place an upper limit to this inhomogeneity in patches of the IGM that have already been ionized. We find that the initial clumping factor of the IGM just as it is being ionized is a strong function of redshift and ionizing background intensity, with typical values at $z = 10$ ranging from about $c_l = 4.4$ to 16 and $\lambda = 0.7$ to 15 Mpc, for $\Gamma_{-12} = 0.03$ to $\Gamma_{-12} = 3$, respectively.

Modelling the transition from a neutral to ionized IGM requires self-consistent simulations of the coupled radiative transfer and hydrodynamical photoevaporation process. Shapiro et al. (2004) used idealized two-dimensional radiative transfer hydrodynamics calculations of the photoevaporation of initially spherical, isolated minihalos, surrounded by infalling gas. Those calculations showed that smaller minihalos are photevaporated faster, and that larger fluxes lead to faster photoevaporation times as well. Iliev et al. (2005b) extended these models to show that the typical timescale for minihalo photoevaporation is $t_{\rm ev} \sim 10 - 100$ Myr. This is comparable to the recombination time $t_{\rm rec} = 1/(c_l \alpha_B \langle n_H \rangle) \sim 100$ Myr at $z \sim 10$ for a clumpy IGM with

$c_l = 10$. This suggests that Jeans smoothing of the IGM occurs before recombinations have had time to significantly disturb the reionization process. The amount by which recombinations occurring within minihalos could delay reionization was studied by Ciardi et al. (2006) who performed numerical simulations using the results of Iliev et al. (2005b) as a subgrid model for minihalo absorption. For the extreme case where Jeans smoothing fails to suppress minihalo formation they place $\Delta z \sim 2$ as the upper limit to the redshift delay of reionization induced by minihalos. For the opposite and more physically realistic case where minihalo formation is heavily suppressed by photoionization they find only a modest impact on reionization with a volume averaged ionized fraction that is $\lesssim 15\%$ lower than the case where minihalo recombinations are ignored.

However, the photoevaporative process is in reality likely to be more complex than for the simplified geometries and source lifetimes considered by Shapiro et al. (2004), with halos over a range of masses clustered in space and arranged within a "cosmic web" of filamentary structure. Filamentary infall from nearby neutral gas could replenish halos as they are being evaporated, considerably extending the photoevaporation process, while ionization from highly luminous but intermittent starburst galaxies could result in large clumping factors and stalled minihalo evaporation, considerably increasing photon consumption and leading to a much more complex morphology of early H II regions (e.g., Wise et al., 2012) than is typically envisioned.

A possible scenario that we have not considered here is the suppression of gas clumping at early times due to the presence of high-redshift X-ray sources (see, e.g., Haiman, 2011). These may be associated with traditional X-ray sources like supernova or by more exotic sources like microquasars (Mirabel et al., 2011). X-rays have a small absorption cross-section meaning that a high-redshift distribution of X-ray sources would expose the IGM to a nearly uniform source of heating, inhibiting minihalo formation and growth at early times (Oh & Haiman, 2003). The result is a warm ($T \sim 1000$ K) and weakly ionized IGM that would later become reionized by the patchy network of star-forming galaxies with softer radiation spectra. In this case the clumping factor would already be reduced at the onset of reionization and the resolution requirements presented here would become less strict. Our convergence criteria may therefore be considered the conservative case where the IGM has not been smoothed by heating processes prior to reionization.

We find that convergence is reached at a dark matter particle mass of $m_{dm} \lesssim 50~M_\odot$. A box size of $L \gtrsim 1$ Mpc is necessary to sample the IGM for the purpose of modelling absorptions by small-scale structure. The clumping factors we find from our converged results are somewhat smaller than the values $c_l \sim 30$ found in early attempts to characterize the clumpiness of the IGM which did not accurately separate ionized and neutral gas (e.g., Gnedin & Ostriker, 1997), but are higher than the clumping factors found by Pawlik et al. (2009) at $z \sim 9$, just before the IGM in those simulations was heated by ionizing radiation. We attribute this difference to the increased mass resolution of our simulations, which resolve halo masses down to the Jeans mass in an *unheated* IGM ($\sim 10^4 M_\odot$), as opposed to that corresponding to the Jeans mass
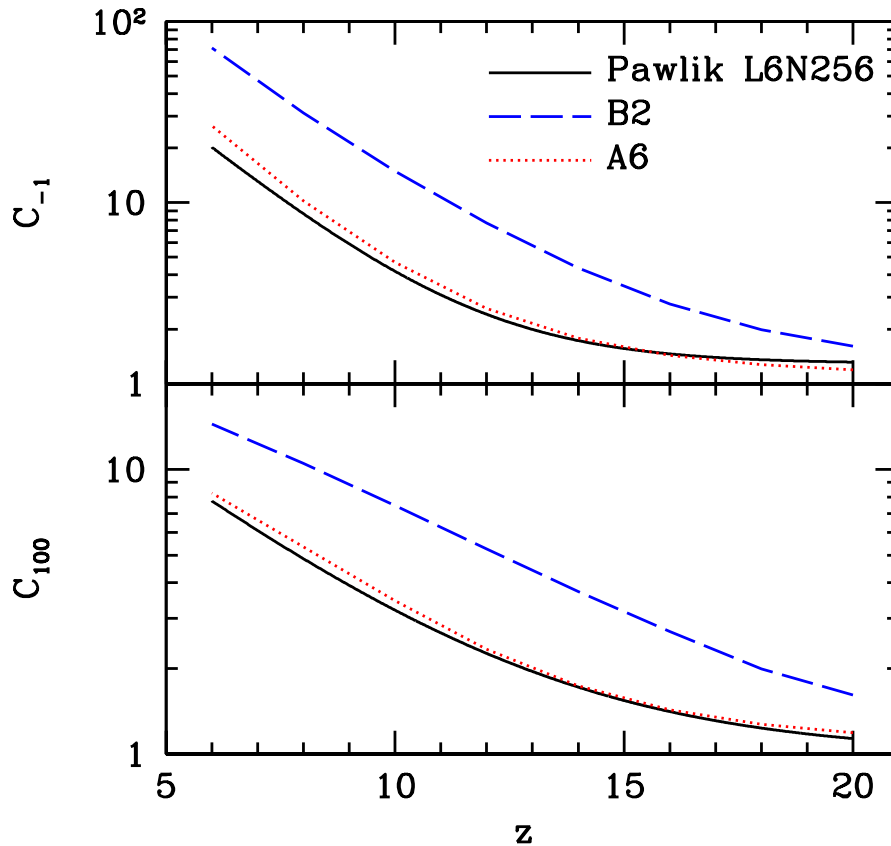
Figure 2.10: Here we compare clumping factors C_{-1} and C_{100} from our fiducial simulation B2 (512^3, 0.5 Mpc) to the Pawlik et al. (2009) simulation L6N256 (256^3, 6 Mpc). The Pawlik et al. curve corresponds to their reference simulation that did not include photoionization and has similar attributes to our simulation A6 (256^3, 8 Mpc). As expected, A6 and L6N256 are in good agreement with each other while the higher-resolved simulation B2 shows clumping factors a few times larger than L6N256.

for a photoionized gas temperature of $\sim 10^4$ K ($\sim 10^8 M_\odot$). As pointed out by Pawlik et al. (2009), the clumping factors they find at $z \sim 6$, for a patch of the IGM which was ionized significantly earlier, at $z \sim 9$, are converged with respect to the Jeans scale of the heated IGM. Their value likely approaches the *correct*[2] value for the post-reionization IGM at $z = 6$ because a long enough time had passed since the gas was ionized for photoheating to evaporate existing small-scale structure and suppress accretion onto newly formed dark matter minihalos with masses below $\sim 10^{8-9} M_\odot$, which were resolved in their highest resolution simulations by $\sim 100 - 1000$ dark matter particles.

Pawlik et al. (2009) demonstrate convergence of their clumping factor for the heated IGM

---

[2]The correctness of the clumping factor depends on the specific physical processes affecting the evolution of baryons within the IGM and on the particular context to which the clumping factor is being used to describe. Here we use the term correct to refer to the value of the clumping factor that would be obtained if the simulation in question had infinite resolution.

while noting that convergence would be more difficult to obtain for an unheated IGM. We have explicitly demonstrated this latter point here and accordingly show that their values for the clumping factor are likely underestimates during the initial stages of reionization, by about a factor of a few. This is illustrated in Figure 2.10 where we compare clumping factors from two of our simulations to the unheated simulation L6N256 of Pawlik et al. Here we plot the clumping factors C_{-1} and C_{100} with this notation being used to emphasize that these clumping factors are evaluated using all gas below some density cutoff. For C_{-1} a physical density threshold of $n_{\mathrm{crit}} = 0.1$ cm^{-3} is used while an overdensity threshold of $\Delta_{\mathrm{crit}} = 100$ is used for C_{100}. These definitions differ from the definition of c_l in equation (2.11) that we have been using so far which involves an average over all ionized gas in the box. In any event, the clumping factors we find in our fiducial simulation B2 are at all times larger, by a factor of 1.2 at $z = 20$ and 3.5 at $z = 6$ for C_{-1}. As described above, the clumping factors we obtain at low redshift are overestimates, and in reality should be closer to $C_{-1} \sim 6$ or $C_{100} \sim 3$ found by Pawlik et al. in the presence of a photoevaporative background. Combining these two results, the clumping factor of the the IGM evolves strongly just after a patch of IGM is ionized. For ionization at $z = 9$, the clumping factor drops from $c_l \sim 20$ at $z = 9$ to a few at $z = 6$, depending on the intensity of the ionizing background – with larger intensities leading to higher clumping factors and larger mean free paths. This strong suppression of the clumping factor due to photoheating was demonstrated by Pawlik et al. who referred to it as a positive feedback on reionization since it reduces the total number of recombinations occurring within small-scale absorption systems.

The results presented here for the inhomogeneity of electron density in the presence of an ionizing background should serve as a foundation for more detailed study of radiative transfer and hydrodynamical effects in the initial stages of reionization, including the effects of the initial relative velocity between baryons and dark matter (e.g., Tseliakhovich & Hirata, 2010), preheating by long mean free path X-ray photons (e.g., Ricotti & Ostriker, 2004; Ricotti et al., 2005), and photoevaporation (e.g., Shapiro et al., 2004; Abel et al., 2007). In simulating all of these processes, it will be necessary to resolve small-scale structure in the way outlined here.

Acknowledgements

Chapter 3

Evolution of low mass galactic subhalos and dependence on concentration

3.1   Chapter Overview

We carry out a detailed study of the orbital dynamics and structural evolution of over 6000 subhalos in the Via Lactea II simulation, from infall to present. By analyzing subhalos with masses down to $m = 4 \times 10^5$ $M_\odot$, we find that lower mass subhalos, which are not strongly affected by dynamical friction, exhibit behaviours qualitatively different from those found previously for more massive ones. Furthermore, there is a clear trend of subhalos that fell into the host earlier being less concentrated. We show that the concentration at infall characterizes various aspects of subhalo evolution. In particular, tidal effects truncate the growth of less concentrated subhalos at larger distances from the host; subhalos with smaller concentrations have larger infall radii. The concentration at infall is further shown to be a determining factor for the subsequent mass loss of subhalos within the host, and also for the evolution of their internal structure in the $v_{\max} - r_{\max}$ plane. Our findings raise the prospects of using the concentration to predict the tidal evolution of subhalos, which will be useful for obtaining analytic models of galaxy formation, as well as for near field cosmology.

3.2 Introduction

The standard model of cosmological structure formation is based upon the notion that the gravitational landscape is dominated by cold dark matter (CDM), which initially collapses on small scales and grows hierarchically to larger scales through the continued merger and accretion of smaller objects. Many of the accreting systems survive to the present epoch as independent entities within their host, giving rise to a system of nested substructure within the largest objects to have formed today. These surviving remnants present a unique opportunity to study the seeds of galaxy formation and the chance to probe the nature of dark matter on small scales.

Accomplishing these goals requires the development of an accurate and predictive theory for the evolution of substructure. This remains a difficult task and a fundamental problem in the burgeoning area of near field cosmology. Even without taking into account the complicating role played by dissipative effects associated with, e.g., star formation and feedback, one must still contend with reconciling the stochasticity in the primordial fluctuations that seed the sub-sructure in any given object, on the one hand, and the highly nonlinear gravitational dynamics associated with tidal disruption and dynamical friction, on the other hand. As is often the case, efforts to tackle this problem generally fall into one of two categories.

First are direct numerical simulations (e.g., Diemand et al., 2008; Springel et al., 2008; Garrison-Kimmel et al., 2014), which attempt to solve the problem *ab initio* from cosmological initial conditions zoomed on a single host. This class of approaches suffers from small number statistics, both in the number of individual objects simulated and in the range of underlying background cosmologies (warm dark matter, self-interacting dark matter, broken scale invariance, etc.). In addition, while simulations have begun to converge on accurate solutions for individual systems in a ΛCDM universe composed only of collisionless dark matter, star formation and feedback must still be treated using heuristic sub-grid approaches calibrated with empirical data, blurring the line between theory and observation and complicating the interpretation of simulations.

The second class involves semi-analytical galaxy formation models (e.g. Taylor & Babul, 2004; Zentner et al., 2005; Gan et al., 2010; Jiang & van den Bosch, 2014b; Pullen et al., 2014) which have a long history in cosmology, and have begun to be successfully applied to the local universe. The standard approach is to generate a mass accretion history using the excursion set formalism (e.g., Bond et al., 1991; Lacey & Cole, 1993) followed by an integration of individual accreting orbits from the moment of infall to the present day. Orbital parameters at infall are drawn from probability distributions motivated by numerical simulations (e.g., Navarro et al., 1995; Tormen, 1997; Ghigna et al., 1998; Benson, 2005; Zentner et al., 2005; Wang et al., 2005; Khochfar & Burkert, 2006; Jiang et al., 2008; Wetzel, 2011; Jiang et al., 2015) and the time integration contains prescriptions for various nonlinear processes such as tidal stripping, tidal heating, and dynamical friction. The utility of this approach is its computational speed, allowing one to simulate multiple realizations and cover a broad region of model and

parameter space compared to what can be achieved using expensive cosmological simulations. The drawback is that any simplifying assumptions (e.g., symmetries in the host potential, omission of substructure interaction) inherent to the model may affect the final result in an unknown or unphysical manner.

In this paper, we present a detailed case study of an individual object simulated at high resolution – the Via Lactea II (Diemand et al., 2008, VL2) simulation – with the aim of making connections relevant to semi-analytic models of substructure evolution. We focus on a self-consistent description of the most important physical processes and relationships, rather than on direct comparison to specific observations. Our goal is to separate the robust quantitative predictions of this simulation from those that are unique to the particular background cosmology and random realization used to generate its initial conditions.

This paper is organized as follows. In Section 3.3 we describe our methodology of extracting substructure evolution from the public VL2 catalogues. In Section 3.4 we present the main results of our work. We begin in §3.4.1 with a basic description of the host halo and in §3.4.2 statistics of its subhalo population, followed in §3.4.3 with a presentation of orbital properties at the time of infall, and in §3.4.4 with a quantitative assessment of substructure evolution including the physical processes of tidal mass loss and its dependence on subhalo properties, the orbital timescale, changes in the orientation of the orbital plane, and the dynamical readjustment of the internal structure of subhalos as portrayed by their movement in the $r_{\max} - v_{\max}$ plane. In §3.5 we compare the surviving and disrupted subhalo populations of VL2 and investigate how survivability depends on infall redshift, mass, concentration, and orbital parameters. We summarize our conclusions in Section 3.6.

3.3   Data Analysis

The VL2 simulation traced the growth of a galactic host halo within a high-resolution region sampled with roughly one billion particles of mass 4100 $M_\odot$. In what follows we make use of the main halo catalogue made publicly available[1] by the VL2 team. This catalogue contains evolutionary tracks of all 20048 (sub)halos within the simulation box that are resolved at $z = 0$ and for which their peak circular velocity was larger than $v_{\max} = 4$ km s^{-1} at some time during their evolution. The latter restriction is imposed to discard small halos affected by insufficient resolution.

The catalogue contains a collection of halo properties at 27 discrete redshifts between $0 \leq z \leq 27$. These properties include: the x, y, and z positions and velocities relative to the host halo rest frame; the tidal radius, r_{tid}, and tidal mass, m_{tid}; the maximum of the circular velocity curve, $v_{\max}$, and the radius, $r_{\max}$, at which this occurs. Empty values occur at redshifts when the halo progenitor either did not exist or overlapped with a more massive halo. In what follows we consider only the redshift range $0 \leq z \leq 4.56$ for which the host progenitor was consistently

---

[1]`http://www.ucolick.org/~diemand/vl/data.html`

identified within the simulation. This contains 19 redshift snapshots which we further refine by performing cubic spline interpolations of the above quantities to generate a total of 181 discrete sample points equally spaced by 68.8 Myr.

Subhalos are identified in VL2 using the six-dimensional phase-space friends-of-friends (6DFOF) algorithm described in Diemand et al. (2006). Around each (sub)halo the circular velocity profile, $v_{\rm circ} = \sqrt{Gm(<r)/r}$, is computed in spherical bins and is fitted with the sum of contributions from an NFW profile and a constant density background, $\rho_{\rm bg}$. The latter component is then subtracted from the (sub)halo density profile and a tidal radius is computed by solving $\rho_{\rm sub}(r_{\rm tid}) = 2\rho_{\rm bg}$, corresponding to the tidal radius of an isothermal sphere on a circular orbit within an isothermal host (Diemand et al., 2007a). The tidal mass is assigned $m_{\rm tid} = m(<r_{\rm tid})$. For sufficiently isolated halos, where the background density is small and $r_{\rm tid} > r_{200}$ (the radius at which the enclosed density is 200 times the mean *matter* density), $r_{\rm tid}$ is capped at r_{200} and $m_{\rm tid} = m_{200}$ (Diemand, private communication).

Hence, the subhalo masses used in this paper are not the result of an unbinding procedure of dark matter particles. Nevertheless, it was shown in the Via Lactea I (VL1) analysis (Diemand et al., 2007b) that this definition of tidal mass indeed agrees well with the true bound mass when the subhalo is near apocenter, but may significantly underestimate bound mass near pericenter. For this reason we generally only report mass quantities near apocenter and explicitly point out to the reader when this is not the case.

In the following subsections we define concepts and present our methodology of investigating substructure evolution from the VL2 data. We begin in §3.3.1 with the definition of a subhalo. In §3.3.2 we model the internal structure of the host and its subhalos via concentration parameters. We define in §3.3.3 the redshift, $z_{\rm infall}$, at which a subhalo is said to first infall onto the host. In §3.3.4 we outline our calculations of orbital energy and angular momentum and finish in §3.3.5 with a description of our method of tracing subhalo orbits after infall.

As a matter of convenience, we remove explicit redshift dependence in our following notation and remind the reader here that all quantities are computed at discrete times. We use lower case notation (e.g., m, $r_{\rm max}$, $v_{\rm max}$) when referring to subhalos while upper case notation (e.g., M, $R_{\rm max}$, $V_{\rm max}$) is reserved for the host. The mass of a subhalo is taken to be its tidal mass while the mass of the host is taken to be its virial mass (see §3.3.2). We often use $\mu \equiv m(z)/M(z)$ to denote the instantaneous mass ratio between a subhalo and the host. At times we normalize to the present-day host mass in which case we define $\mu_0 \equiv m(z)/M(0)$. In what follows we assume the same cosmology as the VL2 simulation; namely, the ΛCDM parameters $(\Omega_m, \Omega_\Lambda, h, n_s, \sigma_8)$ = (0.238, 0.762, 0.73, 0.951, 0.74) from the WMAP 3-year data release (Spergel et al., 2007).

3.3.1 Definition of a subhalo

We flag an object in the VL2 catalogue as a subhalo if at one time during its evolution it passed within the instantaneous virial radius of the host. This definition includes subhalos that are presently *within* the virial radius as well as subhalos that currently reside *outside* the virial

radius. We refer to the latter group as *ejected* subhalos in the sense that they are now removed from the virial boundary of the host. This terminology, however, does not imply that these subhalos are unbound from the host, as shown in §3.4.3.

In later sections we explore subhalo tidal mass loss. It was shown in Kazantzidis et al. (2004) that subhalos with too few particles within their tidal radius experience artificially large tidal mass loss. For this reason we impose a further restriction on the VL2 catalogue that only objects with at least 100 particles in their tidal radius at $z = 0$ may be considered as subhalos. This sets a minimum mass resolution of $m = 4 \times 10^5 \ M_\odot$.

We find a total of 7569 objects meeting the above criteria. 5845 (77%) of these currently reside within the host virial radius of $R_{\rm vir} = 320$ kpc (see §3.3.2) while the remaining 1724 (23%) are currently ejected. For the remainder of the paper we exclude those subhalos whose infall (see §3.3.3) is determined to be $z_{\rm infall} > 4.56$. This reduces the total population to 6145 subhalos with 4607 (75%) currently within the virial radius and 1538 (25%) ejected.

3.3.2   Host and subhalo mass distributions

It was shown in Navarro et al. (1997) that dark matter halos obey a universal density profile, named an NFW profile after its founders. This has the form $\rho(r) \propto x^{-1}(1 + x)^{-2}$, where $x \equiv r/r_s$ and r_s is the radius at which $d \ln \rho / d \ln r = -2$. The virial radius, $r_{\rm vir}$, is defined such that the enclosed density is $\Delta(z)$ times the critical density, where $\Delta(z)$ is calculated using the fitting function to the overdensity of a virialized uniform sphere in a flat universe given in Bryan & Norman (1998). An NFW profile is often parameterized by its concentration, $c_{\rm vir} \equiv r_{\rm vir}/r_s$, which describes the degree to which the mass is contained within the central region.

We assume that the density profile of the host follows an NFW form. We determine its concentration by finding the unique NFW profile for which the mass enclosed within $R_{\rm max}$ is $R_{\rm max} V_{\rm max}^2/G$. This involves the implicit solution of

$$g(C_{\rm vir}) = g(x_m)\frac{\Delta(z)}{2}\left[\frac{H(z)R_{\rm max}}{V_{\rm max}}\right]^2, \qquad (3.1)$$

where $g(x) \equiv f(x)/x^3$ with $f(x) \equiv \ln(1 + x) - x/(1 + x)$, $H(z)$ is the Hubble parameter, and $x_m \equiv R_{\rm max}/r_s \approx 2.163$. Once the concentration is obtained, the host halo mass is computed as $M_{\rm vir} = 4\pi\rho_{\rm crit}\Delta R_{\rm vir}^3/3$ where $R_{\rm vir} = C_{\rm vir}R_{\rm max}/x_m$.

The assumption of an NFW profile for the host should be valid over the entire redshift range considered here. For subhalos, however, an NFW profile is only valid up until its moment of infall onto the host. It was shown by Hayashi et al. (2003) that the processes of tidal heating and stripping tend to modify the internal structure of subhalos away from their initial form. For this reason, we only use $c_{\rm vir}$ obtained from equation (3.1) for subhalos at their time of infall.

Afterwards, we define a concentration parameter

$$c_{\mathrm{max}} = 2 \left[\frac{v_{\mathrm{max}}}{H_0 r_{\mathrm{max}}} \right]^2, \qquad (3.2)$$

which gives the mean density within r_{max} in units of the critical density. Comparing to equation (3.1) shows that, for any given redshift, there exists a monotonic relationship between c_{vir} and c_{max}.

3.3.3 Definition of infall

In an idealized description, a subhalo will form distinct from its future host, accreting surrounding material and growing steadily in size. This process will occur until the time at which tidal interactions with its host become important. At this point, the combined action of dynamical friction and tidal stripping will cause the subhalo to lose mass over time. We therefore define infall as this turnaround phase in the growth history of the subhalo. That is, we define the redshift, z_{infall}, of infall onto the host to be the moment in time at which the mass of the subhalo is a maximum[2].

Recall that masses in VL2 are assigned as the mass contained within the tidal radius. The tidal radius is derived, at any moment, by equating the subhalo density profile to twice the local background density. For sufficiently isolated subhalos, where the background density is small, the tidal radius is capped at r_{200}. The resultant tidal mass provides a good estimation of the true bound mass when the subhalo is near apocentre, which is generally the case at infall. As mentioned earlier, we consider only the 6145 subhalos for which $z_{\mathrm{infall}} \leq 4.56$ since at earlier times the host progenitor is only sporadically identified within the VL2 catalogues, preventing us from computing orbital properties at those times.

An alternative convention that is commonly used in the literature is to define infall as the moment the subhalo passes through the virial radius of the host. However, as shown previously (Hahn et al., 2009; Behroozi et al., 2014), subhalos generally undergo strong tidal forces at distances larger than R_{vir}. Furthermore, the virial radius evolves with redshift through its dependence on $\Delta(z)$, meaning that its value will change even if the intrinsic mass profile of the host is unchanging. The virial radius is therefore not well-suited for defining the distance at which a subhalo becomes tidally truncated by the host, and can be said to undergo infall in the sense considered here.

---

[2]This definition does not filter out the possibility that a subhalo may initially lose mass via tidal interactions with a halo other than its future host. Such group preprocessing was studied in Wetzel et al. (2015) where it was found that a significant fraction of subhalos reside within the virial radius of a different halo prior to passing through the virial radius of the main host. We therefore note the possibility that our z_{infall} are biased toward larger values, though it is unclear to what magnitude group preprocessing affects premature mass loss.

3.3.4 Orbital energy and angular momentum

We determine the energy and angular momentum by assuming that subhalos evolve as isolated point particles within the spherically symmetric NFW profile of the host. In this case, the host potential is

$$\Phi(r) = -\frac{R_{\max}V_{\max}^2}{f(x_m)}\frac{\ln(1+x_m r/R_{\max})}{r}, \tag{3.3}$$

where $r = |\mathbf{r}|$ is the radial separation between the subhalo and host. In this expression we have taken the zero point of the potential to be at infinity. The specific orbital energy of the subhalo is

$$E = \frac{1}{2}\mathbf{v}\cdot\mathbf{v} + \Phi(r), \tag{3.4}$$

while its specific orbital angular momentum is

$$L = \mathbf{r}\times\mathbf{v}. \tag{3.5}$$

Here $\mathbf{v}$ is the physical relative velocity between the subhalo and host which includes the sum of peculiar motion and Hubble flow.

In general, the continued action of dynamical friction will steadily drain energy and angular momentum from subhalo orbits. The evolution of a subhalo after infall thus depends strongly on its initial energy and angular momentum. It is therefore important to characterize the infall distributions of E and L as inputs in semi-analytic models of subhalo evolution. A common convention is to normalize these quantities in terms of a circular orbit of the same energy. We introduce two variables: (i) $\eta \equiv r_{\mathrm{circ}}/R_{\mathrm{vir}}$, defined to be the ratio of the radius, r_{circ}, of a circular orbit of the same energy E as the subhalo to the virial radius, R_{vir}, of the host at infall; (ii) the circularity, $\epsilon \equiv L/L_{\mathrm{circ}}$, defined to be the ratio of the subhalo angular momentum, L, to the angular momentum, L_{circ}, of a circular orbit of the same energy. To compute η and ϵ we must first evaluate r_{circ}, which is achieved by numerically solving the expression

$$\frac{\ln(1+y)}{y} + \frac{1}{1+y} = -\frac{2Ef(x_m)}{x_m V_{\max}^2}, \tag{3.6}$$

where $y \equiv x_m r_{\mathrm{circ}}/R_{\max}$. Then $L_{\mathrm{circ}} = \sqrt{GM(r_{\mathrm{circ}})r_{\mathrm{circ}}}$ where $M(r_{\mathrm{circ}})$ is the mass contained within radius r_{circ} of the host.

The definitions of η and ϵ used here are self-consistent with the description of a subhalo orbiting within an isolated NFW profile. This does not, however, conform with the standard method applied in semi-analytic models of substructure evolution. Instead, it is common to report these quantities at the time when the subhalo first crosses through R_{vir} and to model the host potential as a point mass of M_{vir}. In this case, the orbital energy is

$$E = \frac{1}{2}\mathbf{v}\cdot\mathbf{v} - \frac{GM_{\mathrm{vir}}}{R_{\mathrm{vir}}}, \tag{3.7}$$

and the radius of a circular orbit of the same energy is

$$r_{\text{circ}} = -\frac{GM_{\text{vir}}}{2E}.$$ (3.8)

When discussing η and ϵ at infall we report the results of both methods so that we can make direct comparisons to previous work.

3.3.5 Definition of an orbit

In §3.4.4 we compute subhalo quantities, such as tidal mass, taken over the course of an orbital period. To do so requires a precise definition of an "orbit". This is a complicated task since an orbit within a spherical potential is not closed, generally, and traces a rosette pattern, oscillating radially between a minimum pericenter, r_{peri}, and maximum apocenter, r_{apo} (see, e.g., Binney & Tremaine, 1987). Furthermore, the mass distribution in realistic halos departs significantly from spherical symmetry, due both to triaxiality in the smooth component, as well as substructure. Finally, subhalos slowly spiral inward due to dynamical friction both from the background matter distribution as well as stripped material. Consequently, energy and angular momentum are not in general conserved, and we require a robust and physical definition of an orbit that does not depend on simplifying assumptions such as spherical symmetry and conserved quantities.

We choose to work solely from knowledge of the radial position of the subhalo as a function of time, determining the local minima (pericenters) and maxima (apocenters). Due to the somewhat coarse time information, apocenters are generally more accurately determined than pericenters, since halos spend a larger fraction of time further away from the host center. Thus, we define an orbit as that segment of the subhalo trajectory between two successive apocenters. A given orbit is therefore characterized by the time at first and last apocenters t_1 and t_2, the two apocenters $r_{\text{apo},1}$ and $r_{\text{apo},2}$, and the pericenter, r_{peri}. We take the mean of the two apocenters, $\bar{r}_{\text{apo}} \equiv (r_{\text{apo},1} + r_{\text{apo},2})/2$, and define an effective eccentricity

$$e_{\text{eff}} \equiv \frac{\bar{r}_{\text{apo}} - r_{\text{peri}}}{\bar{r}_{\text{apo}} + r_{\text{peri}}},$$ (3.9)

while the period of the orbit is $t_{\text{orb}} = t_2 - t_1$.

3.4 Results

3.4.1 Host halo

We begin by presenting the derived properties of the host halo using the method outlined in §3.3.2. Figure 3.1 shows the redshift evolution of the host virial mass and concentration. Open circles denote the redshifts for which the VL2 catalogues are sampled while the solid black lines trace the result we derive after performing a cubic spline interpolation on the time evolution of
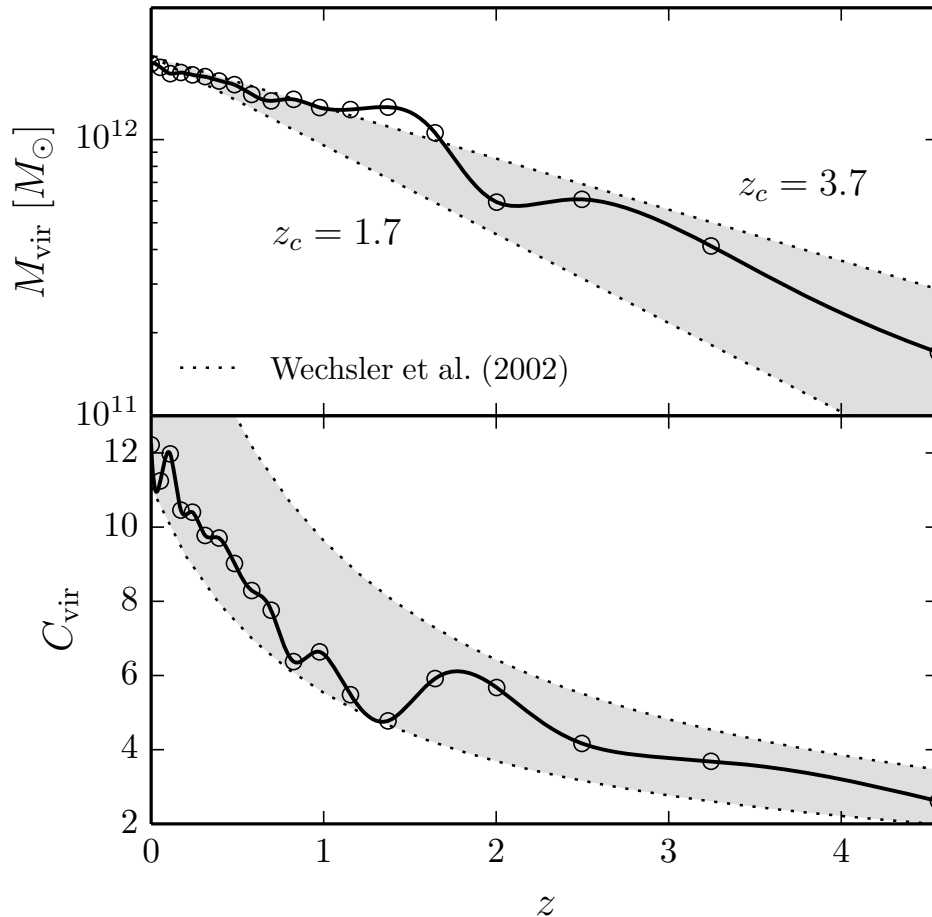
Figure 3.1: Evolution of the viral mass (top panel) and concentration (bottom panel) of the host halo obtained by finding the unique NFW profile that matches the values of R_{max} and V_{max} at each redshift. Open circles denote redshifts at which the VL2 catalogues are sampled while solid black lines trace the results derived from a cubic spline interpolation of R_{max} and V_{max}. The dotted black lines in each panel show the expected evolution for the fitting functions given by Wechsler et al. (2002) for collapse times $z_c = 1.7$ and $z_c = 3.7$ (see text). The VL2 curves are well contained within the shaded region, which may reflect an initial "collapse" at $z \sim 3.7$ (in the sense of the Wechsler et al. formalism) followed by an episode of significant mass accretion at $z \sim 1.7$ which "resets" the concentration back to the virialization value of $C_{\mathrm{vir}} \sim 4$.

R_{max} and V_{max}. Our method finds the host to evolve from a virial mass of $M_{\mathrm{vir}} = 1.7 \times 10^{11}\ M_\odot$ at $z = 4.56$ to $M_{\mathrm{vir}} = 1.9 \times 10^{12}\ M_\odot$ at $z = 0$. The concentration evolves from $C_{\mathrm{vir}} = 2.6$ at early times to $C_{\mathrm{vir}} = 12.2$ at the present day.

Wechsler et al. (2002) showed that halo concentration is strongly related to mass assembly history. In particular, evolution in concentration and virial mass can be described remarkably well using a single parameter, $a_c = 1/(1 + z_c)$, defined as the formation or collapse time of the halo. They provide fitting relations $C_{\mathrm{vir}} = 4.1 a/a_c$ and $M_{\mathrm{vir}}(z) = M_{\mathrm{vir}}(0)\exp[-2a_c z]$ which we

plot in Figure 3.1 spanning the redshift range $z_c = 1.7 - 3.7$. The VL2 data fits well within the shaded region which may reflect an initial collapse time of $z \sim 3.7$ followed later by an episode of significant mass assembly at $z \sim 1.7$ which resets the concentration back down to $C_{\mathrm{vir}} \sim 4$.

3.4.2   Mass functions

The subhalo mass function provides a statistical measure of the amount of substructure within a host as a function of mass scale. In general, we can speak of two subhalo mass functions: the *unevovled* and *evolved* mass functions. The unevolved mass function counts the number of subhalos based on their mass at the time of infall. The choice of name emphasizes that this is a measure of the distribution of subhalos before they have had time to evolve under the influence of tidal processes within the host. The evolved mass function, on the other hand, counts the number of subhalos based on their present-day masses.

In the middle panels of Figure 3.2 we plot both the unevolved and evolved subhalo mass functions measured from VL2. We compare these to the corresponding mass functions from Boylan-Kolchin et al. (2010, BK10) which were fitted from the Millennium II (Boylan-Kolchin et al., 2009) and Aquarius (Springel et al., 2008) simulations. This is a useful comparison since BK10 considered host halos with similar masses to the VL2 host halo and use the same definition of z_{infall} as we do here. One difference, however, is that BK10 do not consider subhalos that reside outside the virial radius of the host at $z = 0$ (i.e., ejected subhalos; see §3.3.1). For more of a direct comparison, we also plot the VL2 mass functions with ejected subhalos removed. The bottom panels show more closely the comparison between VL2 and BK10.

The VL2 and BK10 unevolved mass functions agree well with each other over most of the mass range seen here. The sharp cutoff at small mass simply reflects the resolution limit of VL2. There is considerable disagreement at the high mass end, though this regime is inherently noisy due to small number statistics. This can be seen in the top left panel where the cumulative distribution in μ_0 at infall is shown; only 11 objects with $\mu_0 > 4 \times 10^{-3}$ at infall exist. Including ejected subhalos enhances the VL2 unevolved mass function by a constant factor indicating that infall mass does not play a significant role in determining whether a subhalo resides outside of R_{vir} at $z = 0$.

Note that the unevolved mass functions shown here correspond only to those subhalos that accrete onto the host and remain intact at $z = 0$. The red line in Figure 3.2 traces equation (21) of Jiang & van den Bosch (2014a) which shows the unevolved mass function for *all* subhalos ever accreted onto the host. This mass function is found to have a universal form (van den Bosch et al., 2005; Giocoli et al., 2008; Li & Mo, 2009), independent of host halo mass and cosmology, except perhaps a small dependence on n_s (Yang et al., 2011). The main difference between this mass function and that of surviving subhalos occurs at high μ where dynamical friction selectively disrupts massive subhalos after infall. The VL2 unevolved mass function (black triangles) agrees well with the red line albeit with a small systematic shift upwards. In §3.5 we analyze disrupted subhalos in VL2 and find that including them here would further
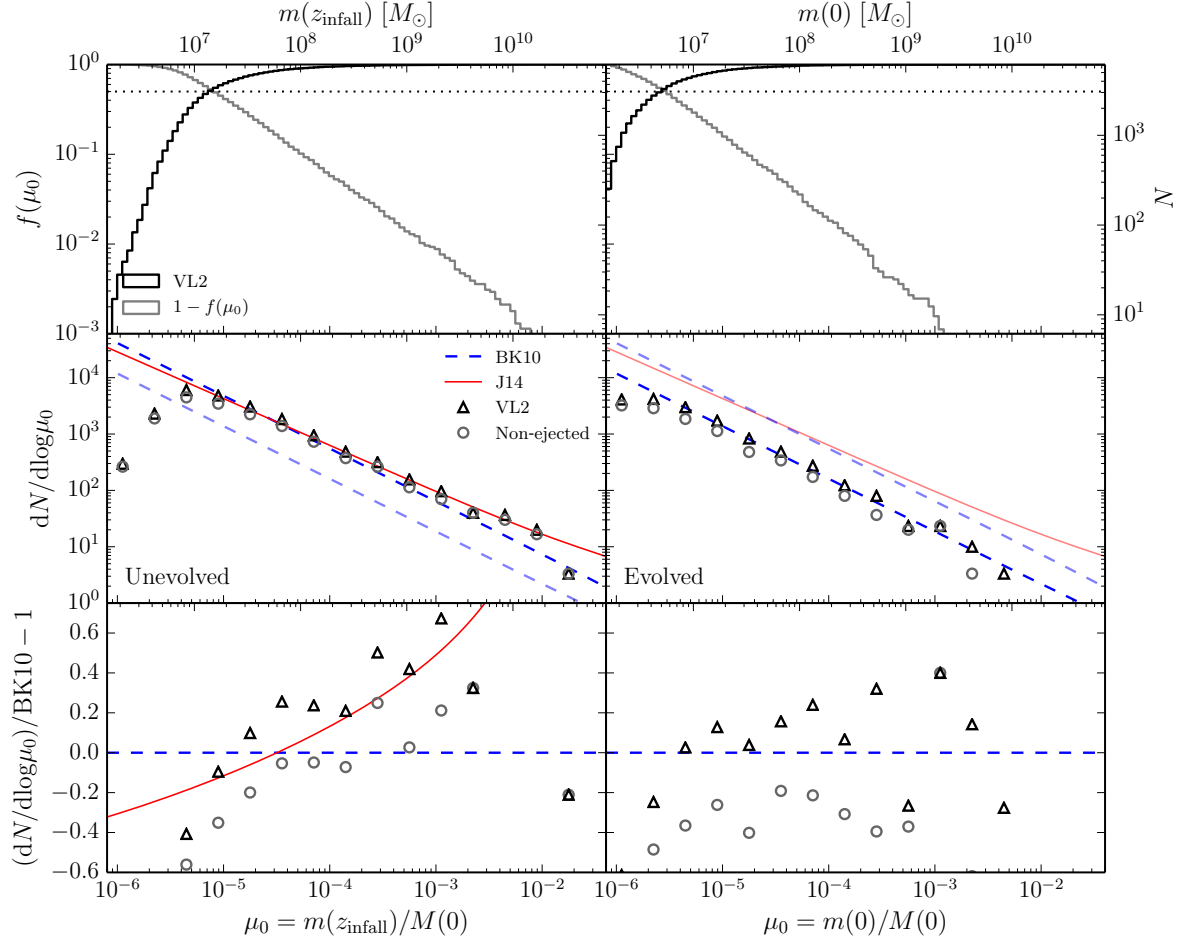
Figure 3.2: Top panels show the cumulative distribution in μ_0 measured at infall (left) and at $z = 0$ (right) for all 6145 VL2 subhalos. The gray histogram shows the reverse cumulative distribution function. Middle panels show the corresponding unevolved (left) and evolved (right) mass functions for all subhalos (black triangles) and only "non-ejected" subhalos (gray circles). Hence, the gray circles correspond to only those 4607 subhalos currently residing within $R_{\rm vir}$ at $z = 0$ (see §3.3.1). This is done for the purpose of comparing to the Aquarius simulation, shown as the dark dashed blue line, based on the BK10 fitting function. The VL2 and Aquarius mass functions show only those subhalos that survive to the present epoch. In contrast, the solid red line traces the fitting function of Jiang & van den Bosch (2014a) for the unevolved mass function of *all* subhalos accreting onto the host. The lightly shaded curves in the left (right) panel correspond to evolved (unevolved) quantities in order to better show the difference between the two mass functions. The bottom left (right) panel shows the relative difference between the various data and the unevolved (evolved) BK10 fitting function.

boost the black triangles upward by $\sim 5\%$ in the range $10^{-5} \lesssim \mu_0 \lesssim 10^{-3}$ (see Figure 3.16). We are indeed focusing on the low-mass regime where dynamical friction and tidal disruption are relatively unimportant for the vast majority of subhalos.

The right panels of Figure 3.2 show the evolved counterparts. The evolved mass function can be thought of as a shift to lower mass due to tidal stripping. This can be seen by comparing

the dark and lightly shaded blue lines. The VL2 evolved mass function lies systematically below the BK10 result at a level of about 30%. BK10 quote an intrinsic halo-to-halo scatter of 18% for $\mu_0 \lesssim 10^{-3}$ which is not enough to explain the discrepancy seen here. Instead, the difference observed here is most likely related to differences in cosmological parameters. In particular, VL2 uses $\sigma_8 = 0.74$ while Aquarius simulates larger perturbations with $\sigma_8 = 0.9$. It is not straightforward to describe how this difference manifests in the evolved mass function since there are at least two competing effects. On the one hand, the lower amplitude of fluctuations in VL2 will yield later formation times meaning that subhalos have less time on average to lose mass since infall. On the other hand, later formation times also yield lower subhalo concentrations which promote more efficient mass loss (see §3.4.4).

Another factor that may contribute to this difference lies in the definition of tidal mass used by VL2. As described in §3.3, subhalo masses in VL2 are underestimated at pericenter due to the simplified scheme used in computing mass based on local density comparisons. This is in contrast to the unbinding procedure used by Aquarius with the code SUBFIND (Springel et al., 2001). As a result, the VL2 evolved mass function will be biased toward smaller masses as some subhalos will be found near pericenter at $z = 0$ (the unevolved mass function is less affected since subhalos are generally near apocenter at infall). Nevertheless, we only expect this to be a partial effect since a suppression of 30% was also seen in Klypin et al. (2011) when comparing VL2 and Aquarius v_{max} functions. The physical mechanism leading to the systematic difference between the VL2 and Aquarius evolved mass functions remains to be seen.

3.4.3 Subhalo properties at infall

In this section we focus on subhalo statistics at the time of infall onto the host. In particular, we investigate the redshift at which infall occurs (§3.4.3), the radial distance from the host at which tidal truncation initiates (§3.4.3), and show distributions in orbital energy (§3.4.3) and angular momentum (§3.4.3) at infall. The results presented here are important as inputs into semi-analytic models of substructure evolution and extend the results of previous works to much lower mass.

Redshift: z_{infall}

In Figure 3.3 we show the cumulative distribution of infall redshift for all 6145 subhalos with $z_{\mathrm{infall}} \leq 4.56$. We see that half of the population has fallen into the host by $z = 2$. We also plot separate distributions for the 1σ outliers having the smallest 16% present-day mass ($\mu \leq 5 \times 10^{-7}$) and largest 16% present-day mass ($\mu \geq 7 \times 10^{-6}$). We see that presently more massive subhalos tend to have fallen in at more recent times. There are two reasons for this trend: (i) structure forms hierarchically, so halos falling in at earlier times were on average less massive to begin with than those infalling later; (ii) subhalos of a given mass that fell in earlier have had more time to undergo tidal stripping, and will be less massive today.
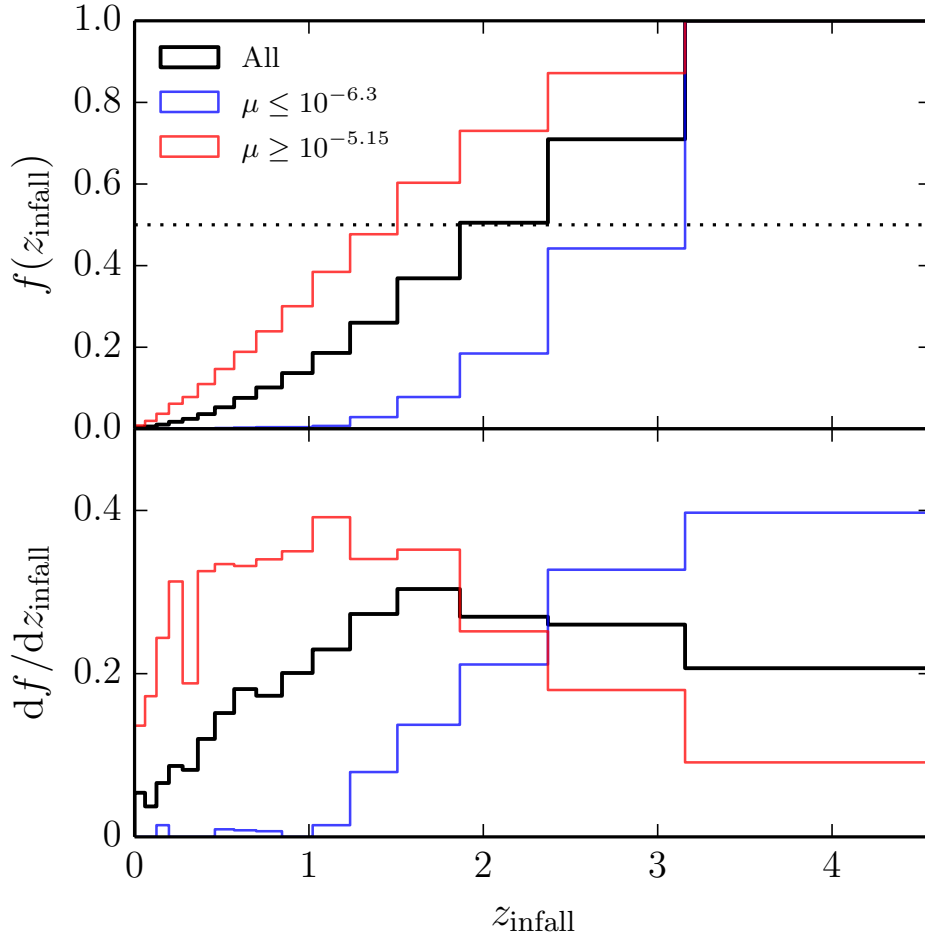
Figure 3.3: Cumulative (top panel) and differential (bottom panel) infall redshift distributions for bins equally spaced in cosmic time. The black histogram traces the total sample of subhalos while the blue and red histograms show distributions for the 1σ outliers with the smallest and largest present-day mass ratios, respectively.

Radius: r_{infall}

Figure 3.4 shows the distribution of the radial distance, r_{infall}, between the subhalo and host at infall normalized to the virial radius of the host at that time. Hence, we are plotting the relative distance at which the subhalo has its growth history truncated due to tidal interactions with the host. We also plot separate distributions for the 1σ outliers with the most recent infall, $z_{\mathrm{infall}} \leq 1.1$, and earliest infall, $z_{\mathrm{infall}} \geq 3.93$. In each case, the differential distribution can be well approximated by a lognormal form in $r_{\mathrm{infall}}/R_{\mathrm{vir}}$. The mean and standard deviation of the least-squared lognormal distribution for each population are summarized in Table 3.1.

Somewhat surprisingly, we find that over 90 per cent of subhalos undergo tidal growth truncation outside of the virial radius, with roughly 50 per cent infalling at a distance of more than three virial radii from the host. Considering halos falling in at the earliest times, $z_{\mathrm{infall}} > 3.93$, this fraction rises above 80 per cent. We emphasize, however, that these numbers
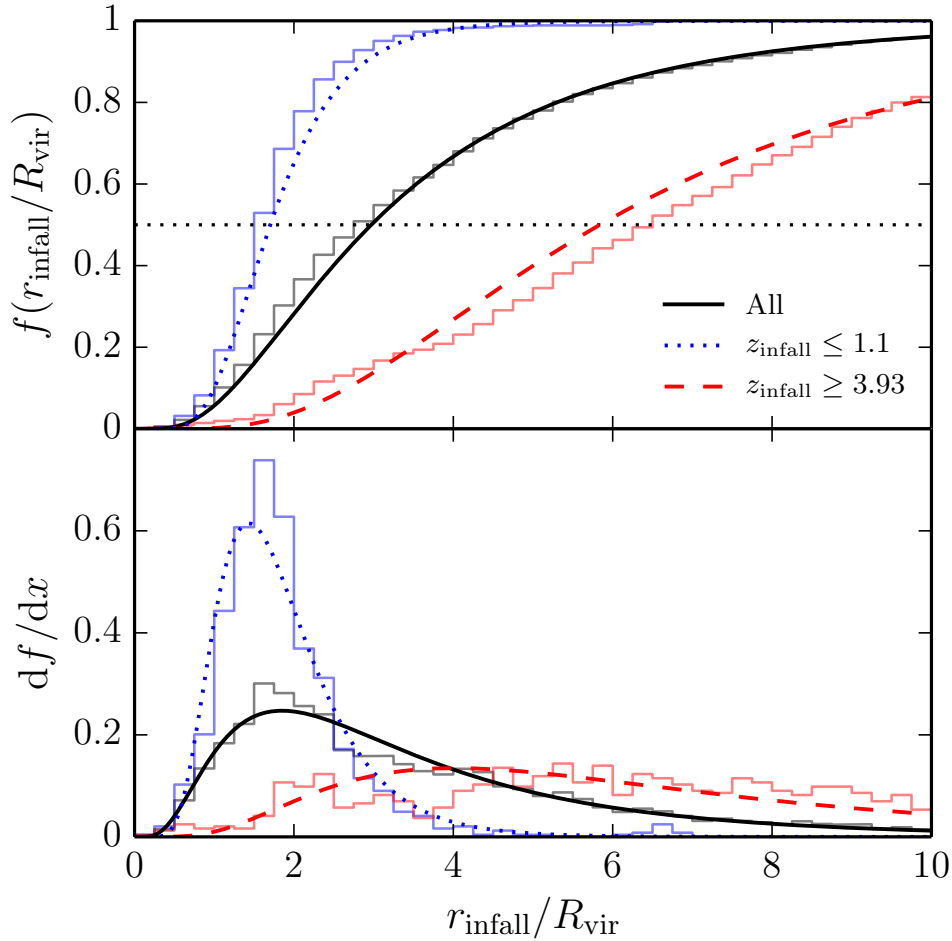
Figure 3.4: Cumulative (top panel) and differential (bottom panel) distributions in the ratio of the radial distance at infall, r_{infall}, to the virial radius of the host, R_{vir}, at that time. The black histogram traces the total sample of subhalos while the blue and red histograms show distributions for the 1σ outliers with the smallest and largest infall redshifts, respectively. The solid black curve, dotted blue curve, and dashed red curve trace lognormal fits to the black, blue, and red histograms, respectively. The mean and standard deviation of these fits are given in Table 3.1.

are likely biased toward larger values since our definition of infall does not exclude the possibility of group preprocessing for which tidal truncation first occurs via interactions with halos other than the future host. Nevertheless, our findings are in qualitative agreement with past studies (Hahn et al., 2009; Behroozi et al., 2014) showing that tidal truncation generally occurs outside of R_{vir}. This trend is also apparent in the top panel of Figure 3.5, where we show the relationship between infall radius and redshift directly. *Why do halos at high redshift begin to be affected so far outside the host?*

A first hint is provided upon inspection of the bottom panel of Figure 3.5, where the infall concentration is plotted against infall redshift. We see a strong correlation, with halos that fall in earlier having much lower concentrations. This is expected because the typical mass of an
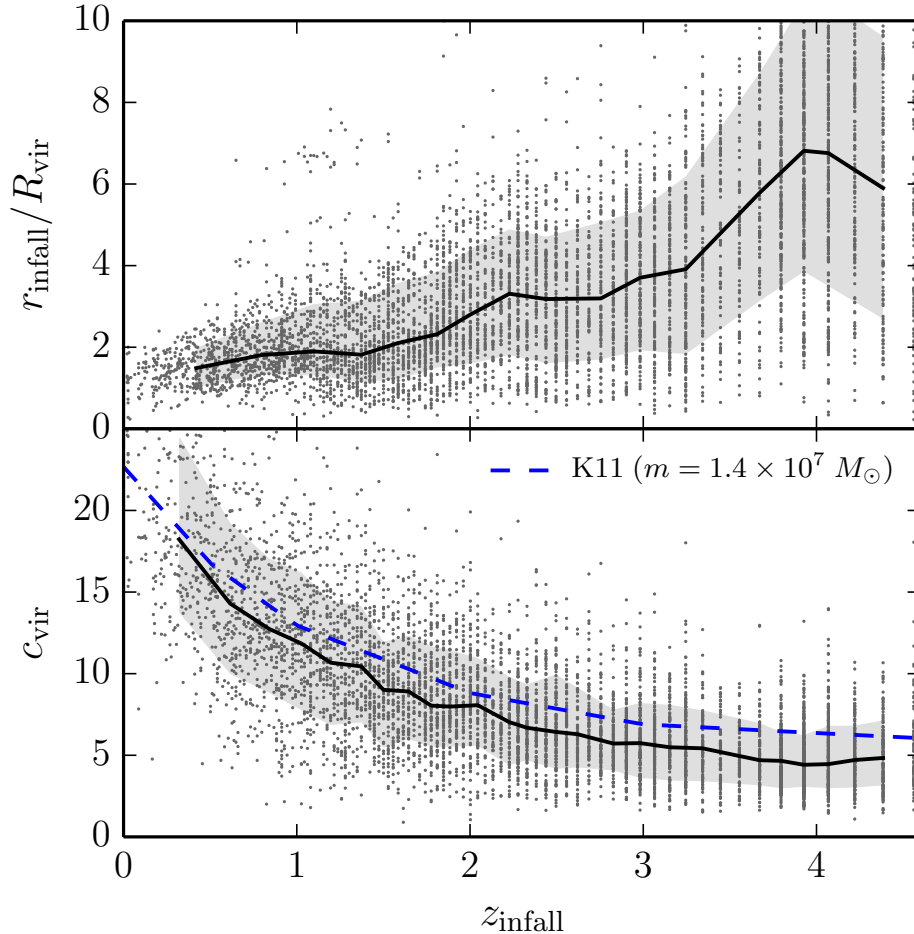
Figure 3.5: Top panel shows the radius–redshift relationship at infall, for each subhalo (points), with median (solid line) and 1σ distribution (shaded region) in each z_{infall} bin. Bottom panel shows the concentration–redshift relationship at infall. Solid line and and shaded region have the same meanings as in the top panel. Shown also is the mean concentration–redshift relationship from Klypin et al. (2011) for a subhalo mass of $1.4 \times 10^7 M_\odot$, which we find to be the median infall mass, independent of redshift. Halos falling in earlier are less concentrated *and* have their growth truncated at larger distances.

infalling halo does not change very strongly with redshift. Thus, the concentrations of infalling halos grow roughly as expected for halos of a fixed mass, e.g., $1.4 \times 10^7 M_\odot$, which we find to be the median infall mass, independent of z_{infall} (see also Figures 3.2 and 3.16). This is shown

Table 3.1: Lognormal $r_{\mathrm{infall}}/R_{\mathrm{vir}}$ Fits.

Population	μ	σ
All subhalos	1.09	0.69
$z_{\mathrm{infall}} \leq 1.1$	0.53	0.42
$z_{\mathrm{infall}} \geq 3.93$	1.76	0.61

as the blue dashed line, which is the mean concentration–redshift relationship at fixed mass as determined by Klypin et al. (2011)[3]. It would seem that a plausible explanation lies in the concentration of infalling halos.

This can be directly tested by plotting $r_{\rm infall}/R_{\rm vir}$ versus $c_{\rm vir}$, as shown in the top panel of Figure 3.6. We see a definite trend of more concentrated subhalos coming closer to the host before undergoing infall. Our physical interpretation is that highly concentrated subhalos with compact density profiles are more resilient to tidal stripping. Hence, they are able to plunge deeper into the potential well of the host before appreciable mass loss occurs. Note that the relationship seen in Figure 3.6 appears weaker than the trend observed when comparing $c_{\rm vir}$ versus $z_{\rm infall}$ in Figure 3.5. In particular, there is a significant fraction of halos with $c_{\rm vir} < 10$ and $r_{\rm infall}/R_{\rm vir} < 3$, with the vast majority of these falling in at late times. This implies there are other effects at high redshift that hinder the growth of infalling halos, in addition to lower central densities.

Before advancing we note that a trend in $r_{\rm infall}/R_{\rm vir}$ versus $c_{\rm vir}$ is expected to exist even if $r_{\rm infall}$ does not change much with time. This is based on the fact that both $c_{\rm vir}$ and $R_{\rm vir}$ generally increase with time due to the expansion of the universe. To try to account for this, we plot, in the bottom panel of Figure 3.6, $r_{\rm infall}/R_s$ versus $c_{\rm vir}/C_{\rm vir}$, where $R_s = R_{\rm vir}/C_{\rm vir}$ is the scale radius of the host. Normalizing $c_{\rm vir}$ and $r_{\rm infall}$ in this way acts to remove redshift dependencies in $c_{\rm vir}$ and $R_{\rm vir}$. We are thus plotting how close tidal truncation occurs relative to the central density peak of the host as a function of subhalo concentration relative to that of the host. Although weaker, we still see a definite trend of more concentrated subhalos coming closer to the central depth of the host before experiencing tidal truncation. This lends support to the notion of an intrinsic radius-concentration relation for infalling subhalos.

Orbital energy: $\eta_{\rm infall}$

Semi-analytic models of substructure evolution require two inputs as initial conditions for subhalo orbits: energy and angular momentum. In this section we present the infall distribution of energy as seen in VL2 and proceed in the next section with angular momentum. In accordance with past studies, we parametrize the infall energy in terms of the variable $\eta \equiv r_{\rm circ}/R_{\rm vir}$, where $r_{\rm circ}$ is the radius of the circular orbit of the same energy as the subhalo and $R_{\rm vir}$ is the virial radius of the host at infall. We compute this quantitiy by first evaluating equation (3.4) for the orbital energy, and then solving equation (3.6) for $r_{\rm circ}$ based on an orbit within an isolated NFW host potential.

This parametrization is only valid for subhalos on bound orbits ($E < 0$). It turns out that this condition is not very restrictive since only 38 (0.6%) of the 6145 subhalos are on unbound

---

[3]Note that the concentration-redshift relation observed here is systematically lower than the Klypin et al. (2011) curve. One reason is that the latter was calibrated against the Bolshoi simulation which had an enhanced amplitude of perturbations with $\sigma_8 = 0.82$ compared to the value of 0.74 employed by VL2. At a fixed redshift we expect VL2 concentrations to be lower than in the Bolshoi simulation based on the notion that concentration reflects the background density of the Universe at the time of halo formation.
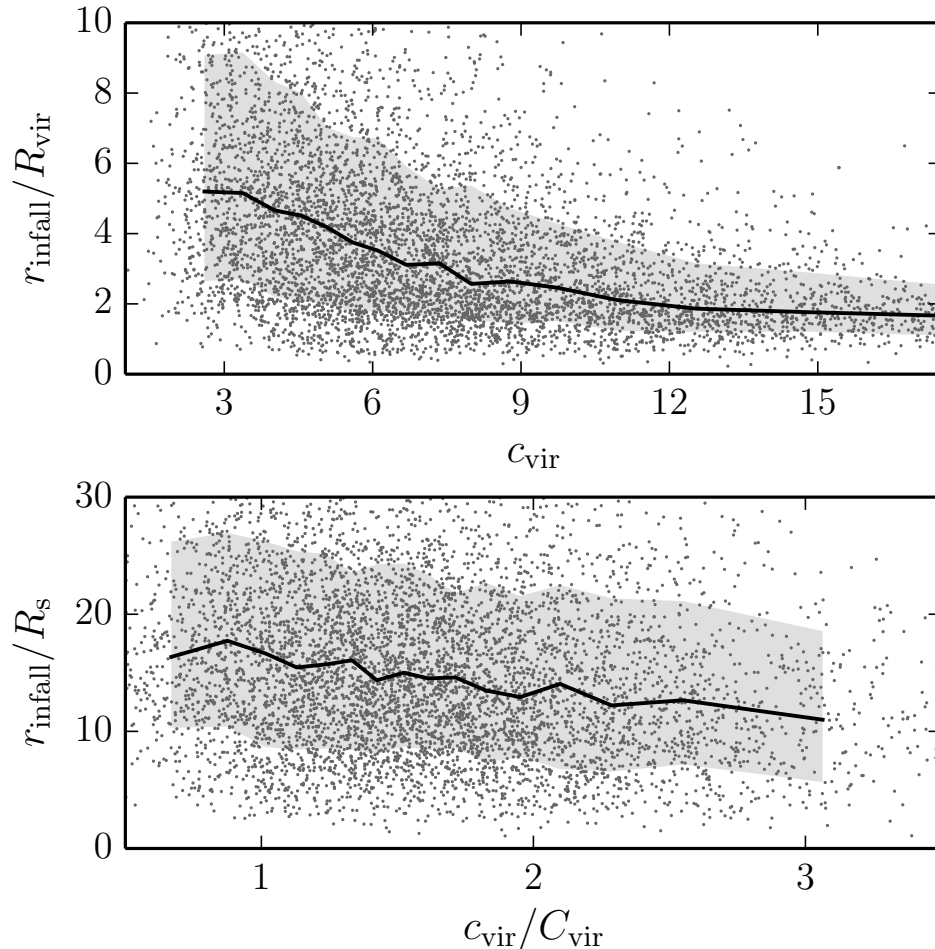
Figure 3.6: Top panel shows the infall radius–concentration relationship at infall. The bottom panel shows a similar result with c_{vir} and r_{infall} normalized to the concentration and scale radius of the host, respectively. In both panels the solid line and shaded region have the same meaning as in Figure 3.5.

orbits at the time of infall. This number is still small at $z = 0$ when only 75 subhalos are found to be on unbound orbits. Interestingly, *all* 75 of these subhalos are outside of R_{vir} at $z = 0$ (i.e., they are ejected subhalos) meaning that *no* subhalos within the present virial radius are unbound. In contrast, only a small fraction (7/38) of unbound subhalos at infall end up being part of the ejected population of subhalos at $z = 0$. Moreover, *none* of the unbound subhalos at infall are also unbound at $z = 0$. Being unbound from the host potential at infall correlates neither with being presently unbound nor with being found outside R_{vir} at $z = 0$. Instead, it is likely that presently unbound subhalos acquire orbital energy from gravitation interactions after infall. This can be achieved, for example, through three-body interactions between merging groups of subhalos as they make their first passage together around the host (Sales et al., 2007; Ludlow et al., 2009).

In Figure 3.7 we plot the VL2 distribution in η at infall for all bound subhalos. This is
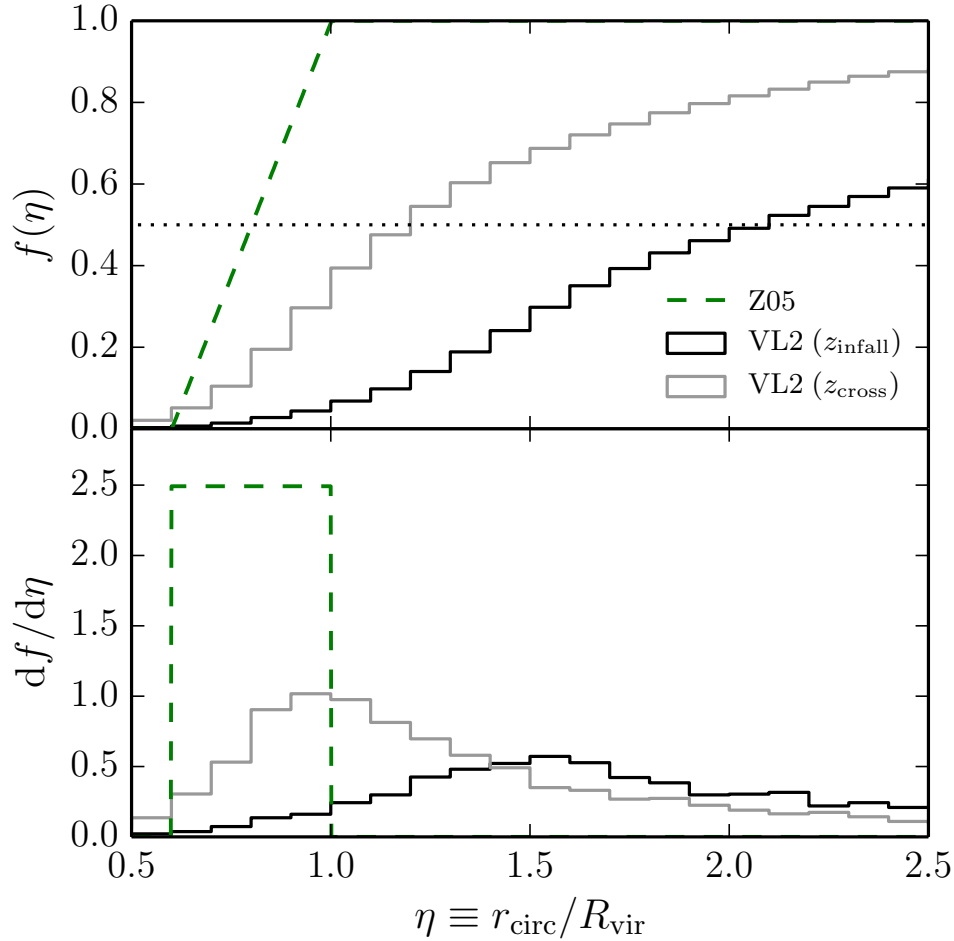
Figure 3.7: Cumulative (top panel) and differential (bottom panel) VL2 distributions in η at the time of infall (black histogram) and first virial crossing with a point mass potential (gray histogram). Compared to the latter is the green dashed curve showing the uniform distribution reported by Z05.

compared to the uniform distribution between $[0.6, 1]$ used in the semi-analytic model of Zentner et al. (2005, Z05) based on the analysis of the N-body simulations of Klypin et al. (2001) and Kravtsov et al. (2004). This also serves as the basis for the input distributions of η used in the semi-analytic models of Gan et al. (2010) and Jiang & van den Bosch (2014b). The VL2 result, with a peak at $\eta \sim 1.5$, is in clear disagreement with the Z05 distribution. However, as described in §3.3.4, our calculation of η is not directly comparable to that of Z05. Firstly, Z05 report η at the time a subhalo first crosses through $R_{\rm vir}$, which occurs at much later times on average than $z_{\rm infall}$ (see §3.4.3). In addition, orbital energy and $r_{\rm circ}$ are computed via equations (3.7) and (3.8), valid for a point mass host potential. The gray histogram in Figure 3.7 shows the result of applying this method to the VL2 data. The agreement with Z05 is better, but still heavily offset toward larger values of η.

In the recent work of Jiang et al. (2015, J15) it was shown that η depends on mass ratio

Table 3.2: Lognormal $\mathrm{d}f/\mathrm{d}\eta$ Fits.

| | z_{infall} with NFW host | | z_{cross} with point host | |
Population	μ	σ	μ	σ
All subhalos	0.70	0.50	0.18	0.40
$z \leq 1$	0.38	0.21	0.29	0.41
$1 \leq z \leq 2$	0.53	0.36	0.22	0.38
$2 \leq z \leq 3$	0.88	0.44	0.17	0.39
$z \geq 3$	1.50	0.54	0.10	0.40

at infall, with smaller objects tending toward larger η. A direct comparison with their result is difficult, however, due to their choice of a singular isothermal sphere host potential. Nonetheless, their analysis suggests that looking only at subhalos with $\mu_0 \gtrsim 10^{-3}$, similar to those resolved in Z05, would shift the gray histogram in Figure 3.7 to the left, presumably in better agreement with the uniform distribution. Since VL2 samples only one host halo, however, we cannot test this explicitly due to insufficient statistics in high-mass subhalos. Nevertheless, the result found here corroborates the work of J15 and indicates that the infall distribution assumed for η in various semi-analytic models of substructure evolution may only be strictly valid for relatively massive subhalos. Low-mass subhalos ($\mu_0 \lesssim 10^{-3}$) tend to have more kinetic energy, making them less bound to the host, with lower specific binding energy.

We plot in Figure 3.8 the dependence of η on mass for the range of mass captured in VL2. In this low-mass regime, there does not appear to be any significant trend of η with infall mass. Instead, we find a strong trend with infall redshift. This trend is attributed to the fact that R_{vir} is an increasing function of time so that η is pushed to larger values at earlier times. This trend is slightly suppressed by a competing evolution in r_{circ} with redshift: we find typical values of r_{circ} increase by a factor of ~ 2 from $z = 4$ to $z = 0$ (whereas R_{vir} increases by ~ 8 in this range). This intrinsic evolution in r_{circ} with z_{infall} indicates that subhalos falling in at earlier times do so on slightly more bound (smaller r_{circ}) orbits. The top right panel of Figure 3.8 shows a strong trend in η with c_{vir} which can be attributed to the concentration-redshift relation seen earlier in Figure 3.5.

We note that the trends observed in the top panels of Figure 3.8 depend on which version of η we present. Namely, we find that using η computed at virial crossing for a point mass host potential mostly washes out the dependence of η with redshift and concentration. The reason is that subhalos tend to become more bound in time after infall so that η is pushed to smaller values at the time of virial crossing, z_{cross}, which generally occurs after z_{infall} (see Figure 3.5). This seems to occur in such a way as to mostly cancel the evolution in R_{vir} with z. The difference between the black and gray histograms in Figure 3.7 can therefore be mostly explained by two effects: (1) larger R_{vir} at z_{cross} and (2) smaller r_{circ} at z_{cross}.

We find that the probability distributions, $\mathrm{d}f/\mathrm{d}\eta$, can be well modelled by lognormal distributions. In Table 3.2 we list the best-fit mean and standard deviations for both the total

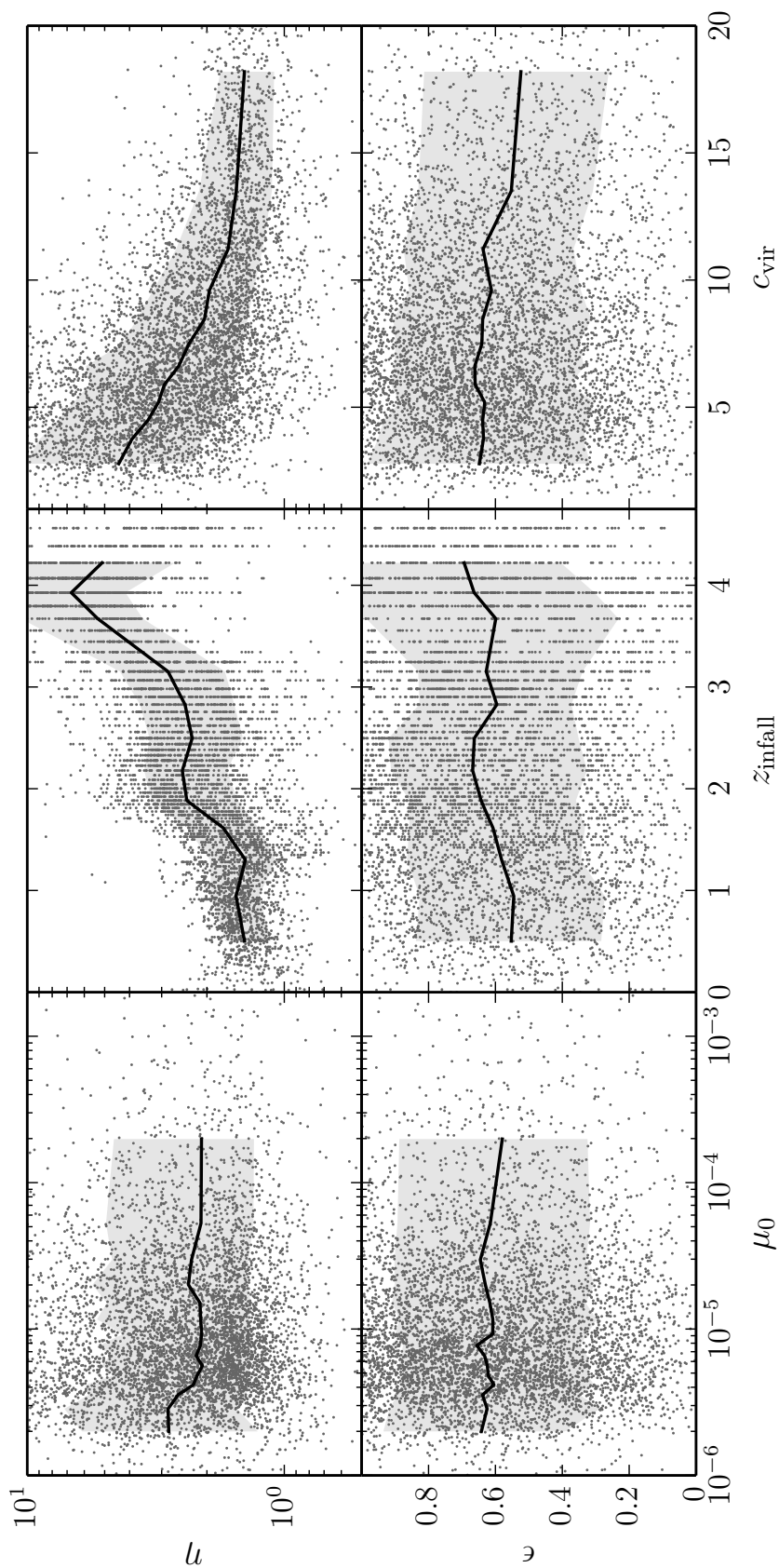Figure 3.8: The dependence of η (top panels) and ϵ (bottom panels) at infall on mass ratio at infall (left), infall redshift (middle), and concentration at infall (right). In both cases we assume an NFW potential for the host. Points denote individual subhalos while the solid line shows the median trend for bins along the x-axis with the corresponding 1σ spread indicated by the shaded region.

distribution as well as those obtained from different redshift ranges. The latter corresponds to cuts in $z_{\rm infall}$ and $z_{\rm cross}$ for the infall and virial crossing methods, respectively. These fitting functions are appropriate for subhalos with mass ratio $\mu_0 \lesssim 10^{-3}$. Higher mass subhalos should shift closer to the Z05 curve in Figure 3.7. In §3.5 we find that subhalos on tightly bound orbits with $\eta < 1$ are preferentially disrupted after infall. However, this has only a small impact on the distributions presented here since this bias is small and there are far fewer disrupted than surviving subhalos. Hence, the fitting functions provided here should be applicable to the total ensemble of subhalos (surviving plus disrupted) that ever accreted onto the host.

Orbital angular momentum: $\epsilon_{\rm infall}$

Studies of substructure evolution (e.g., Peñarrubia et al., 2008) show that subhalos on more radial orbits with lower specific angular momentum plunge deeper into their hosts and experience accelerated mass loss over subhalos on more circular orbits with higher specific angular momentum (see also §3.4.4). Accurately modelling subhalo evolution therefore requires a good handle on the distribution of angular momentum at the time of infall. As such, a great deal of work has been done on measuring this distribution from N-body simulations (Navarro et al., 1995; Tormen, 1997; Ghigna et al., 1998; Benson, 2005; Zentner et al., 2005; Wang et al., 2005; Khochfar & Burkert, 2006; Jiang et al., 2008; Wetzel, 2011). The conclusions of these works agree well with each other: the circularity distribution of infalling satellites is peaked at $\bar{\epsilon} \approx 0.5$ and falls off on either side so that neither largely radial ($\epsilon \sim 0$) nor largely circular ($\epsilon \sim 1$) orbits occur. Below we turn our attention to the circularity distribution measured in VL2.

In Figure 3.9 we plot the infall distribution in ϵ for all bound subhalos. As in Figure 3.7, we show the result at $z_{\rm infall}$ for an isolated NFW host potential (black histogram) as well as the result at first $R_{\rm vir}$ crossing for a point mass host potential. The latter can be compared to the various curves showing the infall distributions used in semi-analytic models of substructure evolution. First, the blue dotted line is the Gaussian distribution used by Taylor & Babul (2004) with mean $\bar{\epsilon} = 0.4$ and standard deviation $\sigma = 0.28$ which was selected so that the final distribution at $z = 0$ matches the results of Tormen (1997) and Ghigna et al. (1998). Second, the green dashed line shows the one-parameter β distribution used in the models of Z05 and Jiang & van den Bosch (2014b). Finally, the red dot-dashed curve shows the infall distribution assumed in the semi-analytic model of Gan et al. (2010), which was taken from the analysis of the hydrodynamic simulations of Jiang et al. (2008).

The gray histogram, with median $\epsilon = 0.55$, is in reasonable agreement with the various curves used in semi-analytic models. There is, however, a clear excess in nearly circular orbits with $\epsilon \sim 1$. The reason for this is the same as was discussed in the previous section. It was shown in J15 that circularity is highly dependent on mass, with high mass subhalos tending to move along radial orbits while low mass subhalos tend to have more circular orbits. One possible explanation is related to the environment in which these objects form. High mass halos are more biased towards forming in high density regions such as filaments and are consequently
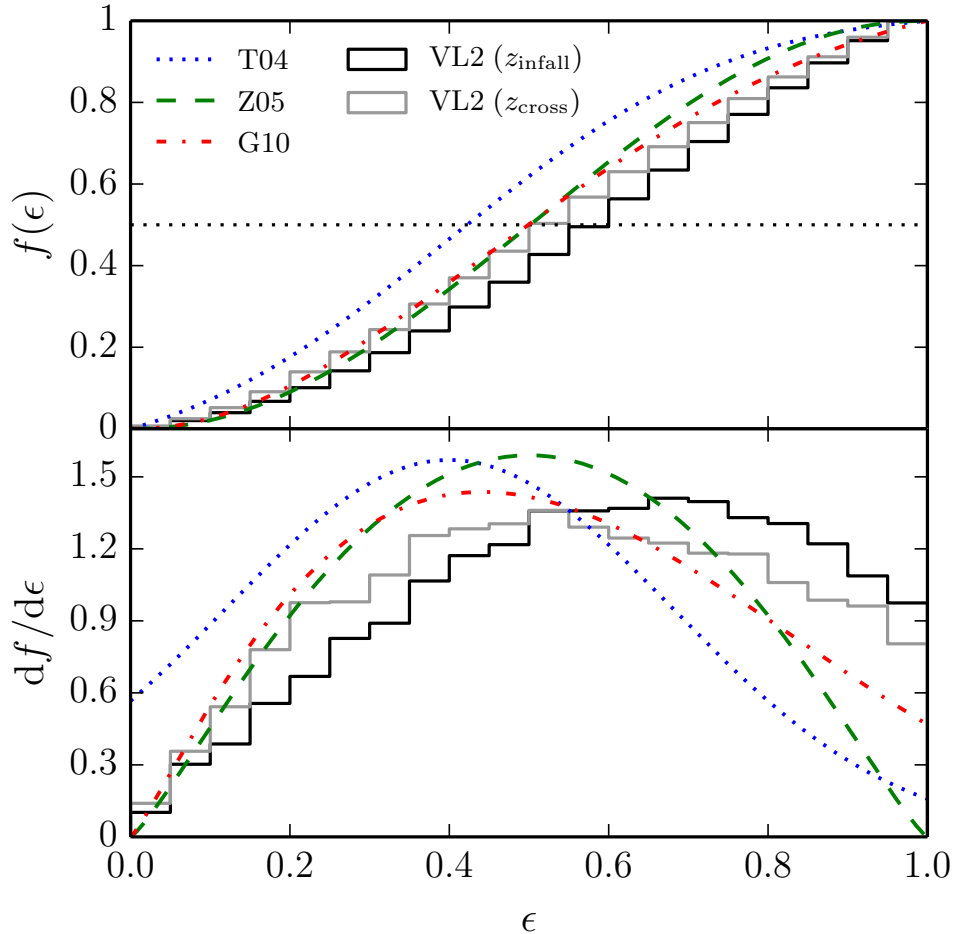
Figure 3.9: Cumulative (top panel) and differential (bottom panel) distributions in ϵ at the time of infall (black histogram) and first virial crossing with a point mass potential (gray histogram). Compared to the latter are various curves showing the circularity distributions employed in semi-analytic models of substructure evolution: the blue dotted curve is the distribution from Taylor & Babul (2004); the green dashed curve is the distribution given by Z05; the red dot-dashed curve is the distribution from Gan et al. (2010).

more likely to fall radially into their host with lower specific angular momentum. Low mass subhalos are less biased to forming within filaments and are thus more likely to fall into their host with a larger component of tangential motion. Another possible explanation, independent of the first, is that low-mass subhalos are simply more likely to acquire tangential motion from gravitational interactions with nearby massive objects prior to infall.

In the bottom panels of Figure 3.8 we show the dependence of ϵ on mass, redshift, and concentration. As with η, we find that ϵ does not exhibit strong mass dependence in the range $\mu_0 \lesssim 10^{-3}$ probed by VL2. There also does not appear to be much dependence on z_{infall}, consistent with the earlier work of Wetzel (2011). There is correspondingly little dependence on ϵ with infall concentration. Replacing the lower panels of Figure 3.8 with ϵ computed at virial crossing for a point mass host potential produces the same (lack of) trends.

Even though the two methods produce similar trends in Figure 3.8, it remains difficult to qualitatively describe the differences between the black and gray histograms in Figure 3.9. The reason is the dependence of L_{circ} on the form of the host potential assumed. In fact, we find that ϵ, unlike η, is very sensitive to the form of the host potential. For example, computing ϵ at infall with a point mass host potential pushes the black histogram in Figure 3.9 to even larger values. Counterintuitively, computing ϵ at virial crossing with an NFW host potential also pushes the gray histogram to larger values, being almost on top of the black histogram. We therefore note that one should be careful in choosing a fitting function for ϵ that suits their specific needs.

We fit the circularity distributions in Figure 3.9 with the following form:

$$\frac{\mathrm{d}f}{\mathrm{d}\epsilon} = a\epsilon^{\alpha}(b - \epsilon)^{\beta}. \tag{3.10}$$

We find the best-fit coefficients $(a, b, \alpha, \beta) = (3.696, 1.12, 1.07, 0.68)$ at infall with an NFW host potential and $(a, b, \alpha, \beta) = (1.508, 1.77, 1.05, 2.45)$ at virial crossing with a point mass host potential. These fitting functions are appropriate for subhalos with mass ratio $\mu_0 \lesssim 10^{-3}$ and are independent of redshift. Higher mass subhalos should have distributions in closer agreement with the other fitting functions plotted in Figure 3.9. In §3.5 we show that circularity does not influence the survivability of low-mass subhalos. The fitting functions provided here are thus applicable to the total ensemble of subhalos (surviving plus disrupted) that ever accreted onto the host.

3.4.4   Evolution

In this section we focus on the evolution of subhalo properties over the course of infall to the present day. This includes internal subhalo properties such as tidal mass and central density as well as orbital properties including radial period and angular momentum. Our results are used to test some of the fundamental assumptions underlying models of substructure evolution.

A common assumption in modeling tidal mass stripping is that subhalos of a given mass lose a certain fraction of their mass in one dynamical time. For example, van den Bosch et al. (2005) developed a model in which the mass loss rate of a given subhalo is $\dot{m} \propto m^{1+\zeta}/\tau_{\mathrm{dyn}}(z)$ where $\tau_{\mathrm{dyn}}(z) \propto (\Delta\rho_{\mathrm{crit}}(z))^{-1/2}$ is proportional to the free fall time of a halo, independent of mass. Recently, Jiang & van den Bosch (2014b) used numerical simulations to fit the mass dependence, finding $\zeta = 0.07$. This is very close to the case $\zeta = 0$, in which the fractional mass loss rate is independent of mass.

Modeling dynamical friction and sinking due to the resultant loss of angular momentum plays a prominent role in modeling subhalo orbital evolution. The trajectory of subhalos through the host must be modelled accurately. Assumptions typically involve spherical symmetry, wherein the torque of dynamical friction is in the direction of the subhalo orbital angular momentum, and subhalos orbit in the same plane.

The question naturally arises whether common assumptions such as those discussed above hold for the low-mass subhalos considered here. In the following sections, we examine separately the mass lost per orbit per halo mass, the orbital period per host dynamical time, and the alignment of tidal torques and angular momentum.

Tidal mass loss: $\Delta m/m$

The general picture of mass loss is related to the processes of dynamical friction and tidal stripping, as follows. The continued force of dynamical friction causes an infalling subhalo to slowly descend into its host. As the orbital radius shrinks, so too does the tidal radius, causing the subhalo to continually shed mass from the outside-in. The internal structure of the subhalo is also affected, generally puffing outwards due to the injection of tidal heat, promoting additional mass loss. Mass loss will vary over the course of an orbital period, being strongest (weakest) at pericenter (apocenter) when tidal interactions with the host are greatest (smallest). Tidal mass loss is clearly a complicated process that will depend on both the internal structure of a subhalo as well as its orbital parameters.

We begin our investigation of mass loss in Figure 3.10 where we plot distributions in $\Delta m/m_{\mathrm{infall}}$. Here, the mass change is $\Delta m = m_{\mathrm{apo,1}} - m_{\mathrm{apo,2}}$ where $m_{\mathrm{apo,1}}$ and $m_{\mathrm{apo,2}}$ are the mass at the start and end of the orbit, respectively. The black histogram shows mass loss over the course of the first orbit after infall while the blue histogram shows mass loss over the last orbit before $z = 0$. Recall that we define an orbit to correspond to the time between successive apocenter passages so the "first" orbit does not start exactly at infall and the "last" orbit does not end exactly at $z = 0$. More specifically, the first orbit begins at the first apocenter after infall[4] while the last orbit terminates at the last apocenter before the present time. We find that 3966 (65%) subhalos finish at least one orbit after infall while 2714 (44%) finish at least two. Since we are interested in comparing how mass loss changes with time, we plot only those 2714 subhalos for which the first and last orbit is different.

Comparing the two distributions in Figure 3.10 shows that subhalos tend to lose a larger fraction of their initial mass during their first orbit compared to their last orbit. In particular, the median mass loss in the first orbit is 16% of the initial mass while the median mass loss in the last orbit is about an order of magnitude smaller, at 3% of the initial mass. Note that not all subhalos lose mass over the course of an orbital period. In particular, for both the first and last orbit, roughly 5% of subhalos actually *gain* mass. This likely occurs either through direct merger with smaller systems or, more gradually, through the accretion of surrounding material.

We proceed to investigate the dependence of mass loss on subhalo properties. The top row of Figure 3.11 shows mass loss versus mass ratio at the start of the orbit. For both orbits, more massive subhalos tend to lose more mass on average. Normally, we would expect this

---

[4]We find that infall is roughly symmetric about the turnaround point where the subhalo first detaches from the Hubble flow and begins its descent towards the host. In particular, 52% of subhalos start to lose mass before turnaround while 48% begin losing mass after turnaround. Hence, for roughly half of the cases, the first orbit begins at the turnaround radius, corresponding to the first apocentre.
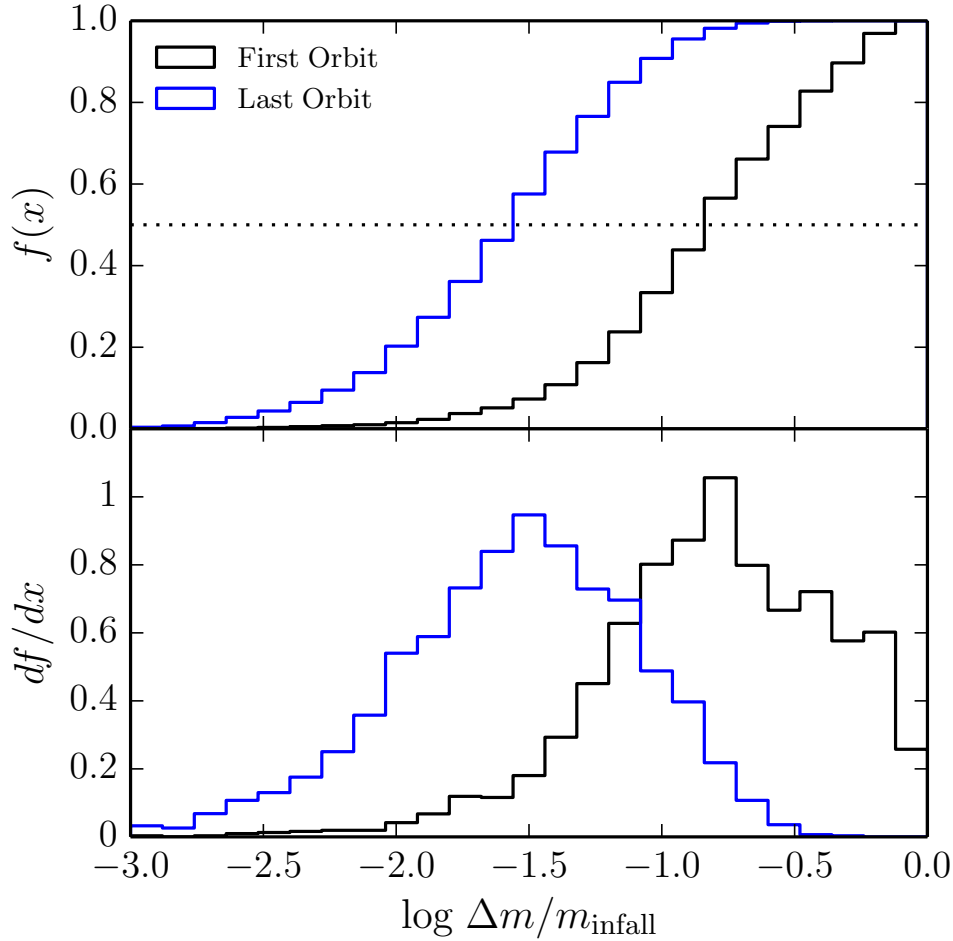
Figure 3.10: Cumulative (top panel) and differential (bottom panel) distributions in the mass loss over the course of an orbit normalized to the mass at infall. The black histogram pertains to the first orbit after infall while the blue histogram shows the last orbit before $z = 0$. Only those 2714 subhalos (44% of the total population) that complete at least two orbits after infall are shown.

result on the basis of a dynamical friction argument whereby the oribts of massive subhalos are preferentially dragged into the depths of the host, promoting enhanced mass loss. However, we do not expect this argument to apply here since the dynamical friction merging timescale for $\mu \lesssim 10^{-3}$ subhalos is much longer than the Hubble time (Boylan-Kolchin et al., 2008).

Instead, the observed correlation with mass is the result of the mass-concentration relation which states that more massive subhalos will be less concentrated on average. We plot as blue circles (red triangles) the 2σ outliers with the smallest 2.3% (largest 2.3%) values of $c_{\mathrm{max}}/C_{\mathrm{max}}$ at the start of the orbit. From the definition of c_{max} in equation (3.2), the ratio $c_{\mathrm{max}}/C_{\mathrm{max}}$ describes the relative central density of the subhalo to the host. In both panels a clear dichotomy emerges with the least (most) concentrated, and most (least) massive, subhalos loosing (retaining) more mass per obit.

This is made more apparent in the middle row of Figure 3.11 where we see a strong negative
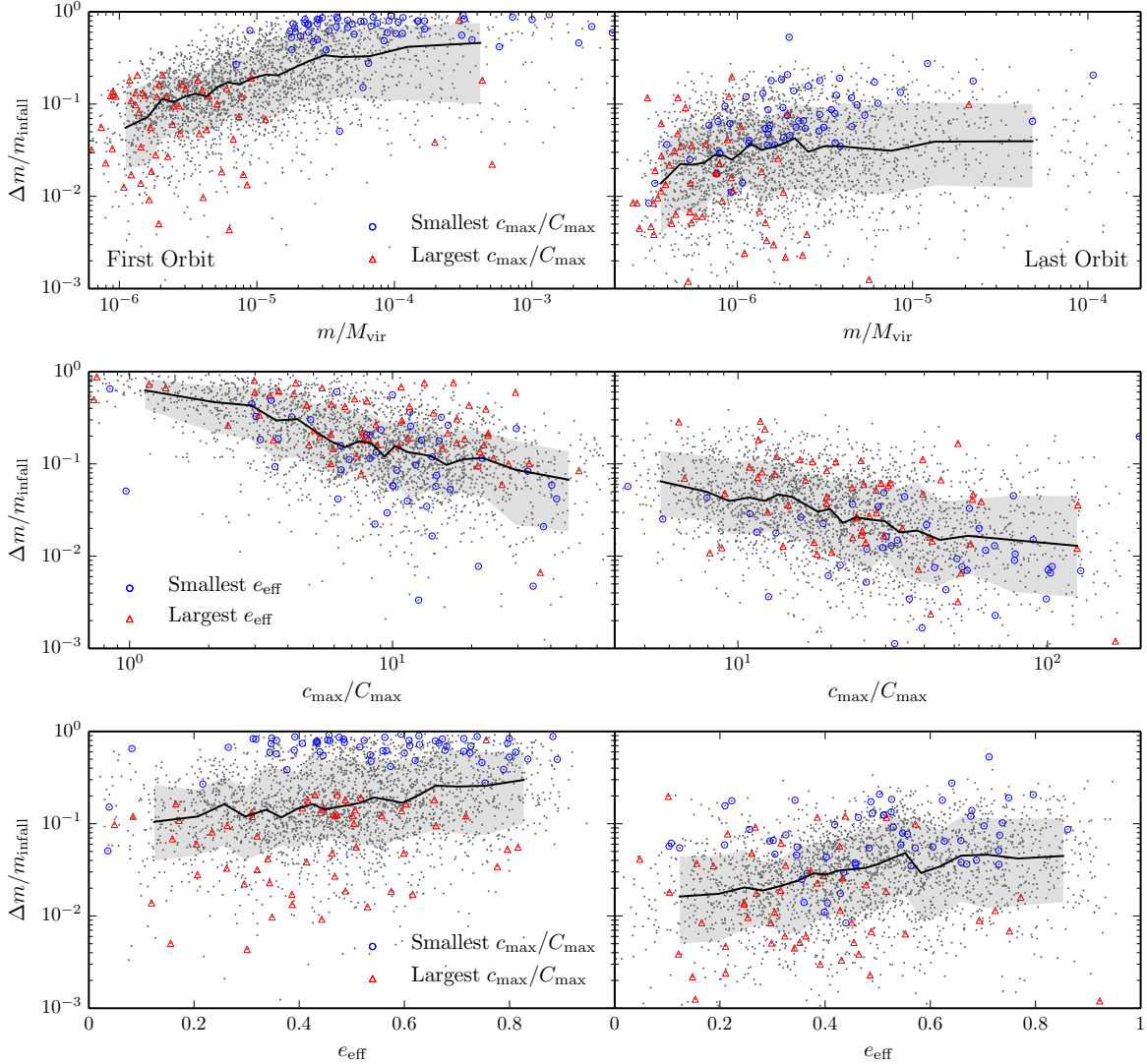
Figure 3.11: Left (right) panels show the fractional amount of mass, Δm, lost over the course of the first apocenter-to-apocenter orbit after infall (last apocenter-to-apocenter orbit before $z = 0$) normalized to the mass, m_{infall}, of the subhalo at the time of infall. The various rows show: (i) fractional mass lost as a function of m/M_{vir} with both quantities computed at the start of the orbit; (ii) fractional mass lost as a function of $c_{\mathrm{max}}/C_{\mathrm{max}}$ with both quantities computed at the start of the orbit; (iii) fractional mass lost as a function of eccentricity e_{eff} computed from equation (3.9). In each panel the solid black line traces the median mass loss for bins with equal number of samples in the x axis while the shaded region shows the 1σ spread about this line. In the top and bottom rows, blue circles and red triangles highlight the 2σ outliers with the smallest 2.3% and largest 2.3% values of $c_{\mathrm{max}}/C_{\mathrm{max}}$. In the middle row, blue circles highlight the 2σ outliers with the smallest eccentricities while red triangles highlight the 2σ outliers with the largest eccentricities.

slope in mass loss versus concentration. There is still considerable scatter at fixed concentration which can be partly attributed to eccentricity. Comparing blue circles and red triangles shows that for fixed concentration, more circular (radial) orbits tend to retain (lose) more mass on

average. A direct comparison is plotted in the bottom row of Figure 3.11 where we detect a small correlation between mass loss and eccentricity.

We have also checked for correlation between mass loss and pericenter, r_{peri}. One would expect that subhalos plunging further into the depths of the host, where tidal forces are strong, would experience enhanced mass loss. We instead find almost no correlation with r_{peri}[5]. The reason is that subhalos closer to the host center tend to be more concentrated (see §3.4.3) which washes out the dependence on r_{peri}.

We conclude that tidal mass loss in the regime of low-mass subhalos is most directly correlated with concentration. When concentration is held fixed, we find no trend in mass loss with varying mass. The apparent trend seen when comparing mass loss versus mass is simply a reflection of the fact that mass is correlated with concentration. This result makes physical sense in the limit of weak dynamical friction since it is the density of a subhalo, relative to its host, that determines how tightly a subhalo on a stable orbit retains its contents (e.g., Taffoni et al., 2003). At fixed concentration, subhalos on more eccentric (i.e., radial) orbits tend to lose more mass than subhalos on circular orbits. This may highlight the importance of tidal heating which results when a rapidly varying gravitational potential injects energy into subhalos, puffing them outwards and promoting further mass loss (e.g., Hayashi et al., 2003).

Orbital period

The dynamical time for a halo is usually defined as the free-fall time of a test particle in a static, uniform sphere at the virial density,

$$\tau_{\mathrm{dyn}}^2 \equiv [16 G \rho_{\mathrm{crit}} \Delta / (3\pi)]^{-1} = \frac{\pi^2 R_{\mathrm{vir}}^3}{4 G M_{\mathrm{vir}}}. \tag{3.11}$$

It is natural to expect, all else being equal, that timescales within the halo should scale in proportion to this dynamical time. For example, the time to complete an orbit is roughly proportional to the dynamical time. Similar scaling arguments apply for timescales other than orbital period, such as the tidal mass loss time, $m/\dot{m}$. Departures from a simple linear scaling with the dynamical time occur because orbital shapes vary from subhalo to subhalo. For example, halos on larger orbits should have longer orbital times, with a correlation between semi-major axis and period that reflects the mass distribution of the host halo around the virial radius.

In Figure 3.12 we show the orbital period of halos just after they fall in, defined as the time between the first two apocenters after infall. The orbital period is plotted in units of the

---

[5]Note that our calculation of r_{peri} is based upon a cubic spline interpolation of subhalo radial distance from discrete VL2 snapshots (see §3.3). The snapshots are separated by 0.688 Gyr which may lead to a potentially crude estimation of the true r_{peri}. Another way to estimate r_{peri} is to solve the roots in the equation of motion of a point particle of energy E and angular momentum L in a static NFW host potential (see, e.g., Binney & Tremaine, 1987). This may lead to a better determination of r_{peri} as E and L vary more smoothly with time than radial distance. Nevertheless, we have checked that using r_{peri} computed in this way changes neither the results on mass loss versus eccentricity nor mass loss versus pericentre.
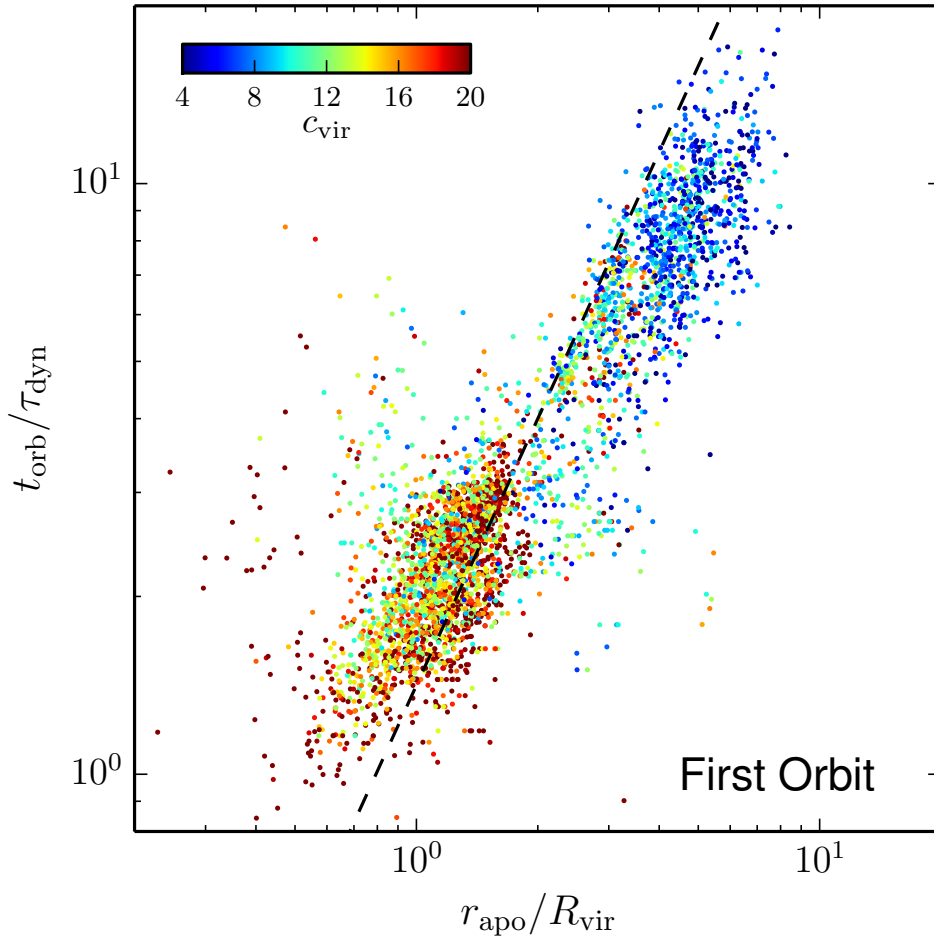
Figure 3.12: Orbital period, $t_{\rm orb}$, in units of the halo dynamical time, $\tau_{\rm dyn}$, for subhalos on their first orbit, colored by concentration, as a function of first apocenter, $r_{\rm apo}$, in units of the host virial radius. All quantities are determined at the beginning of the orbit. Shown as the dashed line is the relationship expected for radial orbits (eccentricity $e = 1$) orbiting a point with mass $M_{\rm vir}$.

dynamical time, $\tau_{\rm dyn}$, at the beginning of the orbit. On the x-axis we show $r_{\rm apo}/R_{\rm vir}$. The first striking trend is the large spread in $t_{\rm orb}/\tau_{\rm dyn}$ values. There is also a similarly large spread, about an order of magnitude, in the apocenters, $r_{\rm apo}/R_{\rm vir}$ of halos on their first orbit. In fact, there is a strong correlation between orbital period and apocentric distance, as expected. Interestingly, there are two "clouds" of subhalos. Those with high concentration at small radius, and those with low concentration at large radius.

Also shown is the relationship expected for radial orbits (where the semi-major axis $a = r_{\rm apo}/2$) around a point mass with $M = M_{\rm vir}$, $t_{\rm orb}^2 = 4\pi^2 a^3/(GM_{\rm vir}) = \pi^2 r_{\rm apo}^3/(2GM_{\rm vir})$. Combining with equation (3.11), we obtain

$$\frac{t_{\rm orb}}{\tau_{\rm dyn}} = 4 \left(\frac{r_{\rm apo}}{2R_{\rm vir}} \right)^{3/2} . \tag{3.12}$$

Subhalos would lie along this line only if they were on radial orbits and all the halo mass was located at the halo center. In general, departures from radial orbits ($a > r_{\mathrm{apo}}/2$) lead to longer orbital times, while the presence of matter outside the virial radius (i.e. the overdensity associated with continuous infall onto the host) leads to shorter orbital times. The latter effect could be responsible for the shorter times at $r_{\mathrm{apo}} > 2R_{\mathrm{vir}}$, although more information about the evolving density profile outside the virial radius would be required to make a quantitative comparison.

Orbital plane

A common assumption made in models of substructure evolution is spherical symmetry of the host. Subhalo orbits are generally integrated in either a static potential or one that dynamically adjusts (e.g., through mass accretion) in a spherically symmetric manner. In either case, the direction of the orbital angular momentum vector is conserved since it is aligned with the direction of the torque. Hence, an obvious test of spherical symmetry within VL2 is to look for changes in the orientation of the orbital plane.

In Figure 3.13 we plot the distribution in the dot product between the angular momentum normal vector at $z = 0$ and infall:

$$\chi = \hat{L}_0 \cdot \hat{L}_{\mathrm{infall}}. \tag{3.13}$$

The black histogram shows the distribution for all subhalos while the blue and red histograms show the 1σ outliers with the latest and earliest infall, respectively. The median χ for all subhalos is 0.39 while subhalos with the earliest and latest infall time have median values 0.16 and 0.88, respectively. There is a clear trend of recently infalling halos remaining in the same orbital plane while subhalos with early infall have their orientation randomly aligned.

Subhalo orbits are continuously torqued after infall, in a direction that is not aligned with the angular momentum vector. Subhalos spending more time in the host experience larger changes in $\hat{L}$. 98% of subhalos with $z_{\mathrm{infall}} < 1.1$ do not finish an orbital period by $z = 0$ while 65% of subhalos with $z_{\mathrm{infall}} > 3.93$ finish at least three orbits. The latter population approach a uniform distribution in χ, indicating that memory of the initial orbital plane is lost after a few orbits within the host. It is clear that the assumption of spherical symmetry does not apply.

This result is not too surprising, however, since dark matter halos are generally triaxial in shape and the host will experience anisotropic mass redistribution as massive objects are biased toward filamentary accretion (see also, e.g., Zemp et al., 2009). Another possible source of orbital torque is substructure interaction. Slater & Bell (2013) used VL2 to show that a significant fraction of subhalos accrete as groups with correlated trajectories that lead to frequent interaction over time. Such interactions can lead to a complex redistribution of orbital energy and angular momenta for the low-mass subhalos that are abundant here (Sales et al., 2007; Ludlow et al., 2009). Though a more detailed inspection of orbits is required to assess the significance of these effects in VL2, our result highlights the importance of considering host
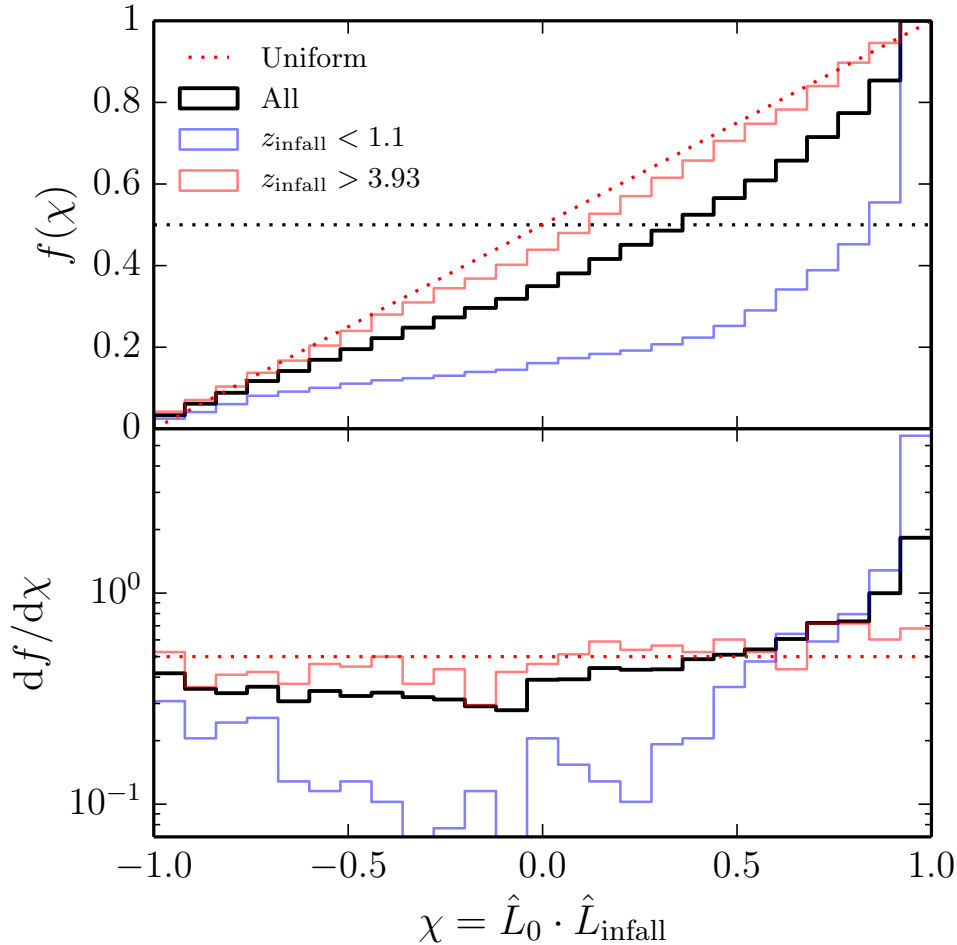
Figure 3.13: Cumulative (top panel) and differential (bottom panel) distributions in the dot product between the angular momentum normal vector at $z = 0$ and infall. The black histogram traces the total sample of subhalos while the blue and red histograms show the 1σ outliers with latest and earliest infall, respectively. Those subhalos that fell in recently tend to have their present-day angular momentum vector more closely aligned with the infall direction while subhalos that fell in earlier approach a uniform distribution in χ (shown for comparison as the dotted red line).

anisotropy and subhalo interaction in semi-analytic models of substructure evolution.

Subhalo internal structure: r_{max} and v_{max}

The main observable properties of luminous subhalos are their velocity structure, often described in terms of the circular velocity profile, $v^2 = GM(< r)/r$. In particular, most dynamical measurements provide robust constraints on the maximum circular velocity, v_{max}, and the radius at which this occurs r_{max}. In this section we show evolution in these two quantities as subhalos descend into the host. We refer to this as evolution in internal structure in the sense that v_{max} and r_{max} describe central density with $\rho_{max} \propto (v_{max}/r_{max})^2$ being the mean density within r_{max}.
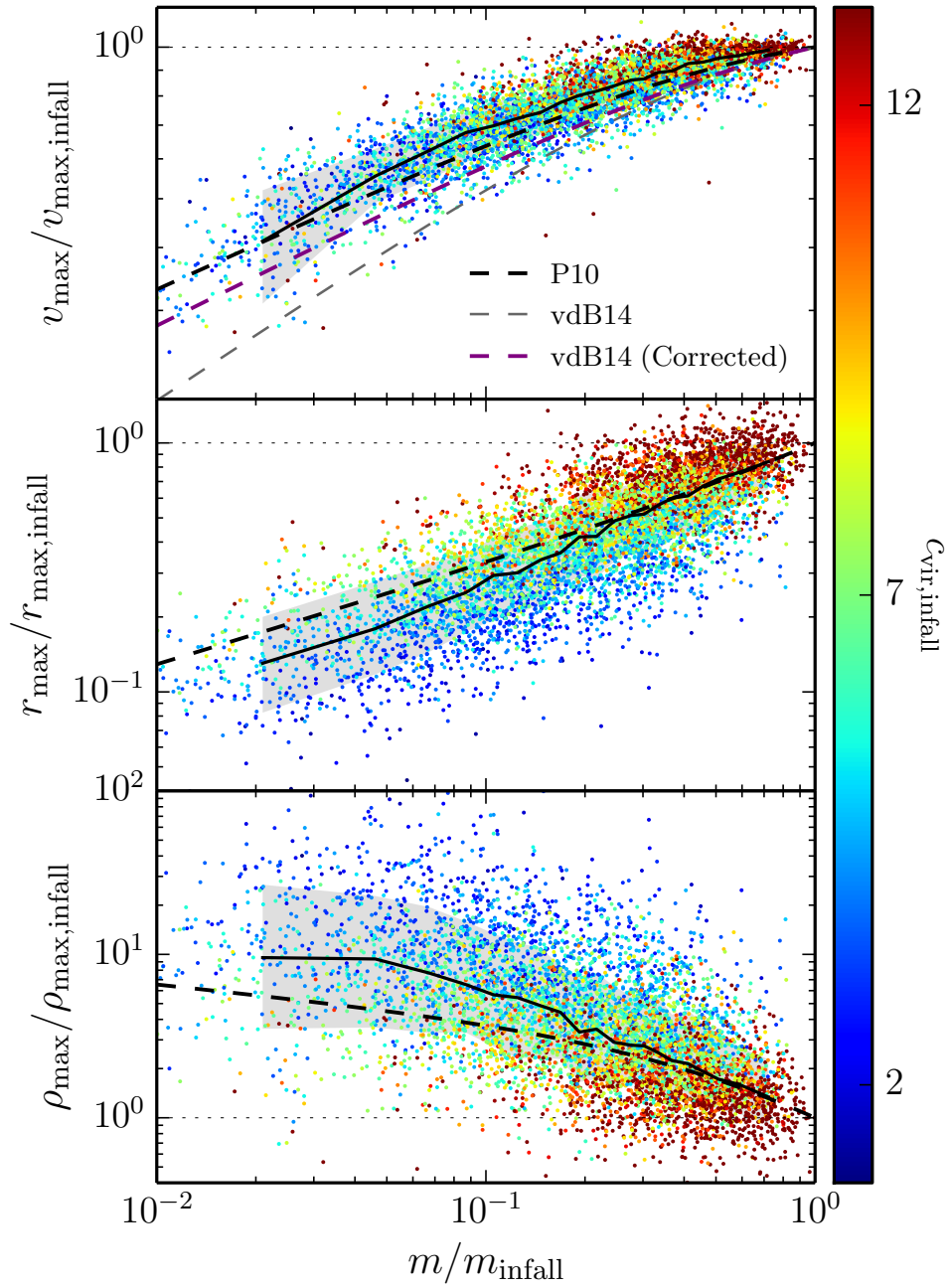
Figure 3.14: Evolution of v_{max} (top), r_{max} (middle), and ρ_{max} (bottom) as a function of mass retained at $z = 0$. In each panel, points represent individual subhalos coloured according to concentration at infall while the solid black line shows the median trend with the associated 1σ scatter shaded in gray. The P10 relation for isolated NFW subhalos of fixed concentration falling into a static host is shown as the dashed black line in each panel. The thin dashed gray line in the top panel traces the Bolshoi v_{max} relation as reported in van den Bosch & Jiang (2014), while the dashed purple line traces the corrected relation including only sufficiently resolved subhalos in Bolshoi (van den Bosch, private communication).

A number of previous works (Hayashi et al., 2003; Peñarrubia et al., 2008, 2010) have studied the evolution in r_{max} and v_{max} using numerical simulations where isolated subhalos are dropped into the potential of a static host. These studies come to the same conclusion that v_{max} and r_{max} evolve along tightly defined trajectories when written in terms of the mass fraction retained after infall. In particular, defining $x = m/m_{\mathrm{infall}}$ and taking y to represent either $r_{\mathrm{max}}/r_{\mathrm{max,infall}}$ or $v_{\mathrm{max}}/v_{\mathrm{max,infall}}$, it is found that subhalos starting at $(x, y) = (1, 1)$ move steadily along the track

$$y(x) = \frac{2^{\alpha} x^{\beta}}{(1+x)^{\alpha}}, \tag{3.14}$$

where α and β are fitting coefficients. For the case of NFW subhalos, Peñarrubia et al. (2010, P10) find the result $(\alpha, \beta) = (0.4, 0.3)$ for v_{max} and $(\alpha, \beta) = (-0.3, 0.4)$ for r_{max}.

In Figure 3.14 we plot the ratio of the present-day values of v_{max}, r_{max}, and ρ_{max} to their infall values versus the fraction of mass retained at $z = 0$. In each panel, the solid black line traces the median relation and the shaded region shows the 1σ scatter. The vast majority of subhalos experience reduction in r_{max} and v_{max}, with a larger suppression in the former, leading to a net increase in ρ_{max} with increasing mass loss. The median relation in each panel can be compared to the dashed black line showing the P10 result. We find VL2 agrees well with P10 for v_{max} but begins to diverge at low mass retention for r_{max} and ρ_{max}. The dashed gray line in the top panel shows equation (3.14) with $(\alpha, \beta) = (0.60, 0.44)$ which was reported by van den Bosch & Jiang (2014) to fit evolution in v_{max} for subhalos in the Bolshoi simulation. The VL2 data sits systematically above the Bolshoi result. The dashed purple line shows a corrected form $(\alpha, \beta) = (0.36, 0.33)$ which fits the Bolshoi relation when insufficiently resolved subhalos are removed from the sample (van den Bosch, private communication). This shows much better agreement with the VL2 result.

The points in Figure 3.14 are coloured in terms of subhalo concentration at infall. In the case of v_{max} we do not see much dependence on concentration other than the fact that subhalos with larger c_{vir} tend to have fallen in more recently and therefore have not had as much time to evolve to the left side of the plot. In contrast, r_{max} and ρ_{max} show strong stratification in c_{vir} with the least concentrated subhalos showing systematically greater reduction in r_{max} and enhancement in ρ_{max}. We offer a heuristic explanation as follows. Subhalos on slowly sinking orbits experience mass loss until the tidal radius shrinks to the point at which the mean interior density is proportional to the local density of the host. Since subhalos are exposed to (roughly) the same local density, those that were initially more dense (i.e., larger c_{vir}) naturally approach a smaller value of $\rho_{\mathrm{max}}/\rho_{\mathrm{max,infall}}$ at late times.

P10 do not find significant scatter since they consider subhalos of fixed concentration. They do find, however, that varying the *shape* of the subhalo inner density profiles at fixed concentration changes the coefficients α and β. We find the complementary result that varying concentration at fixed shape leads to substantially different structural evolution.

This point is made more illuminating by plotting v_{max} versus r_{max}, as in Figure 3.15. In the
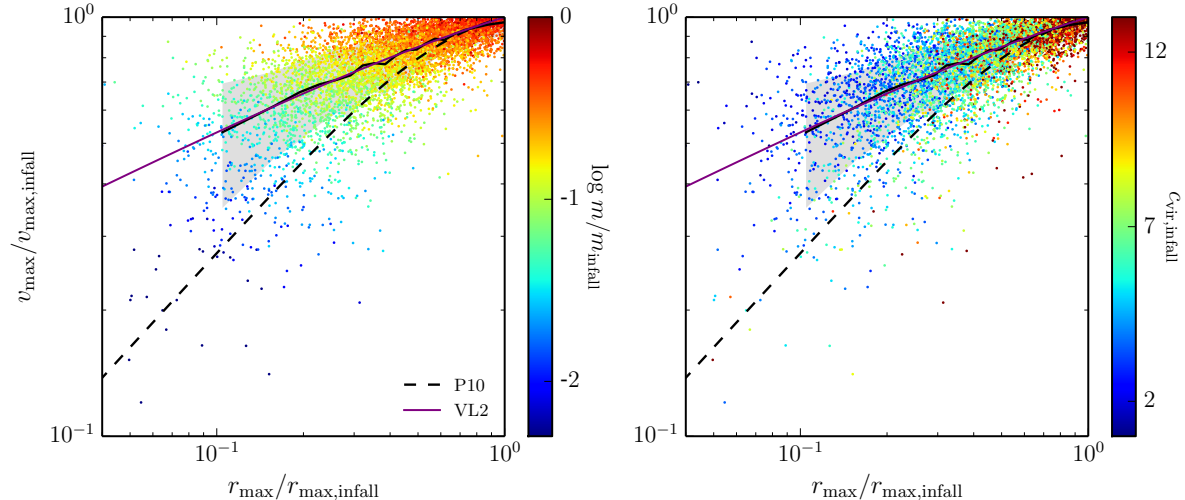
Figure 3.15: Evolution of subhalos in the normalized $v_{\mathrm{max}} - r_{\mathrm{max}}$ plane. Left panel shows subhalos coloured according to the fraction of mass remaining at $z = 0$ while the right panel colours subhalos according to their concentration at infall. The thick black line shows the median trend with the associated 1σ scatter shaded in gray. The thin purple line shows equation (3.14) with $(\alpha, \beta) = (0.25, 0.34)$ chosen to match the median relation. The dashed black line shows the P10 relation for isolated NFW subhalos of fixed concentration falling into a static host.

left panel we colour points according to the mass retained at $z = 0$ while the right panel shows concentration at infall. The left panel shows a clear gradient in colour, reinforcing the notion of previous works (Hayashi et al., 2003; Peñarrubia et al., 2008, 2010) that evolution in internal structure does not depend on *how* mass is lost, but only *how much* mass is lost. As expected, however, subhalos are not bound to a single trajectory in the $v_{\mathrm{max}} - r_{\mathrm{max}}$ plane. The right panel shows that scatter at fixed mass loss can be attributed to concentration, as in Figure 3.14. The median evolution for all subhalos is shown as the solid black line in each panel with 1σ scatter shaded in gray. The purple line fits the median trend using equation (3.14) with $(\alpha, \beta) = (0.25, 0.34)$. This sits above the P10 result that was derived from subhalos of fixed $c_{\mathrm{vir}} = 23$; a considerably larger value than the median concentration of 7 found in VL2.

3.5   Disrupted Subhalo Population

Up to this point we have only considered the population of subhalos that *survive* to the present day. This leaves open questions regarding any potential biases that may exist in our results due to the omission of *disrupted* subhalos. In this section we attempt to address these questions by making use of the second VL2 public catalogue.

The second catalogue contains a similar set of evolutionary tracks as the main catalogue except that it pertains to the 20000 largest systems in the simulation box identified at $z = 4.56$. The two catalogues are not mutually exclusive as some of the surviving subhalos at $z = 0$ also happened to be of the largest systems present at $z = 4.56$. The utility of the second
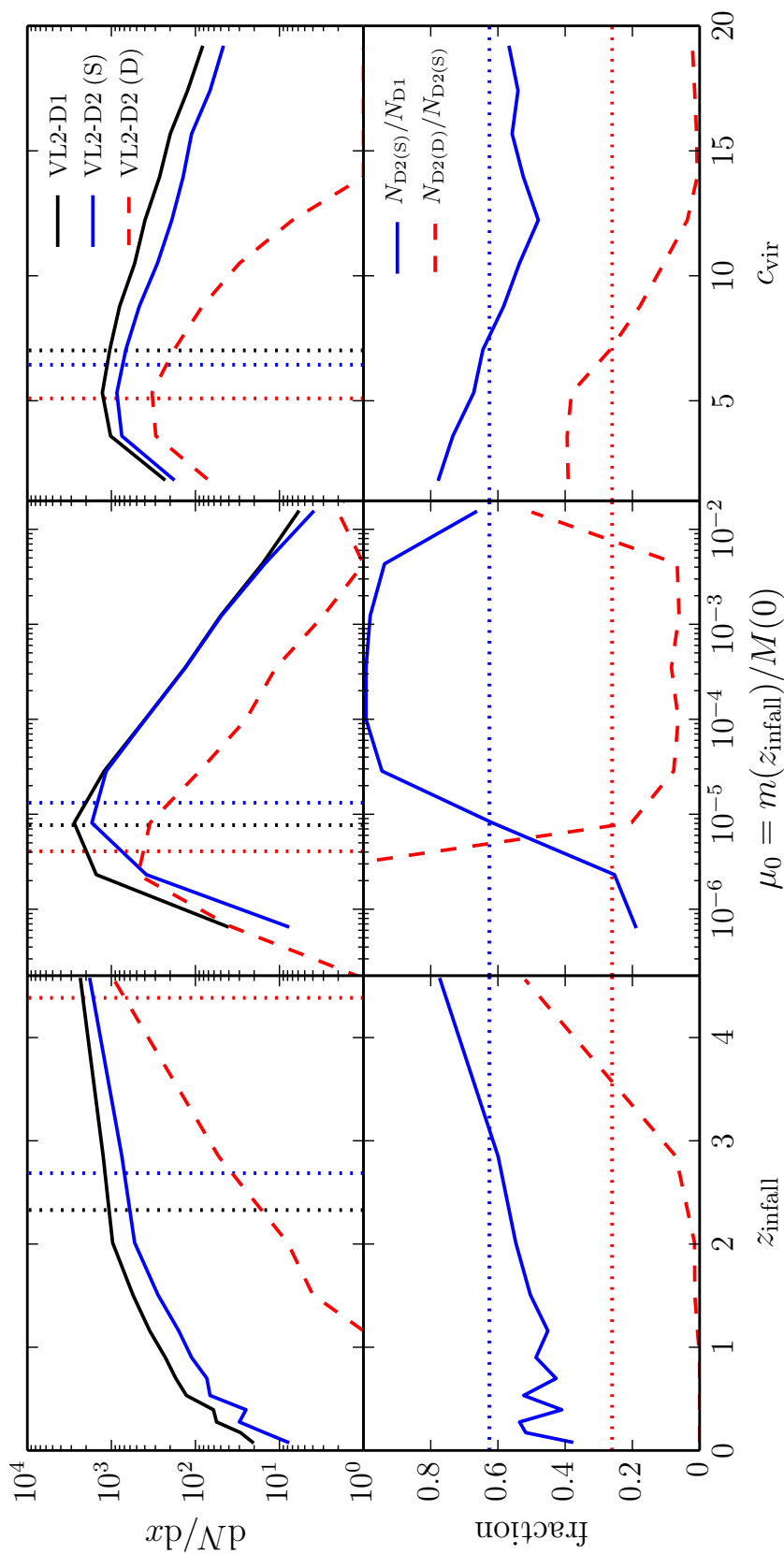
Figure 3.16: Top panels show the distribution of subhalos based on z_{infall} (left), mass ratio at infall (middle), and concentration at infall (right). The solid black line shows the distribution of subhalos from the main catalogue, VL2-D1, considered in the preceding sections of this paper. The solid blue (dashed red) line traces the distribution of surviving (disrupted) subhalos from VL2-D2. The vertical dotted lines show the median value of the distribution of the corresponding colour. The dashed red lines in the bottom panels trace the ratio $N_{\text{D2(D)}}/N_{\text{D2(S)}}$ of disrupted to surviving subhalos in VL2-D2 with the dotted red line showing the mean value 1000/3843. The solid blue lines trace the fraction $N_{\text{D2(S)}}/N_{\text{D1}}$ of surviving subhalos in VL2-D2 to surviving subhalos in VL2-D1. The dotted blue line shows the mean fraction 3843/6145.

catalogue is that it contains subhalos that disrupt prior to the present day. Though this does not constitute the *full* ensemble of disrupted subhalos (some subhalos that disrupt were not of the largest systems at $z = 4.56$) it should be enough to elucidate differences between surviving and disrupted subhalos. For convenience we henceforth refer to the main VL2 data set (considered in all preceding sections) as VL2-D1 and refer to the second data set as VL2-D2.

We apply the same framework outlined in §3.3 to VL2-D2. Namely, we identify subhalos as those systems that at some point passed within the instantaneous virial radius of the host. Of these subhalos we identify the surviving population as those that still exist as intact objects at $z = 0$. Conversely, the disrupted population consists of those subhalos that fall below the mass resolution of the VL2 halo finder some time before reaching $z = 0$. We find a total of 4843 subhalos in VL2-D2 of which 3843 (79%) belong to the surviving group and 1000 (21%) belong to the disrupted group. Note that $\sim 63\%$ of the 6145 subhalos from VL2-D1 are also part of VL2-D2.

We examine in Figure 3.16 the dependence of survivability on infall redshift, mass ratio, and concentration. In the top panels, we plot the distribution in each quantity for all surviving (disrupted) subhalos from VL2-D2 as solid blue (dashed red) lines. For comparison, the solid black line traces the distribution in each quantity for the VL2-D1 subhalos. The vertical dotted lines denote the median value of the distribution with the corresponding colour. In the bottom panels, the dashed red line traces the ratio, $N_{\rm D2(D)}/N_{\rm D2(S)}$, of disrupted to surviving subhalos in VL2-D2, with the horizontal red line denoting the mean value 1000/3843. To test for bias in the surviving fraction of VL2-D2 subhalos, the solid blue line traces the ratio, $N_{\rm D2(S)}/N_{\rm D1}$, of the surviving subhalos in VL2-D2 to the full ensemble of surviving subhalos contained in VL2-D1. The horizontal blue line denotes the mean fraction 3843/6145.

We begin with infall redshift. The blue line in the bottom left panel shows that VL2-D2 is slightly biased towards containing those surviving subhalos with larger values of $z_{\rm infall}$. This reflects the fact that subhalos with smaller values of $z_{\rm infall}$ were less likely to exist as large objects at $z = 4.56$ when VL2-D2 was constructed. Comparing the surviving and disrupted populations in VL2-D2 shows that subhalos with $z_{\rm infall} \gtrsim 3$ are much more likely to belong to the latter group. That is, subhalos spending more time exposed to the tidal field of the host are more likely to disrupt by the present day.

Next we investigate mass ratio at infall. The middle panels of Figure 3.16 show little dependence of survivability in the mass range $10^{-5} \lesssim \mu_0 \lesssim 10^{-2}$. For larger masses, we expect the disrupted fraction to increase as dynamical friction preferentially causes massive subhalos to plummet into the depths of the host where tidal forces are strongest. We indeed see an upturn at $\mu_0 \gtrsim 10^{-2}$ though VL2 is hindered by small number statistics in this regime to make a meaningful statement here. We also observe a rapid rise in the disrupted fraction for $\mu_0 \lesssim 10^{-5}$. This is expected due to the finite mass resolution of the simulation – subhalos closer to the resolution limit are more likely to "disrupt". There is a related drop in the blue line in the bottom middle panel indicating that the missing surviving population in VL2-D2 are
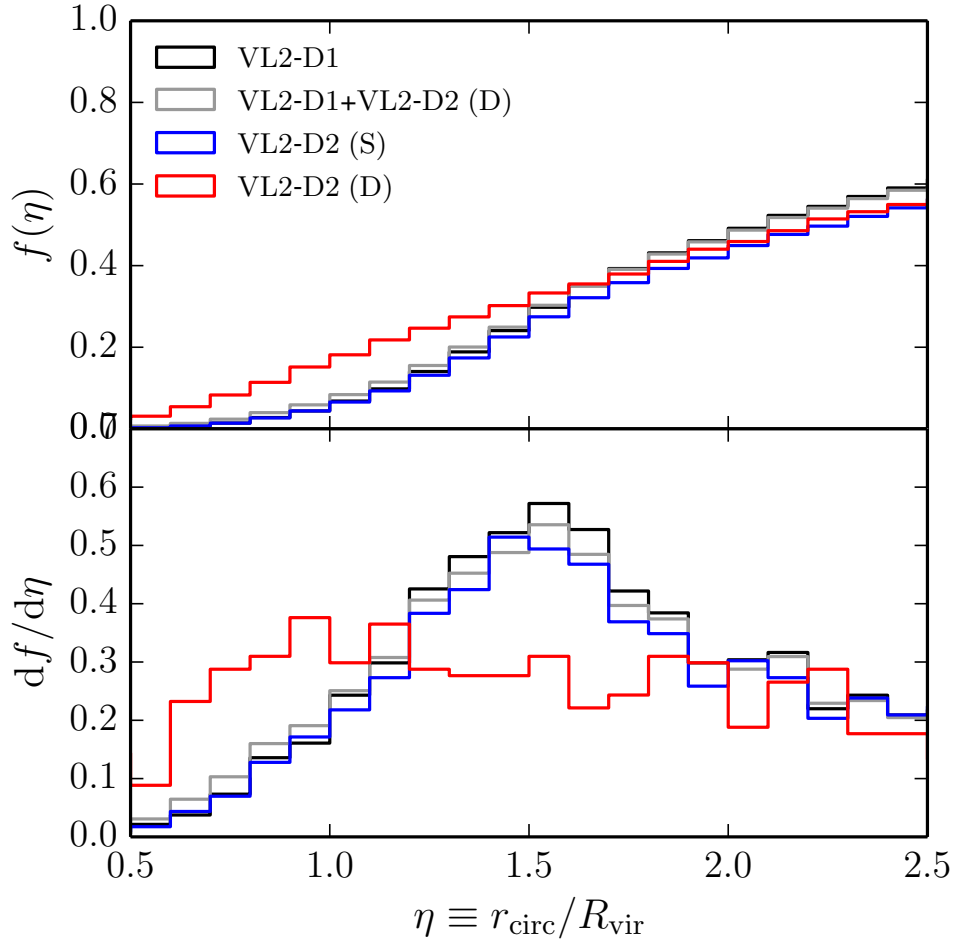
Figure 3.17: Cumulative (top panel) and differential (bottom panel) distributions in η for all surviving VL2 subhalos (black histogram), the surviving subhalos in the VL2-D2 catalogue (blue histogram), and the disrupted subhalos in the VL2-D2 catalogue (red histogram). The gray histogram shows the result of combining the total population of surviving subhalos with the VL2-D2 disrupted population. In each case we report η at z_{infall} for an NFW host potential. The results are qualitatively similar if we consider virial crossing with a point mass host potential.

almost exclusively low-mass subhalos. This reflects the early infall bias in VL2-D2: subhalos nearer the resolution limit are only likely to survive to $z = 0$ if they infall later.

We finish by examining infall concentration in the right panels of Figure 3.16. First, we see that VL2-D2 is biased towards containing low-concentration surviving subhalos, consistent with the early infall bias via the concentration-redshift relation (see Figure 3.5). Moreover, of all subhalos in VL2-D2, those with $c_{\mathrm{vir}} \lesssim 5$ are much more likely to disrupt by $z = 0$. This is consistent with our previous finding that low-concentration subhalos are more susceptible to tidal stripping from the host (see Figure 3.11). In fact, the strong dependence of survivability on c_{vir} and not on μ_0 strengthens the notion that mass loss is more strongly connected to concentration than mass for low-mass ($\mu_0 \lesssim 10^{-3}$) subhalos.

We now shift focus to the infall distribution of orbital energy and angular momentum for
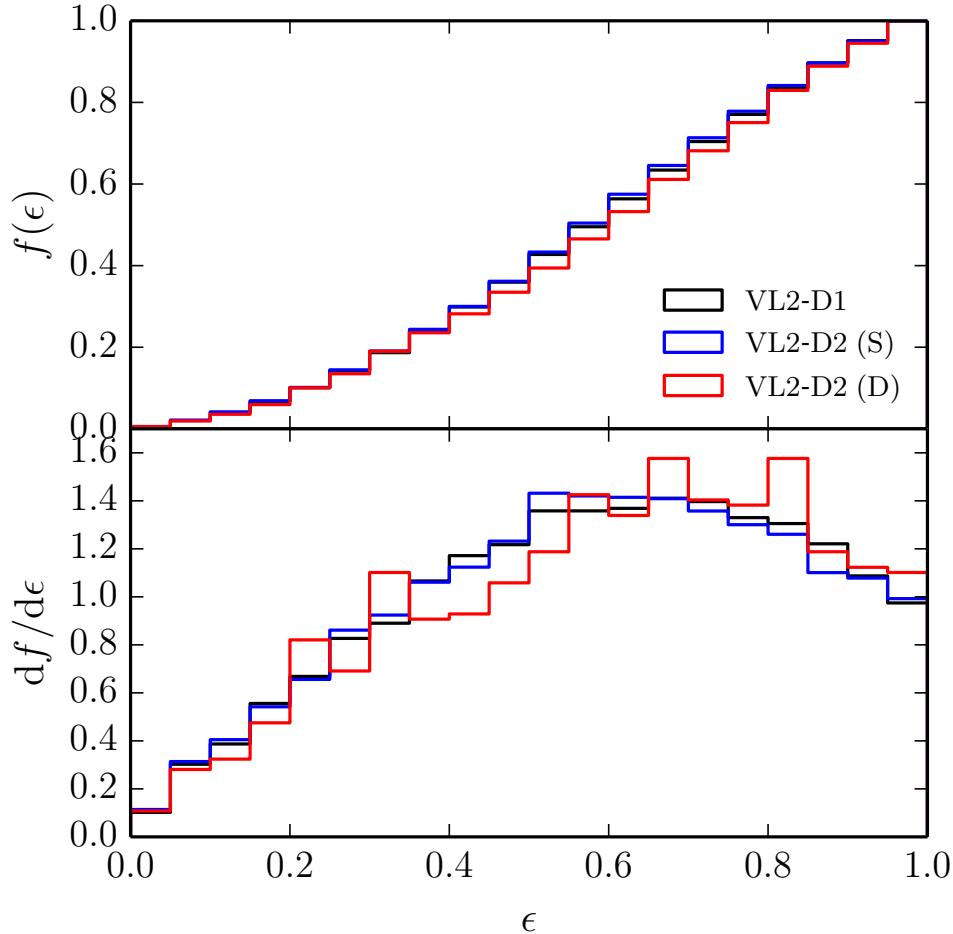
Figure 3.18: Cumulative (top panel) and differential (bottom panel) distributions in ϵ for all surviving VL2 subhalos (black histogram), the surviving subhalos in the VL2-D2 catalogue (blue histogram), and the disrupted subhalos in the VL2-D2 catalogue (red histogram). In each case we report ϵ at z_{infall} for an NFW host potential. The results are qualitatively similar if we consider virial crossing with a point mass host potential.

surviving versus disrupted subhalos. In Figure 3.17 we plot the infall distribution of η for the surviving (disrupted) subhalos in VL2-D2 as a blue (red) histogram. The blue histogram can be compared to the black histogram showing the infall distribution for all surviving subhalos in VL2-D1 (i.e., the black histogram in Figure 3.7). We see good agreement between the surviving VL2-D2 subhalos and the full VL2-D1 population. The disrupted population, on the other hand, agrees well with the other curves for $\eta > 2$, but displays a much flatter distribution for smaller η. Most importantly is the excess at $\eta < 1$, indicating that subhalos strongly bound to the host at infall are preferentially disrupted by $z = 0$.

This result suggests that the black histogram is suppressed at $\eta < 1$ compared to the distribution of *all* subhalos that ever fell onto the host, regardless of survivability. The gray histogram in Figure 3.17 shows the result of combining the disrupted subhalos in VL2-D2 with the VL2-D1 catalogue. Doing so results in only a minor change to the black histogram

since there are six times fewer disrupted subhalos than surviving subhalos. Though we do not have access to the full ensemble of disrupted subhalos, it seems unlikely that we are missing a large enough fraction for there to be a significant impact on the infall distribution and fitting functions for η presented in §3.4.3.

In Figure 3.18 we plot the infall distribution of ϵ for the surviving (disrupted) subhalos in VL2-D2 as a blue (red) histogram. The surviving population can be compared to the black histogram showing the infall distribution for all surviving subhalos in VL2-D1 (i.e., the black histogram in Figure 3.9). In this case, we see good agreement between all histograms. Hence, unlike orbital energy, angular momentum does not appear to play a significant role in determining the survivability of subhalos. The infall distribution and fitting functions for ϵ presented in §3.4.3 are therefore robust to the inclusion of disrupted subhalos.

3.6   Summary

We have analyzed the publicly available VL2 halo catalogue in order to characterize the infall properties, orbital dynamics, and structural evolution of over 6000 subhalos within a galactic host. Our main focus is on the role of subhalo concentration in each of these categories, and how this relates to $z = 0$ observables, such as circular velocity and size.

We define subhalo infall as the time when a halo reaches maximum mass. In other words, a halo becomes a subhalo when its growth is halted, mainly due to tidal truncation from the host. After infall, subhalos experience mass loss from tidal forces and exhibit internal readjustment as they gradually sink toward the host center. We focus on low-mass subhalos for which dynamical friction plays only a minor role, leading to qualitatively different behaviour than is often described for high-mass subhalos. In the following paragraphs we report the main results of our paper.

Subhalo mass function: We compare the unevolved and evolved subhalo mass functions with the results published from the Aquarius simulations. The unevolved mass function uses the mass of each subhalo *when it fell in* while the evolved mass function uses the mass at $z = 0$, showing the cumulative effect of tidal mass loss after infall. While the unevolved mass functions agree well, the evolved VL2 mass function is systematically lower, by 30%, corresponding to a downward shift in mass (Figure 3.2). The lower normalization of the VL2 simulation ($\sigma_8 = 0.74$ vs. $\sigma_8 = 0.9$) could be the origin, although the physical explanation remains unclear (see §3.4.2).

Properties at infall: Several important relationships among subhalo properties at the time of infall emerge: (1) The typical infalling halo mass does not evolve significantly with time, with a value of $\sim 10^7\ M_\odot$ (Figure 3.5 and also Figure 3.16). (2) Rare, massive halos fall in much later than less massive ones, as expected in hierarchical structure formation (Figure 3.3). (3) Halos that fall in earlier have lower concentrations, consistent with the well-known concentration-mass-redshift relationship for dark matter halos at fixed mass (e.g., Klypin et al., 2011, see Figure 3.5). (4) Halos that fall in earlier or, equivalently, that have lower concentrations at

infall, tend to experience tidal growth truncation at a larger radius (Figures 3.4 and 3.5).

Energy and angular momentum: The orbital energy and angular momentum of sub-halos at infall are significantly different than reported in previous studies that focused on more massive subhalos. The low-mass subhalos found in VL2 are skewed toward lower specific binding energy (Figure 3.7) and slightly more circular orbits (Figure 3.9). This is consistent with the recent results of Jiang et al. (2015). The explanation for these trends may be related to the environment in which objects form – massive subhalos fall into the host preferentially along filaments, leading to tightly bound, radial orbits – and/or gravitational interactions prior to infall that preferentially inject energy and tangential motion into low-mass subhalo orbits.

Mass loss: We find that subhalos undergo most of their mass loss on the first pericenter passage, with a median mass loss fraction of ~ 0.2 (Figure 3.10). The fraction of mass lost in the first pericenter passage is most correlated with halo concentration at infall – less concentrated halos tend to undergo more mass loss, nearly independent of mass (Figure 3.11). There is a significant but less pronounced correlation of mass loss fraction with subhalo mass, but this trend is only apparent, being explained by the fact that more massive halos have lower concentrations on average and are thus more susceptible to tidal effects. Scatter in mass loss at fixed concentration can be mainly attributed to eccentricity with radial orbits tending to lose more mass than circular orbits.

Orbital period: The period of the first orbit after infall is roughly proportional to the dynamical time of the host halo, $t_{\mathrm{orb}} \propto \tau_{\mathrm{dyn}} \propto [\Delta(z)\rho_{\mathrm{crit}}(z)]^{-1/2}$. There is significant scatter, however, in the apocenter, $r_{\mathrm{apo}}/R_{\mathrm{vir}}$, which results in a comparable scatter in $t_{\mathrm{orb}}/\tau_{\mathrm{dyn}}$ (Figure 3.12). The scatter originates in the concentration of the infalling subhalos: low-concentration subhalos begin to be disrupted earlier and thus experience much longer initial orbits than subhalos with higher concentrations.

Spherical Symmetry: Motion in a spherical potential, in which the direction of angular momentum does not change, is not a good approximation to subhalo orbital dynamics. In particular, the direction of the angular momentum vector is not fixed. After a few orbits, the direction of the angular momentum is essentially randomized. This seems to be a generic feature of subhalo evolution in highly inhomogeneous, triaxial host halos (Figure 3.13).

Evolution in the v_{max}–r_{max} plane: As subhalos are tidally disrupted by the host halo, their maximum circular velocities and radii steadily decrease, tracing out tracks in the v_{max}–r_{max} plane. While the joint median evolution, as well as their individual dependence on tidal mass, are in qualitative agreement with previous studies, we find a substantial amount of scatter. Furthermore, this scatter can be mostly attributed to variations in the concentration at infall. The difference is most pronounced in the evolution of r_{max}: subhalos that are *more concentrated* at infall experience a *weaker evolution* in r_{max} as they lose mass (Figure 3.14). Concentration at infall determines evolution in the v_{max}–r_{max} plane (Figure 3.15).

Disrupted Subhalo Population: We find that subhalos with early infall and/or low

concentration are preferentially disrupted within the host (Figure 3.16). We find no dependence of survivability on mass within the range probed by VL2. These results are consistent with the notion that tidal mass loss is correlated with concentration instead of mass for low-mass subhalos. The typical infalling mass of $m \sim 10^7 \ M_\odot$ ($\mu_0 \sim 10^{-5}$) is true for both surviving and disrupted subhalos. Circularity does not influence subhalo survivability. There is a slight bias in tightly bound orbits with $\eta < 1$ being preferentially disrupted though this is a relatively small effect. The infall distributions and fitting functions for η and ϵ presented in §3.4.3 and §3.4.3 based on surviving VL2 subhalos should do a good job at representing the infall distribution for *all* subhalos (surviving plus disrupted) that ever fell onto the host (Figures 3.17 and 3.18). This is the case at both z_{infall} with an NFW host potential as well as z_{cross} with a point mass host potential.

In this work we have extended previous detailed analyses of subhalo dynamics and evolution to the much lower mass ratios probed by the Via Lactea II data. We have found qualitatively different behaviour in this low-mass regime, with dynamical friction and orbital dynamics playing a lesser role, and the interior structure of the subhalos, expressed in terms of concentration, playing a much more important role.

The 'concentration bias' we find here raises the prospects of significantly improving our ability to connect ultra-faint dwarf galaxies to the primordial fluctuations from which they collapsed. More detailed study, in particular with finer time resolution and a larger sample of simulated Galactic host halos, will be necessary before we can reliably use concentration bias in near field cosmology.

Acknowledgements

Chapter 4

Precision reconstruction of the cold dark matter-neutrino relative velocity from N-body simulations

4.1 Chapter Overview

Discovering the mass of neutrinos is a principle goal in high energy physics and cosmology. In addition to cosmological measurements based on two-point statistics, the neutrino mass can also be estimated by observations of neutrino wakes resulting from the relative motion between cold dark matter (CDM) and neutrinos. Such a detection relies on an accurate reconstruction of the CDM-neutrino relative velocity which is affected by nonlinear structure growth and galaxy bias. We investigate our ability to reconstruct this relative velocity using large N-body simulations where we evolve neutrinos as distinct particles alongside the CDM. We find that the CDM velocity power spectrum is overpredicted by linear theory whereas the neutrino velocity power spectrum is underpredicted. The magnitude of the relative velocity observed in the simulations is found to be lower than what is predicted in linear theory. Since neither the CDM nor the neutrino velocity fields are directly observable from galaxy or 21 cm surveys, we test the accuracy of a reconstruction algorithm based on halo density fields and linear theory. Assuming prior knowledge of the halo bias, we find that the reconstructed relative velocities are highly correlated with the simulated ones with correlation coefficients of 0.94, 0.93, 0.92 and 0.88 for neutrinos of mass 0.05, 0.1, 0.2 and 0.4 eV. We confirm that the relative velocity field reconstructed from large scale structure observations such as galaxy or 21 cm surveys can

be accurate in direction and, with appropriate scaling, magnitude.

4.2   Introduction

Despite extensive research in the particle physics and cosmology communities, many properties of neutrinos remain elusive. For instance, neutrino oscillation experiments (Fogli et al., 2012) have accurately measured the mass-squared splittings between neutrino species, but individual neutrino masses have yet to be measured. It is also unknown whether the neutrino masses follow a *normal* hierarchy in which there are two light neutrinos and a single heavy one, an *inverted* hierarchy with the opposite configuration or are *quasi-degenerate* with all three masses being approximately equal and much larger than the mass splittings. Moreover, it is still unknown whether neutrinos are Dirac or Majorana fermions.

Cosmological techniques for determining neutrino masses are currently insensitive to individual neutrinos and instead constrain the sum of all neutrino masses. For instance, cosmic microwave background (CMB) observations made by the Plank satellite place $\sum m_\nu < 0.194 \, \mathrm{eV}$ (Planck Collaboration et al., 2015). Recently, a new technique for constraining neutrino mass using large-scale velocity fields was proposed in Zhu et al. (2014a,b). Neutrinos and cold dark matter (CDM) are expected to have a relative velocity arising due to the free streaming of neutrinos over large scales. As neutrinos bulk flow over large scale structures they become focussed into wakes. Such downstream overdensities introduce a unique dipole distortion in the matter field in the direction of the neutrino flow which could be observed via either direct lensing of the wake or through a dipole component of the correlation function.

Unlike other probes of cosmological neutrinos, this method is expected to be background free and only relies on knowledge of the relative velocity field. Determining velocity fields directly is particularly challenging even for luminous matter and certainly impossible for neutrinos. However, the relative velocity is predicted to be coherent over several megaparsecs. We therefore expect linear theory to be accurate enough to allow for a reconstruction of the velocity field from the easier to obtain matter density field.

Our goal is to quantify the accuracy of this linear reconstruction when nonlinear structure formation, which affects both the density and velocity fields, is taken into account. We furthermore wish to understand whether the reconstruction procedure is robust when only a *tracer* of the CDM field is used. To achieve this we use large cosmological simulations. Neutrinos have been implemented in a variety of ways within the framework of N-body simulations: (i) Brandbyge & Hannestad (2009) used a grid-based approach where an additional neutrino density field is evolved alongside N-body CDM; (ii) Brandbyge & Hannestad (2010) employed a hybrid method where neutrinos start as a grid and are converted to particles as their energy decreases; (iii) Bird et al. (2012) evolved neutrinos as distinct N-body particles; (iv) Ali-Haïmoud & Bird (2013) computed the neutrino linear response alongside the evolving CDM. In general, the grid-based approaches have been unable to resolve nonlinear neutrino structure formation

while particle-based approaches are hindered by the requirement that many neutrino particles are needed to reduce Poisson noise on small scales. In this work, we adopt the particle based approach since an accurate computation of nonlinear neutrino dynamics is a main focus of our work.

In §4.3 we discuss our implementation of neutrino particles into the cosmology code CUBEP³M (Harnois-Déraps et al., 2013) and our method for computing density and velocity fields. In §4.4 we present the results of our simulations and analyze the accuracy of various reconstruction methods. In §4.5 we discuss a practical procedure to estimate cosmic velocity fields from density tracers.

4.3 Theory and Implementation

4.3.1 Neutrino N-body Particles in CUBEP³M

We simulate a single neutrino species as an N-body particle. Initial neutrino positions are generated separately from CDM using the same Gaussian noise map. We use neutrino density transfer functions, T_δ, computed via CAMB (Lewis et al., 2000) for a universe with one massive and two massless neutrinos. The initial neutrino velocity is composed of two parts: a linear component (analogous to the Zel'dovich velocity) plus a random thermal component. For the linear component, we first compute the linear neutrino velocity transfer function, T_v, via the continuity equation under the assumption that initial conditions are adiabatic and velocities are linear (e.g. $\delta(k,z) = T_\delta(k,z)\delta_i(k)$ and $\vec{v}(\vec{k},z) = T_v(k,z)\delta_i(k)\hat{k}$ for an initial perturbation $\delta_i(k)$):

$$\dot{\delta} + \frac{1}{a}\vec{\nabla} \cdot \vec{v} = 0 \rightarrow T_v = -i\frac{H}{k}\frac{T_\delta(z+\delta z) - T_\delta(z - \delta z)}{2\delta z}, \tag{4.1}$$

where we convert time derivatives to redshift derivatives and evaluate numerically using a spacing $\delta z = 0.1$. We have checked that the transfer functions computed via equation 4.1 are in good agreement with those produced by the CLASS code (Blas et al., 2011) in Newtonian gauge[1].

From this velocity transfer function, we compute a velocity potential, $\phi_v(k)$, such that $\vec{v}(k) = i\vec{k}\phi_v(k) = (T_v/T_\delta)\delta\hat{k}$. When combined with equation 4.1 this yields:

$$\phi_v(k) = -\frac{H}{k}\frac{T_\delta(z+\delta z) - T_\delta(z-\delta z)}{2\delta z}\frac{\delta}{T_\delta}. \tag{4.2}$$

This potential is then Fourier transformed and a two-sided finite difference is taken to obtain the linear velocity. Using a real-space gradient reduces the number of Fourier transforms to be computed and is consistent with our calculation of the displacement field.

---

[1]The CAMB density transfer functions are in the synchronous gauge whereas the velocity transfer function we desire are in the longitudinal Newtonian gauge. However, the gauge transformation terms are proportional to the time derivatives of the Newtonian potentials which we already ignore in the continuity equation.

The random component of the velocity is computed via the cumulative distribution function, $\text{CDF}[v, \beta]$, which follows from the relativistic Fermi-Dirac distribution, $\text{PDF}[v, \beta]$, for neutrinos:

$$
\begin{aligned}
\text{PDF}[v, \beta] &= \frac{1}{N} \left(\frac{m_\nu}{kT}\right)^3 \frac{v^2}{e^{m_\nu v/kT} + 1} = \frac{\beta^3}{N} \frac{v^2}{e^{v\beta} + 1} \\
\text{CDF}[v, \beta] &= \int_0^v \text{PDF}[u, \beta] du \\
&= \frac{1}{N} \int_0^{w=\beta v} \frac{w^2}{e^w + 1} dw \\
&= \text{CDF}[\beta v, 1]
\end{aligned}
\tag{4.3}
$$

where m_ν and T are neutrino mass and temperature, respectively, $\beta \equiv m_\nu/kT$ and $N = \int_0^\infty w^2/(e^w + 1)dw \simeq 1.803$ is a normalization constant. Our numerical evaluation of the CDF gives a maximum particle speed of $0.013\,(0.2\,\text{eV}/m_\nu)\,(1 + z_i)c$ for a given starting redshift z_i. Neutrinos in the mass regime we are interested in are relativistic at the redshift for which CDM initial conditions are generated ($z_c = 100$):

$$
\langle v \rangle = \frac{\int_0^\infty v \text{PDF}[v, \beta] dv}{\int_0^\infty \text{PDF}[v, \beta] dv} \approx 800 \left(\frac{0.2\,\text{eV}}{m_\nu}\right)(1 + z)\,\text{km s}^{-1}.
\tag{4.4}
$$

This thermal motion would dominate the time step constraining the maximum distance a particle may travel, making the simulation impractically slow. To circumvent this issue we evolve the CDM in isolation to a lower redshift, $z_\nu \sim 10$, at which point neutrinos are added and the two components evolve together.

During their subsequent evolution, CDM and neutrino particles are treated identically except for their masses, which are weighted by their energy fractions as well as number ratio:

$$
m_i = \frac{\Omega_i}{\Omega_m} \frac{N_g}{N_i},
\tag{4.5}
$$

where Ω_i is the energy fraction of species i, Ω_m is the total matter energy fraction, N_g is the number of cells in the simulation grid, and N_i is the number of particles of species i. These masses are used when adding particles to the grid for the computation of the long-range gravitational force as well as the short-range pairwise force. The particle type is distinguished within the code using 1 byte particle identification tags.

4.3.2 Density and Velocity Fields

We compute CDM, neutrino, and halo density fields using a standard cloud-in-cell interpolation method for both CDM and neutrinos. Computing velocity fields from particle-based simulations has only recently been studied in depth. This may be related to the ambiguity associated with defining a velocity field from a sample of point particles. Unlike quantities such as mass or momentum, the velocity of a particle cannot be simply added to a grid. The most obvious

method for generating a velocity field is to divide a gridded momentum field by its corresponding density field. However, within void regions it is possible that empty cells exist for which no well-defined velocity can be assigned. Alternatively, one may define the velocity at a given grid cell to be the average velocity of the N_{near} nearest particles about this point. The application of the nearest particle method was studied by Zhang et al. (2015) and Zheng et al. (2015) where it was found that the velocity power is suppressed for low particle number densities, $n < 1$ (Mpc/h)$^{-3}$, due to the sampling procedure. In our simulations we use high number densities, $n_{\text{dm}} \sim 10$ (Mpc/h)$^{-3}$, and therefore do not expect this effect to be significant. More advanced methods for computing velocity fields exist such as phase-space interpolation discussed in Pueblas & Scoccimarro (2009) and more recently in Hahn et al. (2014). The neutrino velocity distribution has been studied by Villaescusa-Navarro et al. (2013).

In what follows we compute the velocity fields of CDM and neutrinos in different ways. For CDM, we adopt the nearest particle method and take the $N_{\text{near}} = 1$ nearest particle about the centre of each cell using the same grid resolution as neutrinos. We have found that the nearest particle method can also be used for neutrinos albeit with a much larger $N_{\text{near}} = 64$ to smooth the field on small scales. However, searching over this many particles is a computationally expensive task. For neutrinos we therefore employ the approach of dividing their momentum field by their density field on grids coarsened so that there is always at least one neutrino per cell. This is possible since neutrinos are rather homogeneously distributed and form voids to a lesser extent than CDM.

We treat the velocity fields obtained from the nearest particle and momentum methods as faithful tracers of the actual field. However, these fields are not comparable to observational data since neither CDM nor neutrino velocities can be directly measured. For this purpose we reconstruct velocity fields from density fields using linear theory:

$$\vec{v} = \frac{T_v}{T_\delta} \frac{\vec{k}}{k} \delta, \tag{4.6}$$

where we use CDM and halo density fields separately for δ (although with the same T_δ). In what follows we treat halos as point particles of unit mass in order to represent the information available through galaxy surveys.

Poisson noise is a severe hindrance in computing neutrino statistics as the large thermal velocity causes neutrino particles to be more homogeneously distributed. For density spectra it is possible to subtract out the flat Poisson noise spectrum but this is not possible for velocity fields. Instead, we use a method that exploits the fact that Poisson noise arises from particles being randomly distributed. The procedure for either density or velocity fields is:

1. Randomly divide the particles into two groups.

2. Interpolate particles of each group into a field (density or velocity).

3. Compute the cross spectrum between groups as an estimate of the auto spectrum.

This procedure ensures that Poisson noise is highly suppressed as the noise between the two groups is uncorrelated due to the random assignment to groups. We use this method for density and velocity auto-spectra for both CDM and neutrinos; we do not use it for CDM-neutrino cross spectra where it is redundant (there are already two groups of particles).

The accuracy of the reconstructed field is measured using a correlation coefficient:

$$r_{ij}(k) = \frac{\Delta_{ij}^2(k)}{\sqrt{\Delta_{ii}^2(k)\Delta_{jj}^2(k)}} \tag{4.7}$$

where Δ_{ij}^2 is the cross power spectrum between species $i = c, h, \nu$ or rel using reconstruction method sim, Rec DM, Rec HA (nearest particle/momentum, equation 4.6 with CDM and equation 4.6 with haloes respectively) and species j (with potentially a different reconstruction method). We also define the integrated correlation coefficient as:

$$r_{ij} = \frac{\int \Delta_{ij}^2 \frac{dk}{k}}{\sqrt{\int \Delta_{ii}^2 \frac{dk}{k}}\sqrt{\int \Delta_{jj}^2 \frac{dk}{k}}} \tag{4.8}$$

which no longer depends on wavenumber.

4.4 Results

In this section we present the results for a suite of four simulations of CDM and neutrinos. We simulate neutrinos of mass $m_\nu = 0.4, 0.2, 0.1$ and $0.05\,\mathrm{eV}$. Each simulation contains $N_c = 1536^3$ CDM particles and $N_\nu = 3072^3$ neutrino particles within a periodic box of side length $L = 500\,\mathrm{Mpc/}h$. In each case CDM is started from an initial redshift $z_c = 100$ and gravitational forces are softened below the scale $r_{\mathrm{soft}} = 24\,\mathrm{kpc/}h$. Neutrinos are added in at redshift 10 for all species except $0.05\,\mathrm{eV}$ which we add at redshift 5. We assume a base cosmology compatible with Planck results: $\Omega_b = 0.05$, $\Omega_c = 0.27$, $\sigma_8 = 0.83$, $n_s = 0.96$, $h = 0.67$, and compute

$$\Omega_\nu = \frac{m_\nu}{93.14\,h^2} \tag{4.9}$$

as in Mangano et al. (2005). We hold Ω_b and Ω_c fixed in each simulation and maintain a flat universe by adjusting $\Omega_\Lambda = 1 - \Omega_m = 1 - \Omega_b - \Omega_c - \Omega_\nu$. In what follows we mainly investigate a fiducial simulation with $m_\nu = 0.2$ eV. We label our simulations based on neutrino mass with S05, S1, S2, and S4 denoting the simulations with $m_\nu = 0.05, 0.1, 0.2$, and $0.4\,\mathrm{eV}$ respectively.

Halo catalogues are generated for each simulation at $z = 0$ using a spherical overdensity algorithm that considers all halos with at least 100 CDM particles. This corresponds to a minimum halo mass of $3 \times 10^{11}\,M_\odot/h$. Recall, however, that we assign each halo unit mass when constructing halo density fields in order to emulate the information available in galaxy surveys. In what follows, density and velocity fields for CDM, neutrinos, and halos are computed

on uniform rectilinear grids containing 1536^3 mesh cells.

4.4.1 Density

Figure 4.1 compares slices of the CDM and halo density fields at $z = 0$ from simulation S2 to the neutrino density fields from simulations S05, S1, S2, and S4. It is easy to see that the neutrino density fields are correlated with the CDM density field albeit with much less clumping in the former than the latter as evidenced by their respective colour bars. In addition, we see that higher mass neutrinos tend to clump more than lower mass neutrinos as they are more influenced by the underlying CDM distribution due to their lower thermal velocities.

Figure 4.2 shows the dimensionless power spectra for CDM, halos, and neutrinos at $z = 0$ from S2. Also plotted are theoretical predictions for CDM and neutrinos, which are computed via

$$\Delta_i^2(k) = \frac{k^3}{2\pi^2} P_m \left(\frac{T_i}{T_m} \right)^2, \tag{4.10}$$

where T_i is the linear transfer function for species i, T_m is the total matter linear transfer function, and P_m is either the linear (computed from CAMB) or the nonlinear [computed from HALOFIT (Smith et al., 2003)] total matter power spectrum. We first note that the group cross-correlation method we employ effectively removes the shot noise allowing us to understand statistical properties even of the noisy neutrino density field. We find that the CDM power spectrum agrees well with the nonlinear prediction up to large k. The neutrino power spectrum, on the other hand, is significantly enhanced on small scales compared to the theoretical curve demonstrating that the linear response of equation 4.10 fails to capture neutrino dynamics on small scales. This trend was previously observed by Ali-Haïmoud (private communication) and modelled in Massara et al. (2014).

Despite their enhanced power on small scales, neutrinos remain highly correlated with the CDM density field, as was qualitatively discussed with Figure 4.2. More quantitatively, Figure 4.3 shows the $z = 0$ cross-correlation coefficient between CDM and neutrinos from S2 as a function of wavenumber. We find that neutrinos exhibit $r_{c\nu} \gtrsim 0.9$ correlation with CDM on all scales $k < 1$ h/Mpc and achieve $r_{c\nu} \sim 0.85$ down to the smallest scales resolved in the simulation.

The halo power spectrum is also plotted in Figure 4.2. As expected, the halo power follows the general shape of the CDM power spectrum, but with a reduced amplitude, or bias. We define the bias as:

$$b \equiv \sqrt{\frac{P_{hh}}{P_{cc}}}, \tag{4.11}$$

and plot it as a function of k in Figure 4.4. Defining the bias with respect to the CDM power spectrum instead of the total matter spectrum (e.g. including neutrinos) was shown to be less scale dependent in Castorina et al. (2014). The bias is roughly constant on large scales with $b \sim 0.8$ and falls off on small scales as the halo density field does not include contributions
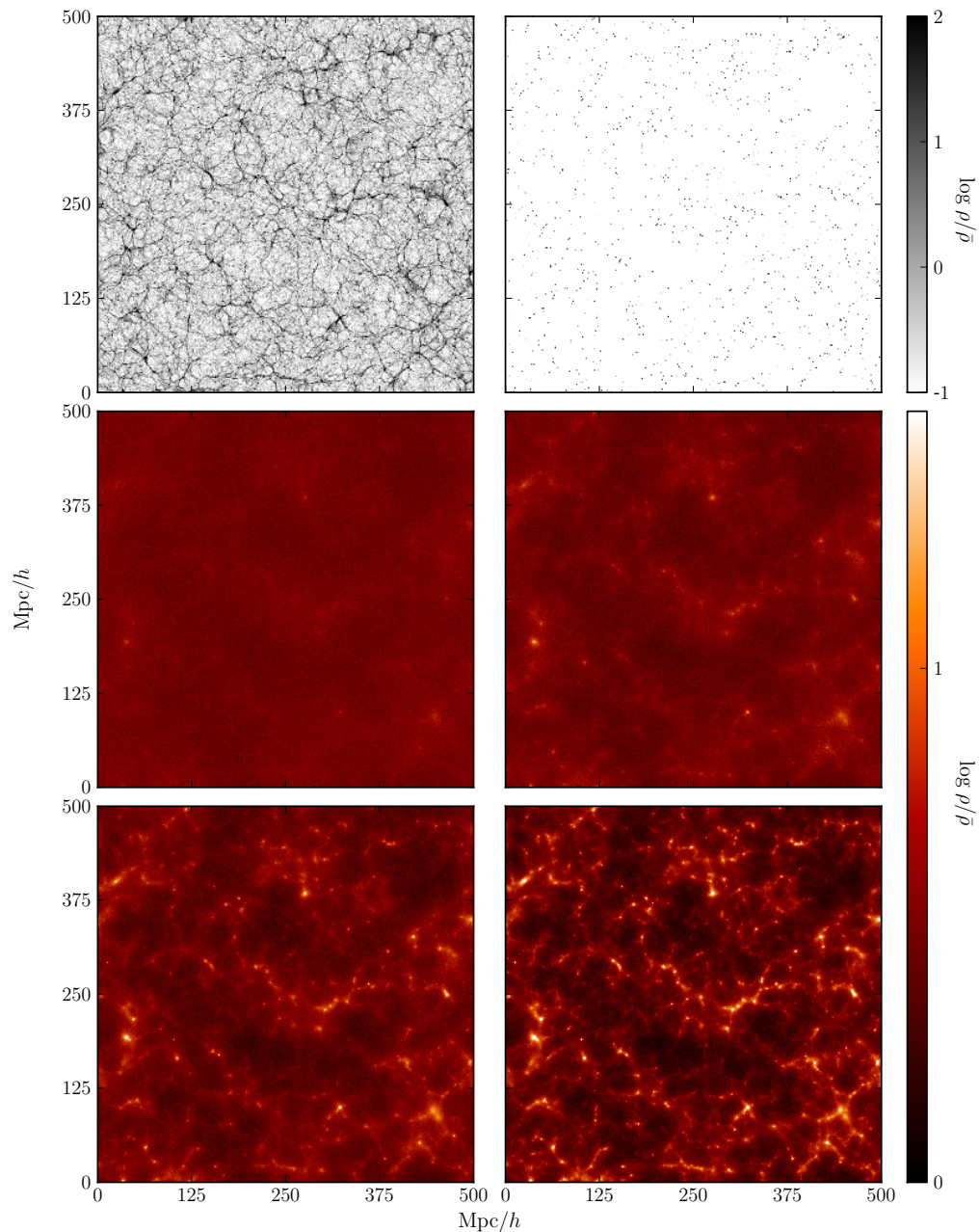
Figure 4.1: Density slices of equal width 500 Mpc/h and thickness 1.3 Mpc/h from various simulations at $z = 0$. The top row shows cold dark matter (left) and halo (right) density slices from the 0.2 eV neutrino simulation. The middle row compares neutrino density slices from the 0.05 (left) and 0.1 (right) eV simulations while the bottom row shows the 0.2 (left) and 0.4 (right) eV simulations. It is easy to see by eye that the cold dark matter and neutrino density fields are highly correlated and that heavier neutrinos cluster more than lighter ones.
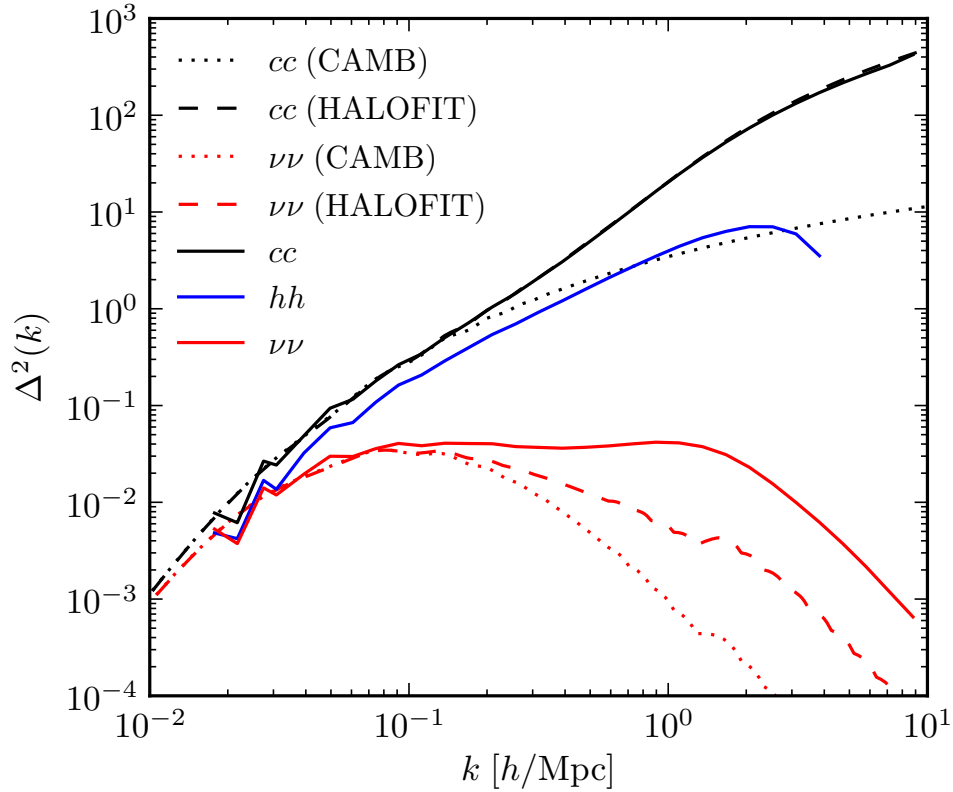
Figure 4.2: The dimensionless matter power spectra at $z = 0$ for cold dark matter (solid black line), halos (solid blue line) and neutrinos (solid red line) from S2. Shot noise has been removed by computing the cross-spectrum between two randomly chosen groups for each species. Also plotted are the linear and nonlinear cold dark matter (dotted black and dashed black lines) and neutrino (dotted red and dashed red lines) power spectra. Note that there is a small numerical artifact in the linear neutrino transfer function just above $k = 1\,h/\mathrm{Mpc}$ that should be ignored.
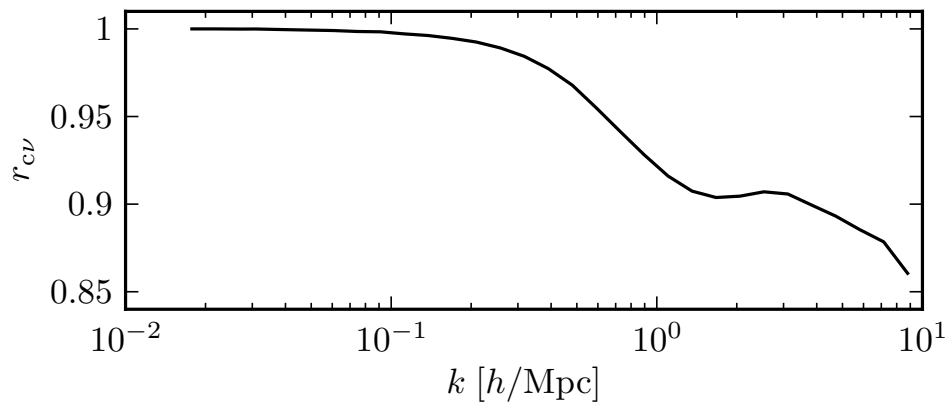

Figure 4.3: The cold dark matter-neutrino cross correlation coefficient at $z = 0$ from S2. As expected, neutrinos are highly correlated with cold dark matter over a large range of scales.
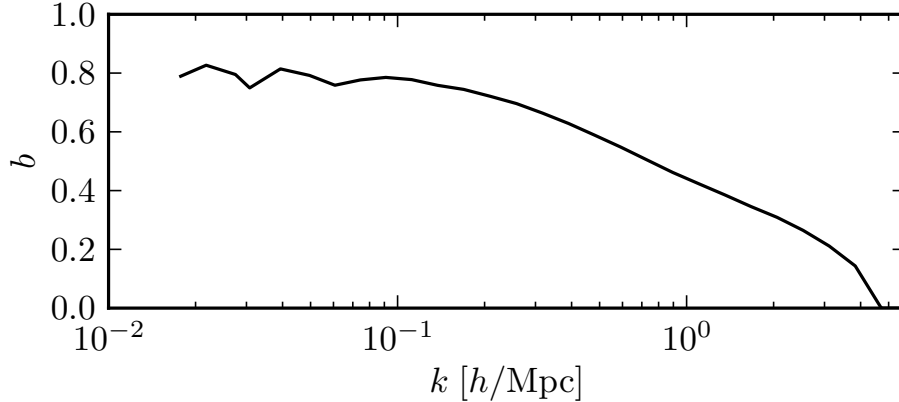
Figure 4.4: The halo bias parameter measured from S2 at $z = 0$. On scales $k \lesssim 0.2\ h/$Mpc the bias is roughly constant with $b \sim 0.8$. The bias falls off on smaller scales as power is suppressed within the typical virial radii of halos.

from the "one-halo" term describing the internal mass profile of halos (Scherrer & Bertschinger, 1991). Hence, halo power is suppressed on scales comparable to the typical virial radii of halos which occurs at $k \sim 0.2\ h/$Mpc for the largest halos in the box.

4.4.2   Velocity

Figure 4.5 compares slices of CDM, neutrino, and CDM-neutrino relative velocity computed from the simulation particles as well as reconstructed from the CDM and halo density fields using equation (4.6). We observe a similar trend as the density fields with CDM and neutrinos highly correlated in velocity. In addition, we see that the velocity fields reconstructed from only knowledge of either the CDM or halo density field qualitatively agree with the large-scale structure of the velocity fields obtained within the simulation.

Figure 4.6 compares the simulated CDM and neutrino velocity power spectra to the CDM and halo reconstructed fields. Note that for the latter we take $\delta = \delta_h/b$ in equation (4.6) to account for the halo bias. We use a value of $b = 0.80$ consistent with the large-scale bias found in Figure 4.4. We compute theoretical predictions for the velocity power using equation (4.10) with T_i being a velocity transfer function. We note that the groups method has also effectively removed shot noise from the velocity power just as for the density.

Figure 4.6 demonstrates that the simulated CDM velocity field is suppressed on scales $0.2 \lesssim k \lesssim 4.0$ h/Mpc compared to the linear and nonlinear expectations. This suppression was also seen in Pueblas & Scoccimarro (2009); Hahn et al. (2014) and may be due to the thermalization of CDM within collapsed objects. The velocity field reconstructed from CDM agrees well with the nonlinear expectation of equation (4.10). This is simply a reflection of the agreement between the CDM density field and HALOFIT shown in Figure 4.2. If we used the full bias curve, $b(k)$, instead of a constant then the halo reconstruction method works equally well. Neutrinos, on the other hand, have a velocity power spectrum that agrees well with the
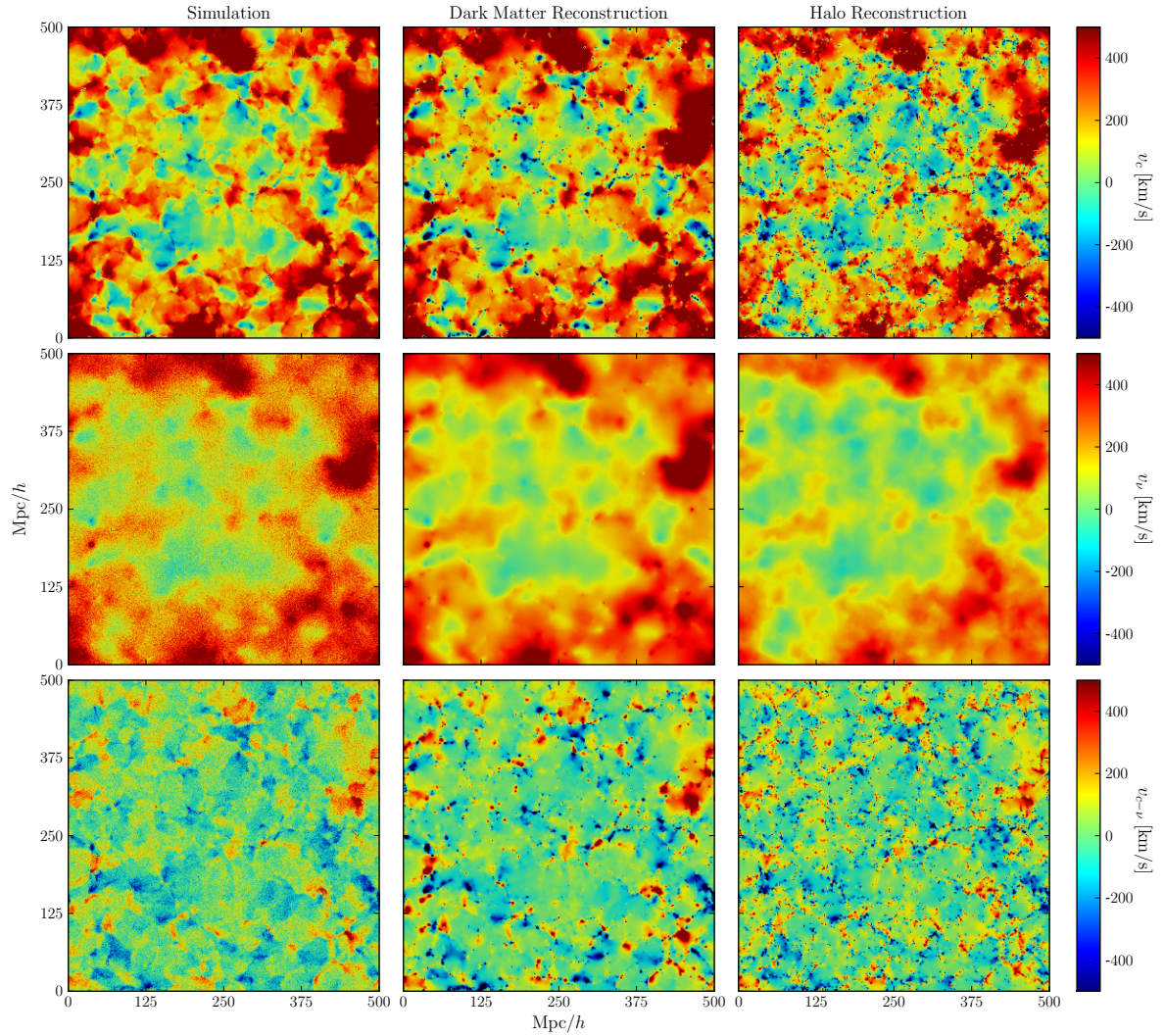
Figure 4.5: Slices of equal width 500 Mpc/h and thickness 1.3 Mpc/h showing the $z = 0$ velocity component perpendicular to the page for cold dark matter (top row), neutrinos (middle row), and the relative velocity between cold dark matter and neutrinos (bottom row). Columns show the velocity fields from the simulation particles (left column), reconstructed from the cold dark matter density field (middle column), and reconstructed from the halo density field (right column). We see that both of the reconstruction methods agree well with the large-scale structure of the simulation velocity fields.
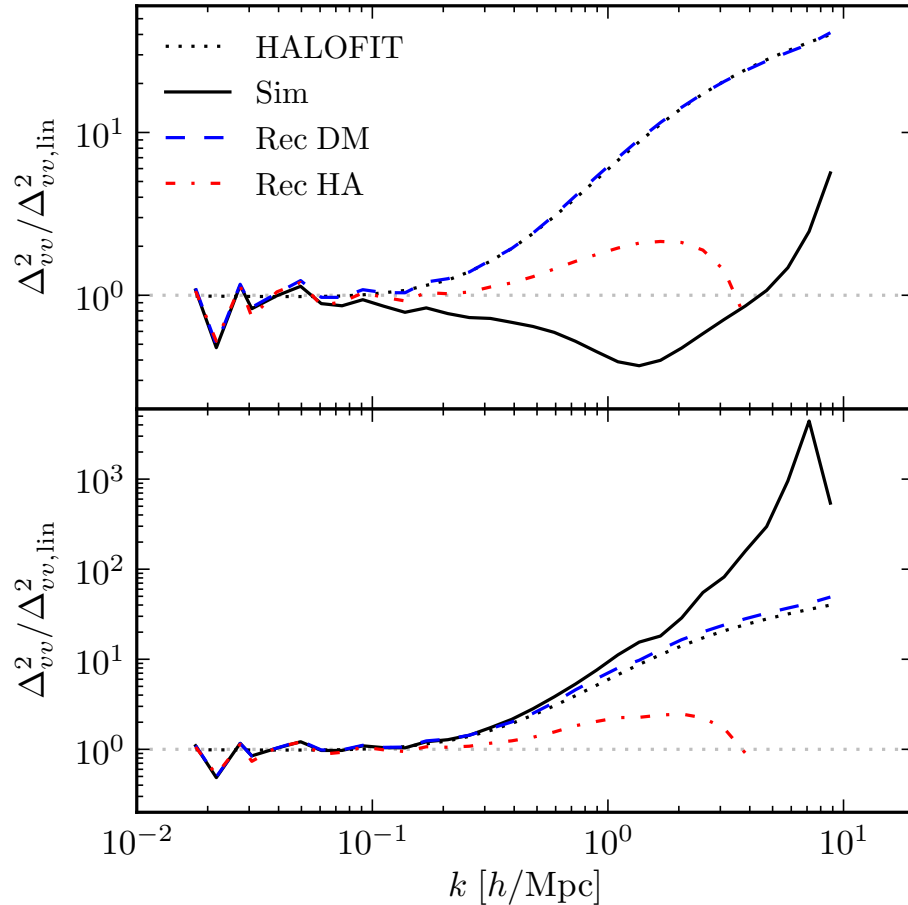
Figure 4.6: Velocity power spectra at $z = 0$ from S2 for cold dark matter (top) and neutrinos (bottom) normalized to the linear theory result obtained from equation (4.10). In each panel, the dotted black line shows the nonlinear expectation of equation (4.10), the solid black line shows the simulation result, and the dashed blue line (dot-dashed red line) shows the velocity field reconstructed from equation (4.6) using the cold dark matter (halo) density field.

nonlinear expectation on scales $k \lesssim 0.15\,\text{h/Mpc}$. However, we find that they are underpredicted by linear theory on small scales. It is unclear why neutrinos behave in an opposite manner from CDM.

The efficacy of reconstructing velocities using equation (4.6) relies on the linearity of the velocity field. To test this we decompose velocity into divergence and curl components. We have performed this computation using both real-space finite differencing of the velocity field as well as Fourier space decomposition:

$$
\begin{aligned}
\vec{v}_k &= \hat{k}(\hat{k} \cdot \vec{v}_k) + \hat{k} \times (\hat{k} \times \vec{v}_k) \\
&= \hat{k}D + \vec{C},
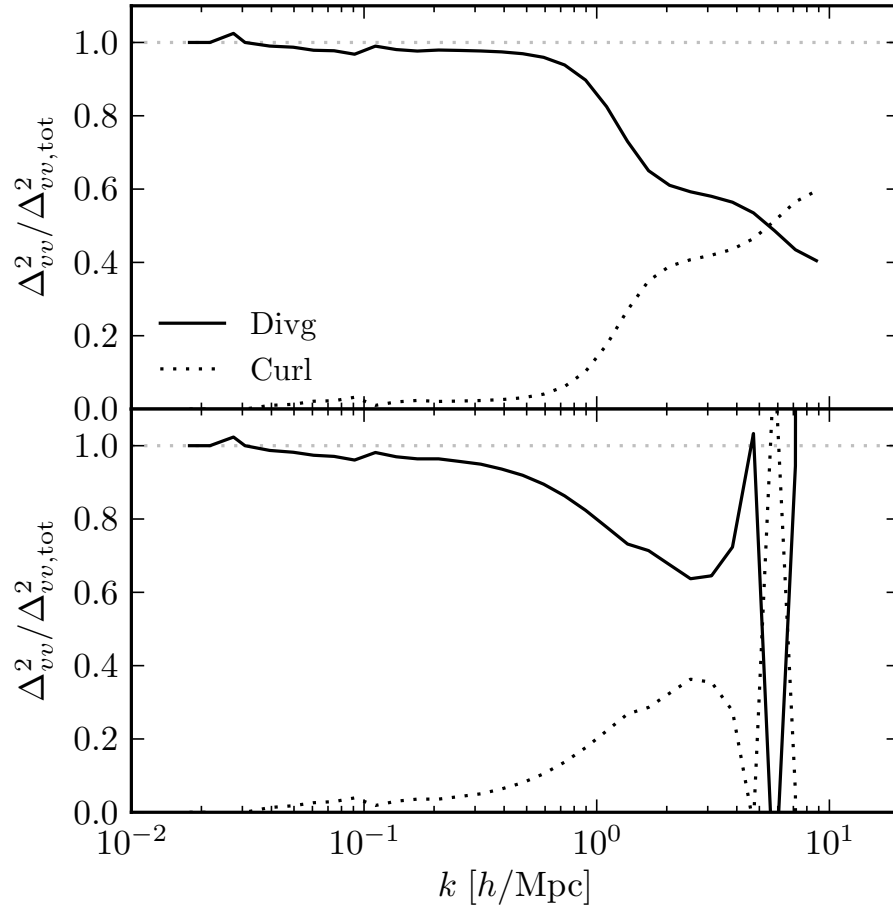\end{aligned}
\tag{4.12}
$$

Figure 4.7: Relative fraction of the divergence (solid black line) and curl (dotted black line) components of the cold dark matter (top) and neutrino (bottom) velocity power at $z = 0$ from S2. In each case, the curl component is negligible on scales $k \lesssim 1$ h/Mpc. The oscillations seen with the neutrino power on small scales is indicative of their shot noise.

where D is the divergence field and $\vec{C} = \vec{v}_k - \hat{k}D$ is the curl field. Both the real-space and Fourier-space methods produce equivalent results. In linear theory, the velocity is parallel to $\hat{k}$ and therefore has no curl. Hence, the presence of a curl component of the velocity field allows us to measure its degree of nonlinearity.

In Figure 4.7 we plot the divergence and curl components of both the CDM and neutrino velocity fields. In each case, we see that the velocity is curl-free on scales $k \lesssim 1$ h/Mpc. The only significant curl component occurs for CDM on scales $k \gtrsim 5$ h/Mpc. This result highlights that the discrepancy between the simulated CDM velocity and theoretical curves in Figure 4.6 is not due to the presence of a curl component, but rather due to nonlinear processes affecting the divergence.
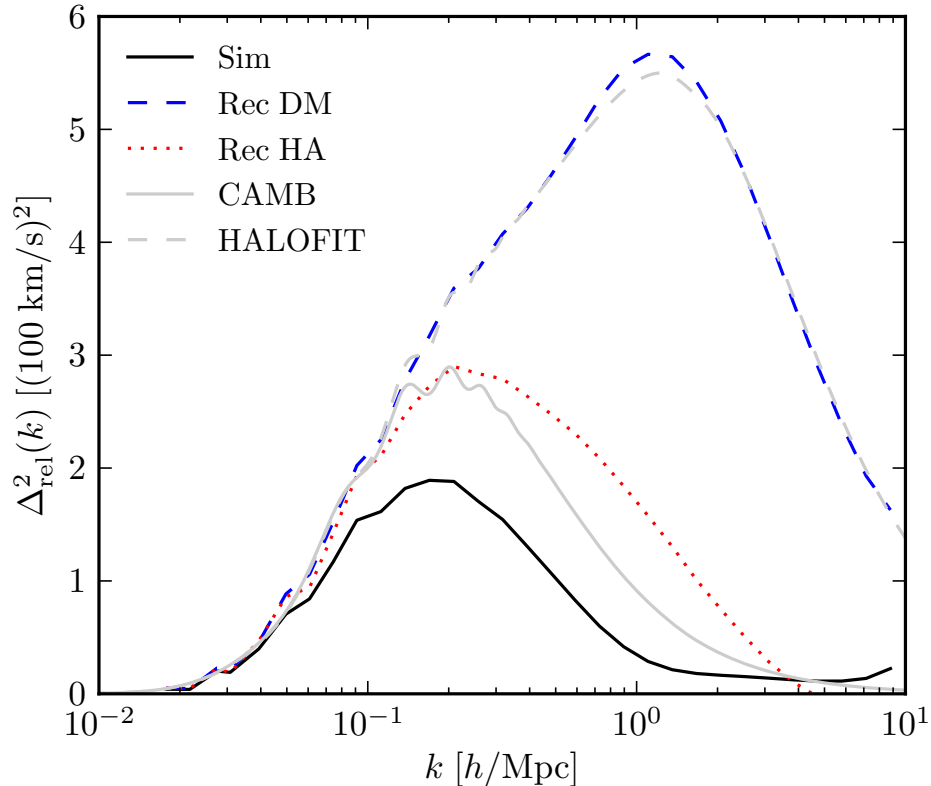
Figure 4.8: The cold dark matter-neutrino relative velocity power spectrum at $z = 0$ for S2 (black line) compared to the cold dark matter (dashed blue) and halo (dotted red) reconstructed fields as well as the linear (solid gray) and nonlinear (dashed gray) predictions. The simulated relative velocity power is similar to the linear prediction whereas the two reconstructed fields deviate from the linear curve due to nonlinear structure formation.

4.4.3   Relative Velocity

Figure 4.8 compares the CDM-neutrino relative velocity power spectrum to linear and nonlinear predictions as well as to the two reconstruction methods. The relative velocity field from the simulations is roughly similar to the linear theory expectation, being within a factor of 3 on scales $k < 5$ h/Mpc. The power spectra from the halo reconstruction method is also similar to the linear theory result. The field reconstructed from CDM looks very different from the previous two but is consistent with the nonlinear expectation. This can be made consistent with the linear theory result by simply multiplying equation (4.6) by the ratio between the linear and nonlinear CDM density power spectra.

Figure 4.9 shows the correlation coefficient defined in equation (4.7) between the simulated and reconstructed relative velocity fields. We see that both reconstruction methods reproduce the relative velocity field well over the scales of interest. In particular, the halo reconstruction achieves nearly perfect correlation on scales $k \lesssim 1$ h/Mpc. The velocity correlation coefficient is a measure of how well the vector fields agree in direction as the denominator in equation (4.7)
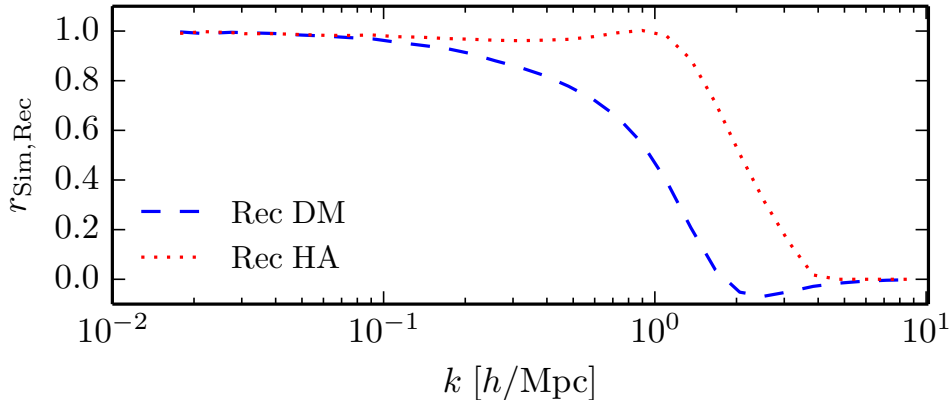
Figure 4.9: The cold dark matter-neutrino relative velocity correlation coefficient between the simulated field and the field reconstructed from cold dark matter (solid black line) and halo (dashed blue line) density fields. Both methods are highly correlated over all relevant scales.

divides out the magnitudes. Thus, Figure (4.9) demonstrates that we are able to reconstruct the direction of the relative velocity field accurately.

Figure 4.10 shows the relative velocity power spectra for each of the four neutrino masses using the nearest particle/momentum method. We find that they follow the same trends: lighter neutrinos have less relative velocity and the linear prediction is larger than in simulation. Table 4.1 lists the integrated correlation coefficients as a function of neutrino mass between simulated and halo reconstructed velocities for CDM, neutrino and CDM-neutrino relative velocities. We find that there is a large correlation between these methods indicating that the reconstruction method is accurately reproducing the simulation velocities.

Finally, in Figure 4.11 we show the relative velocity correlation lengths, $\xi_{1/2}$, defined as in Zhu et al. (2014b) to be the point at which the relative velocity correlation function,

$$\xi_{\nu c}(r) = \int \frac{dk}{k} \Delta_{\nu c}^2 \frac{\sin(kr)}{kr} \tag{4.13}$$

reaches half its maximum value. This scale can be thought of as the size of a region with a uniform velocity field. Lighter neutrinos are less affected by large scale structure due to their larger thermal velocities and so are coherent over larger regions. Figure 4.11 shows these

Table 4.1: The integrated correlation coefficient defined in equation (4.8) between the simulated velocities and those reconstructed by halos for cold dark matter, neutrinos and cold dark matter-neutrino relative velocities.

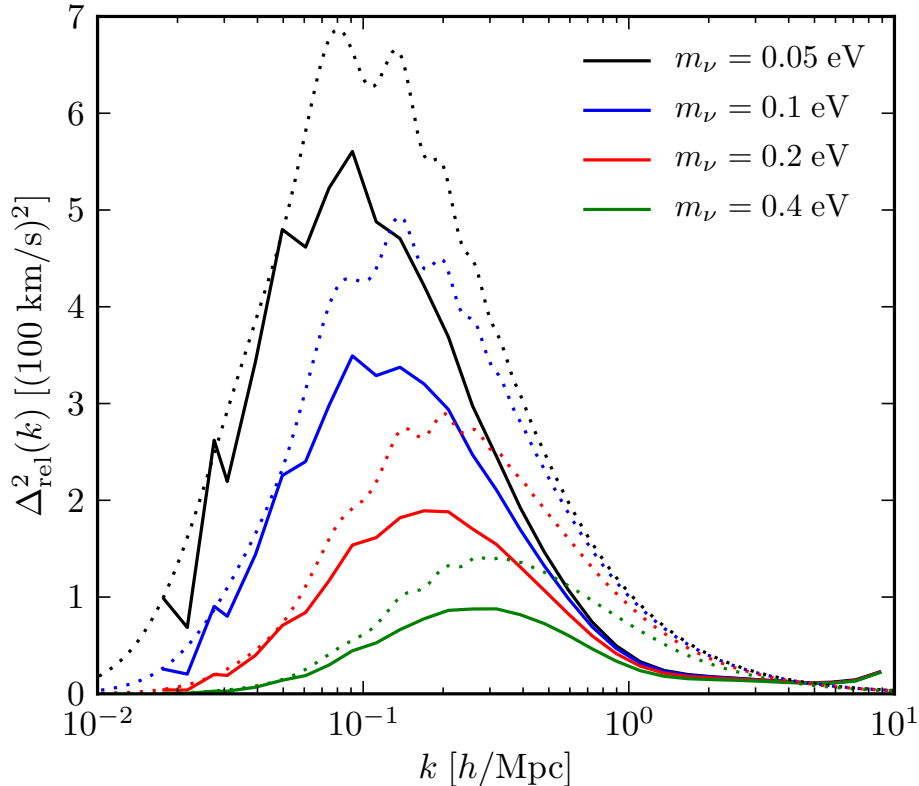| m_ν	Cold Dark Matter	Neutrinos	Relative
0.05	0.95	0.98	0.94
0.1	0.95	0.97	0.93
0.2	0.95	0.97	0.92
0.4	0.95	0.97	0.88

Figure 4.10: The cold dark matter-neutrino relative velocity power spectra via the nearest particle/momentum method for all four neutrino masses (solid) along with theoretical predictions (dashed). The power is clearly suppressed compared to linear theory but behaves qualitatively similar with varying masses.

correlation lengths as a function of neutrino mass. We find that the simulations exhibit a slightly larger correlation length for each neutrino mass compared to the theoretical predictions. The shapes of the curves remain similar, however, with both having power law slope which we fit to have an exponent -0.44.

4.5   Discussion

We have tested four methods of computing the velocity field: a nearest particle method, a momentum method, and reconstruction via CDM and halo density fields. Our results are generally consistent with theoretical expectations and highly correlated among each other. Specifically we have demonstrated that reconstructing the velocity from point-particle halos produces a velocity field highly correlated with that of our N-body particles. It is the near unit correlation coefficient - a measure of the angle between the two fields - that ensures that the reconstructed velocity points in the right direction. The magnitude of the velocity can then simply be scaled to the correct value as long as the bias is known.
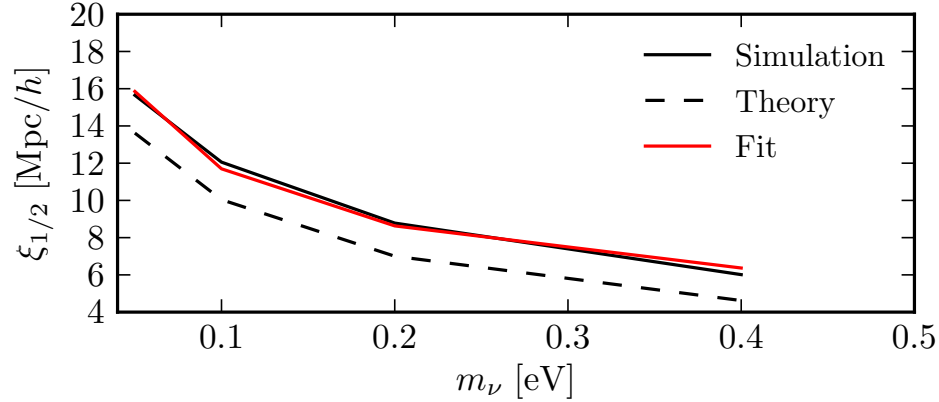
Figure 4.11: The correlation length defined to be the distance for which the correlation function in equation (4.13) drops to half its maximum value for varying neutrino masses. The simulations have longer correlation lengths but follow a similar power law behaviour.

This result allows for a prescription to determine the actual velocity fields in our own Universe.

1. Reconstruct the galaxy density field from a galaxy survey catalogue. We expect this reconstruction to be very comparable to the halo reconstruction we use here except with the addition of a 1-halo term to make the bias constant over more wavenumbers.

2. Fourier transform the gridded density field. Then, use equation (4.6) to compute the CDM, neutrino and relative velocity fields in Fourier space. Here, a nonlinear correction can be applied by additionally multiplying by a factor of $\Delta_v^{\mathrm{Sim}}/\Delta_v^{\mathrm{RecHA}}$.

3. Fourier transform back to real space.

We first note that a similar process could be performed on the density fields produced by 21 cm observations. We also note that redshift distortions and masking effects might result in extra biases in the reconstruction scheme. We intend to investigate these effects in a future paper.

Our results also provide support for the applicability of the analysis performed in Zhu et al. (2014a,b). They used moving background perturbation theory to study the neutrino relative velocity effect. The moving background approximation relies on having a coherent background relative flow and our simulation results indicate that the coherency scales of such motions are larger than predicted. Thus, we expect that inaccuracies in the predicted dipole distortion to the correlation function will come from nonlinear evolution rather than the moving background approximation. We note that we can also directly measure the dipole correlation function in our simulations and plan to report on this in a subsequent paper.

4.6   Conclusion

We performed a set of four large N-body simulations including cold dark matter and neutrinos of varying mass. We have accurately measured the cold dark matter-neutrino relative velocity. We find that we can accurately reconstruct this velocity using a linear theory approach and halo density fields. We have described a simple method for accurately predicting the relative velocity field via a galaxy survey or 21 cm observations. Since such a reconstruction allows for an independent measurement of neutrino masses, we expect this technique to provide significant constraints in upcoming astronomical surveys.

Acknowledgements

Chapter 5

TianNu: simulating the neutrino sky

This chapter presents preliminary results from a research project that we plan to soon submit for publication as "TianNu: simulating the neutrino sky" Yu, H.-R., Emberson, J.D., Inman, D., Zhang, T.-J., Pen, U.-L., Harnois-Déraps, J., Yuan, S., Zhu, H.-M., Chen, X., Teng, H.-Y., Xing, Z.-Z.

5.1   Chapter Overview

Constraining the absolute neutrino mass hierarchy remains one of the most elusive challenges of modern science. Neutrino oscillation experiments confirm the existence of at least two massive neutrino species, but only place lower bounds on their mass. Cosmological experiments, on the other hand, have so far been only able to place upper bounds on the total sum of neutrino mass. The existence of massive neutrinos requires physics beyond the standard model and determining individual neutrino mass would shed light on the mysterious nature of these particles. In this work, we study new cosmological neutrino detection methods using a pair of high-resolution N-body simulations; one with massive neutrinos and one without. The neutrino simulation, named "TianNu" or the "Neutrino Sky", is currently the world's largest N-body simulation containing 6912^3 cold dark matter (CDM) particles and 13824^3 neutrino particles. The neutrino-less simulation, named "TianCold" or the "Cold Sky", contains 6912^3 CDM particles. We present here preliminary results from our analysis of TianCold and TianNu. These include detailed measurements of the matter power suppression on small scales caused by neutrino free-streaming as well as an assessment of the dipole distortion in the matter density field induced by the relative flow of CDM and neutrinos. By comparing TianCold and TianNu on a halo-by-halo basis, we obtain a measure of neutrino bias, and propose a new method of searching for neutrinos in galaxy surveys. This method measures the *difference* between neutrinos and the rest of matter, making it potentially easier to observe compared to standard cosmological approaches (e.g., matter power spectrum) that measure the *sum* of neutrinos with the rest of matter.

5.2 Introduction

The conjecture of massless neutrinos has been convincingly disproved by the observation of neutrino flavour oscillations in a multitude of solar, atmospheric, accelerator, and reactor experiments (see Wang & Xing, 2015). These observations imply that at least two of the three neutrino species are massive, with minimum masses of roughly 0.009 and 0.05 eV (Fogli et al., 2012). Unfortunately, oscillation experiments are only sensitive to the mass-squared splittings between mass eigenstates and cannot be used to infer the hierarchy of individual neutrino masses. This leaves many open questions into the nature of these fundamental particles.

To this end, particle physicists have devised a number of methods to constrain the absolute neutrino mass scale with exquisite precision. Experiments such as GERDA (Agostini et al., 2013) and EXO-200 (The Exo-200 Collaboration et al., 2014) attempt to observe neutrinoless double-β decay ($0\nu\beta\beta$), a process through which an atomic nucleus decays with the emission of two electrons and nothing else. If observed, this process implies that neutrinos are Majorana particles (i.e., they are their own anti-particle) and may also place constraints on the absolute mass scale. At present, this observation has proven difficult and no statistically significant evidence for $0\nu\beta\beta$ has been found. Another method of measuring neutrino mass comes from observations of the energy spectrum of emitted electrons from the β decay of tritium: ${}^{3}_{1}\mathrm{H} \rightarrow{}^{3}_{2}\mathrm{He} + \mathrm{e}^- + \bar{\nu}_e$. Current constraints from tritium experiments place an upper limit on the mass of the electron neutrino at $m_{\nu_e} \leq 2.3$ eV (Kraus et al., 2005) while the upcoming KATRIN experiment is expected to reduce this bound to the level of ~ 0.35 eV (Eitel, 2005).

Cosmologists have also been working hard to constrain the neutrino mass scale. Relic neutrinos produced during the early universe have the potential to impact cosmological phenomena including big bang nucleosynthesis, the cosmic microwave background, and large-scale structure. Currently, the best constraint comes from the Plank satellite, which places an upper bound on the sum of neutrino mass at $\sum m_\nu < 0.194$ eV (Planck Collaboration et al., 2015). At least two of the three neutrino species are massive enough to be relativistic today since the neutrino temperature, $T_\nu \approx 10^{-4}$ eV, is much smaller than the minimum masses of 9 and 50 meV derived from oscillation experiments. Non-relativistic neutrinos contribute to the matter density of the universe and act as a hot dark matter (HDM) component that smooths structure formation on small scales. Future galaxy surveys such as Euclid (Amendola et al., 2013) and LSST (LSST Dark Energy Science Collaboration, 2012) will measure the matter power spectrum with extreme precision and are expected to reduce the cosmological bounds on the sum of neutrino mass to the ~ 0.04 eV scale (Costanzi Alunno Cerbolini et al., 2013).

Current and future cosmological observations have thus far been sensitive to only the *sum* of neutrino mass. Furthermore, constraints from matter power spectrum observations are hindered by the complicated details of unknown baryonic physics that can also suppress structure formation on small scales. Zhu et al. (2014b) recently proposed a cosmological observation that circumvents both of these issues. The idea is based on the relative flow between CDM and neutrinos that establishes a local dipole asymmetry in the matter density field. This dipole is

a unique feature of neutrinos and has the potential of being observed by galaxy-galaxy cross-correlations, weak lensing surveys, and future 21 cm observations (Zhu et al., 2014a). The dipole distortion is sensitive to individual mass so that the total signal can be deconstructed to provide constraints on the neutrino mass hierarchy. Moreover, the scale on which this dipole operates (~ 10 Mpc) is too large to be affected by baryonic physics. The only information required to search for the signal is knowledge of the direction vector of the relative CDM-neutrino velocity. Inman et al. (2015) used N-body simulations to show that this can be accurately reconstructed by applying linear transformations to an observed galaxy survey.

In this Chapter, we explore the neutrino dipole distortion as well as a new method of potentially observing neutrinos based on their impact on the clustering of CDM halos. In §5.3 we discuss the two N-body simulations used in this work. In §5.4 we present preliminary results from our analysis of the simulation data. We finish in §5.5 with a brief summary.

5.3 Numerical Simulations

Our aim is to make accurate predictions of the impact of neutrinos on cosmological observations within the nonlinear regime. We therefore require the use of numerical simulations that trace the nonlinear evolution of both CDM and neutrino particles. In this work, we adopt the technique described in Inman et al. (2015) for simulating both species in cosmological N-body simulations. We provide a brief summary of this algorithm and point the reader to Inman et al. (2015) for technical details.

The N-body simulations are performed using the cosmology code CUBEP³M (Harnois-Déraps et al., 2013) modified to contain neutrino particles. CDM initial conditions are generated at $z = 100$ using the Zel'dovich approximation (Zel'dovich, 1970). At this redshift, neutrinos are still relativistic, demanding a prohibitively slow time step to trace their dynamics. We avoid this issue, we first evolve CDM particles in isolation from $z = 100$ to $z = 5$. Adiabatic initial conditions for neutrino particles are generated at $z = 5$ using the same Gaussian random noise map as the CDM. Neutrino velocities are given both a traditional linear term and a random thermal component. The latter is drawn from the relativistic Fermi-Dirac distribution and is applied in a random direction. CDM and neutrino particles evolve together from $z = 5$ to $z = 0$, interacting through particle-particle-particle-mesh (P³M) gravitational forces.

We simulate a box size of width $L = 1200$ Mpc/h and focus on a single neutrino of mass $m_\nu = 0.05$ eV. The box size was chosen to have a similar volume as an all-sky survey out to $z \approx 0.2$. The neutrino mass was chosen as the minimum mass of the most massive neutrino from oscillation constraints (Fogli et al., 2012) in order to test minimum observability prospects. We choose a cosmology consistent with the Planck (Planck Collaboration et al., 2015) results: $(\Omega_b, \Omega_c, \sigma_8, n_s, h) = (0.05, 0.27, 0.83, 0.96, 0.67)$. Neutrinos contribute an additional energy fraction (Mangano et al., 2005):

$$\Omega_\nu = \frac{m_\nu}{93.14h^2 \text{ eV}}, \tag{5.1}$$

and the dark energy fraction is chosen to satisfy $\Omega_\Lambda = 1 - \Omega_m$ where $\Omega_m = \Omega_b + \Omega_c + \Omega_\nu$ is the sum of baryons, CDM, and neutrinos.

We perform two simulations for cosmologies with and without the presence of neutrinos. The first simulation, named "TianCold" (the "Cold Sky"), contains 6912^3 CDM particles that evolved in isolation from $z = 100$ to $z = 0$. The second simulation, named "TianNu" (the "Neutrino Sky"), started with the $z = 5$ CDM distribution from TianCold and added 13824^3 neutrino particles, which evolved alongside CDM to $z = 0$. The two simulations differ by the influence of massive neutrinos between redshifts 5 and 0. Both simulations were performed using 86% (331,776 cores) of the Chinese supercomputer Tianhe-2.

TianNu contains a total of 2.97×10^{12} particles making this the world's largest cosmological N-body simulation to date. The large number of neutrino particles is necessary to suppress shot noise on small scales due to the thermal motion of the hot neutrinos. The particle masses are $4.7 \times 10^8 \ M_\odot/h$ and $9.8 \times 10^4 \ M_\odot/h^3$ for CDM and neutrinos, respectively. Gravitational forces are smoothed below a softening length of 13 kpc/h. CDM halos are identified in CUBEP^{3}M using a spherical overdensity algorithm that considers all halos with at least 500 particles ($2.3 \times 10^{11} \ M_\odot/h$) within the virial radius. The virial radius is defined such that the enclosed density is 200 times the mean matter density of the universe.

5.4 Preliminary Results

5.4.1 Matter Power Suppression

We begin in Figure 5.1 with slices of the CDM and neutrino density fields from TianNu at $z = 0$. Neutrinos clearly cluster around the largest CDM structures in the cosmic web, but have significantly suppressed clumping on small scales. The fluctuations in neutrino density, being only a factor of a few in this image, are also much suppressed compared to that of CDM, where the density in collapsed objects easily exceeds the mean density by orders of magnitude. The zoom-in region in the right panel shows that neutrinos still exhibit noticeable shot noise on the smallest scales of the simulation. This highlights the importance of using a large number of neutrino particles to sufficiently sample the simulated volume.

We study this picture more quantitatively in the top panel of Figure 5.2 where the density power spectra of CDM and neutrinos from TianNu are shown at $z = 0$. Power spectra are obtained by interpolating each species to a 6912^3 mesh using the nearest grid point scheme. The solid blue and red curves in Figure 5.2 confirm the trends noticed visually in Figure 5.1. The neutrino power approaches that of CDM on large scales, $k \lesssim 10^{-2} \ h/$Mpc, where both agree well with linear theory. On small scales, neutrino power is increasingly suppressed due to free-streaming. These results are consistent with our findings presented in Inman et al. (2015).

The solid blue line in the bottom panel of Figure 5.2 shows the ratio, $P_{mm}^{\mathrm{TN}}/P_{mm}^{\mathrm{TC}}$, between the total matter power spectrum of TianNu and TianCold. Hot neutrinos lead to a suppression in the matter power spectrum of TianNu on all scales probed here. The upturn at $k \gtrsim 1$
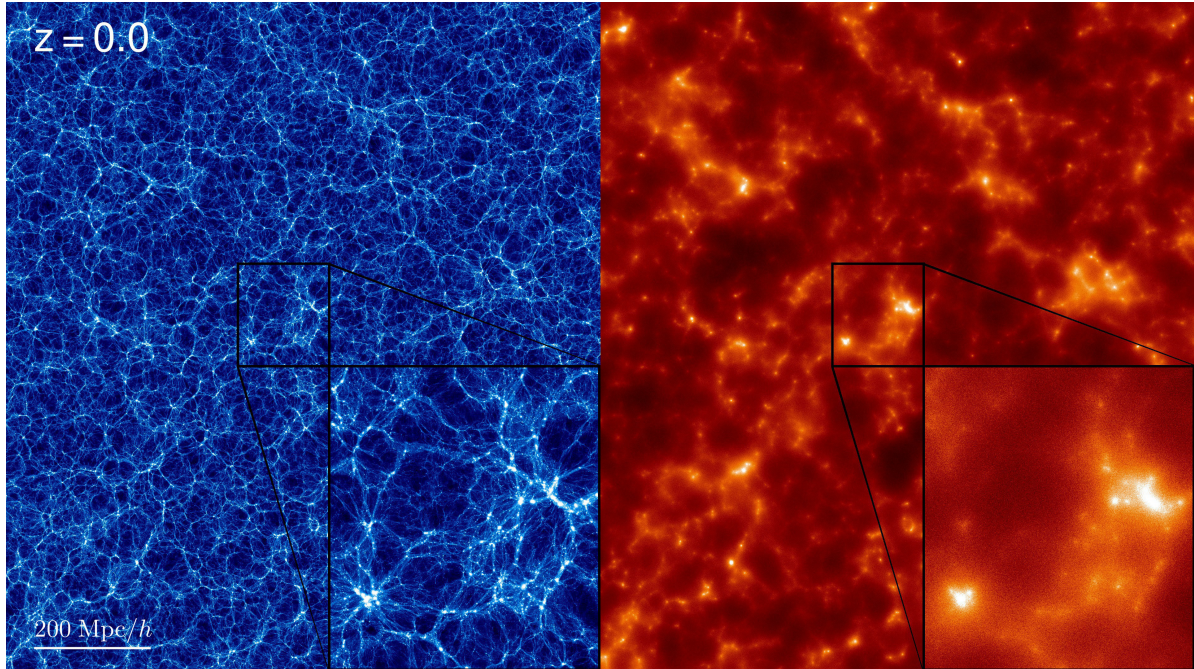
Figure 5.1: Slices of the CDM (on the left, in blue) and neutrino (on the right, in red) density fields at $z = 0$ from the TianNu simulation. Each slice is 1000×1125 Mpc/h on a side and has a depth of 8 Mpc/h. The inset on the bottom-right of each slice shows a closeup on a region 150×170 Mpc/h on a side. The slices are coloured according to the logarithm of the projected density. The colour map of CDM (neutrinos) spans 3.5 (0.3) decades in log density.

h/Mpc is due to small-scale structure that has had sufficient time since collapse for nonlinear CDM dynamics to drive the evolution into closer agreement with TianCold (see also Brandbyge et al., 2008; Viel et al., 2010; Bird et al., 2012; Massara et al., 2014). Though small, the total suppression seen here has observational ramifications, being potentially observable in upcoming galaxy surveys such as Euclid and LSST. Recall that $m_\nu = 0.05$ eV is situated at the lower bound of neutrino mass, so the effect seen here can be viewed as the minimum suppression made by massive neutrinos. The large dynamic range of TianNu offers the most accurate prediction to date of the level of matter power suppression induced by 0.05 eV neutrinos.

Recently, Bird et al. (2012) updated HALOFIT (Smith et al., 2003) to allow for predictions of the nonlinear matter power spectrum in massive neutrino cosmologies. However, the simulations used by Bird et al. (2012) for this calibration were focused more on $m_\nu \sim 0.3$ eV neutrinos. Due to the present lack of fully nonlinear $m_\nu = 0.05$ eV simulations, it remains to be seen how well the new HALOFIT modifications fare in the low mass regime. We are currently in the process of comparing our results to those expected from the Bird et al. calibration. Unfortunately, this is somewhat complicated due to the nature in which the neutrinos were turned on at $z = 5$ in TianNu. We are thus working to disentangle this effective two-stage cosmology in order to make a fair comparison with HALOFIT.
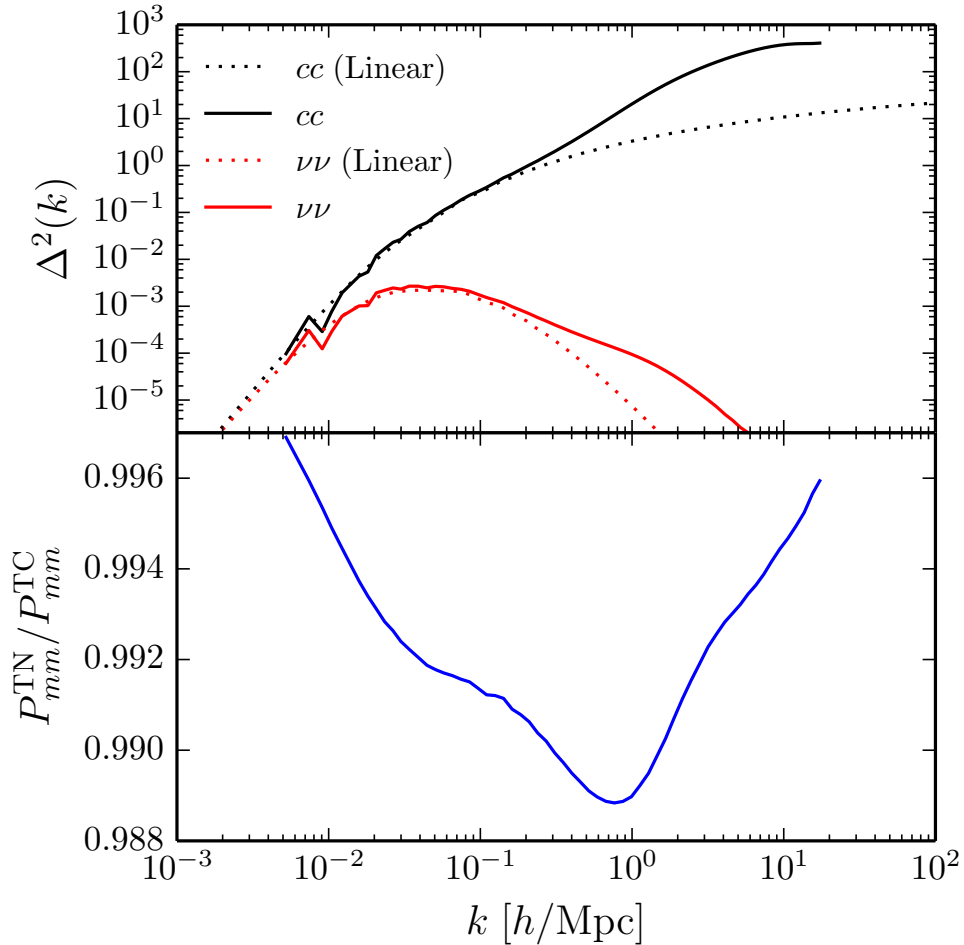
Figure 5.2: (top) Dimensionless density power spectra measured at $z = 0$ for CDM (solid black line) and neutrinos (solid red line) from TianNu. Dotted lines show the corresponding linear theory predictions for CDM (black) and neutrinos (red). (bottom) The ratio between the total matter power spectra, P_{mm}^{TN} and P_{mm}^{TC}, measured in TianNu and TianCold, respectively.

5.4.2 Dipole Distortion in Galaxy Cross-Correlation Functions

The relative flow between CDM and neutrinos establishes a unique dipole distortion in the matter density field. This can be imagined by considering a coherent flow of neutrinos becoming gravitationally focused into a high density wake downstream from a massive CDM halo. This dipole asymmetry can be measured in the CDM-neutrino cross-correlation function:

$$\xi_{c\nu 1}(r) = \langle \delta_c(\mathbf{x}) \delta_\nu(\mathbf{x} + \mathbf{r}) \mu \rangle, \tag{5.2}$$

where δ_c and δ_ν are the density contrasts of CDM and neutrinos, respectively, and $\mu \equiv \hat{\mathbf{r}} \cdot \hat{\mathbf{v}}_{c\nu}$ with $\mathbf{v}_{c\nu}$ the CDM-neutrino relative velocity. The angle brackets in equation (5.2) represent averages over spatial coordinate $\mathbf{x}$ and radial separation $\mathbf{r}$.

The dipole distortion given above was first presented in Zhu et al. (2014b) where predictions
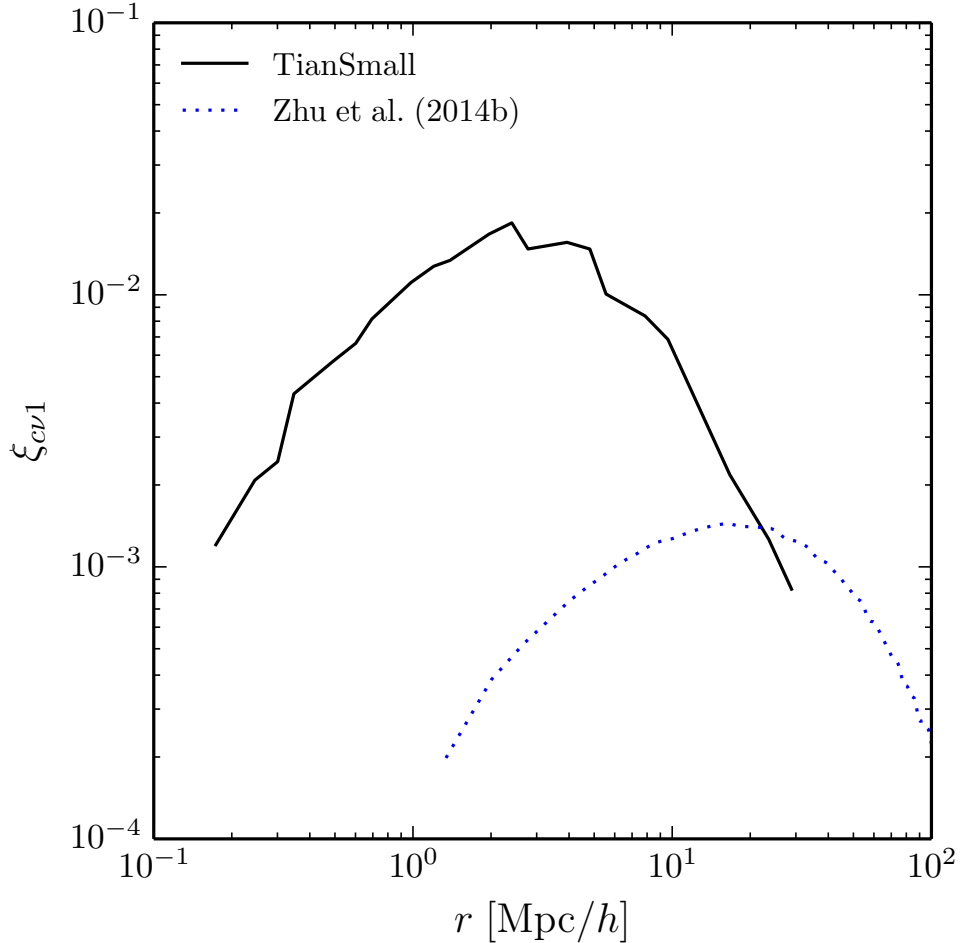
Figure 5.3: The dipole component of the CDM-neutrino cross-correlation function as obtained from TianSmall (solid black line) and as predicted from the moving background perturbation theory calculations of Zhu et al. (2014b) (dotted black line).

of its form were made using moving background perturbation theory (MBPT). We reproduce their prediction here as the dotted blue line in Figure 5.3. We are currently in the process of measuring $\xi_{c\nu1}$ directly from the simulation particles in TianNu. For testing purposes, we have performed a scaled-down version of TianNu, named TianSmall, containing 576^3 CDM plus 1152^3 neutrino particles in a box of side length 100 Mpc/h. The dipole signal measured from TianSmall is shown as the solid black line in Figure 5.3. For this calculation, CDM and neutrino particles are interpolated onto a 576^3 mesh and $\xi_{c\nu1}$ is averaged over pairs of cells. The relative velocity in equation (5.2) is taken to be the mean value of $\mathbf{v}_{c\nu}$ over a given pair of cells. Velocities for CDM and neutrinos are computed at each mesh cell using the procedure outlined in Inman et al. (2015). The two curves in Figure 5.3 show a significant discrepancy between the MBPT prediction and that found in TianSmall. Evidently, nonlinear structure formation induces an appreciable boost on small scales and shifts the peak of $\xi_{c\nu1}$ to lower values. However, as described below, this signal may also be influenced by a nonlinear dipole

term found in the CDM density field. In either event, the comparison will be made more illuminating once the signal is computed from TianNu as the small volume of TianSmall limits its ability to probe larger scales.

In practice, the application of equation (5.2) is of limited use since neither δ_c nor δ_ν can be observed directly. We must therefore rely on indirect means to measure the CDM-neutrino dipole distortion. One possibility is to uncover the dipole from the cross-correlation of two galaxy populations of differing mass (Zhu et al., 2014b). To see this, we first write the halo[1] density field, δ_h, as the sum

$$\delta_h = b_c f_c \delta_c + b_\nu f_\nu \delta_\nu, \tag{5.3}$$

where f_i is the relative fraction contributed by species i to the matter density (i.e., $f_i = \Omega_i/\Omega_m$) and b_i is the halo bias with respect to component i. Suppose we limit ourselves to halos of mass $\sim 10^{12} - 10^{13}\ M_\odot$. In this range, we expect b_ν to be independent of mass since these halos are below the free-streaming scale of neutrinos. For simplicity, we take $b_\nu = 1$ in what follows though our conclusion is unchanged as long as b_ν is constant. If we consider two halo populations, labelled δ_α and δ_β, their cross-correlation follows from equation (5.3):

$$\xi_{\alpha\beta} = \langle \delta_\alpha \delta_\beta \rangle = b_\alpha b_\beta f_c^2 \xi_{cc} + (b_\alpha + b_\beta) f_c f_\nu \xi_{c\nu} + f_\nu^2 \xi_{\nu\nu}, \tag{5.4}$$

where b_α and b_β represent the CDM bias for halo population α and β, respectively. The dipole component in $\xi_{c\nu}$, given by equation (5.2), will also manifest in $\xi_{\alpha\beta}$. In particular, $\xi_{\alpha\beta}$ has a dipole component, $\mu(b_\alpha - b_\beta) f_c f_\nu \xi_{c\nu 1}$, that is observable provided that $b_\alpha \neq b_\beta$. It is well known that bias is a generally increasing function of halo mass (e.g., Cooray & Sheth, 2002). If we take the populations α and β to represent populations of different mass, M_α and M_β, then their cross-correlation contains a dipole term proportional to the relative bias, $b(M_\alpha) - b(M_\beta)$.

We are currently working at computing the dipole component of the cross-correlation function of two halo populations of differing mass in TianNu. For this calculation, the relative velocity vector is reconstructed by applying linear transformations to the total halo density field, as outlined in Inman et al. (2015). This represents the observational pipeline for measuring the dipole signal. However, based on our analysis, it seems that this process may be more complicated than originally thought. Interestingly, there appears to be an additional dipole coming from the halo density fields themselves and overwhelming the neutrino signal. This additional dipole is found in both TianNu and TianCold, indicating that it is unrelated to neutrinos and instead due to some difference in the clustering of low- and high-mass halos. If real, this signal should be easily observable in current galaxy surveys, and may serve as a predictive indicator of halo mass. For now, it presents a burden to uncovering the neutrino signal, which we are currently working to solve.

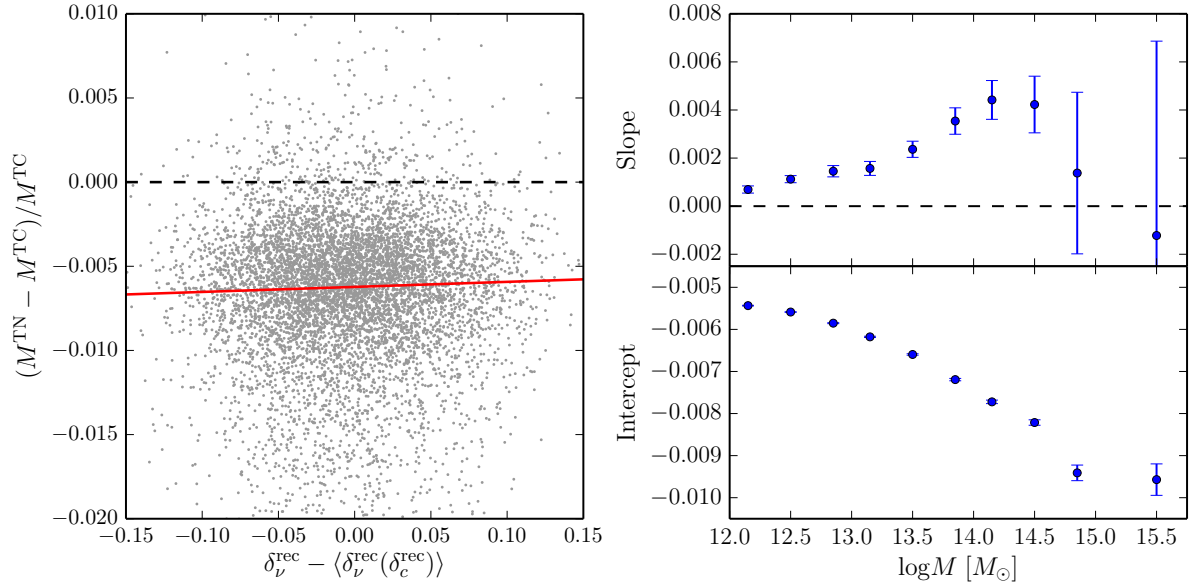[1]We assume here that halos can be used in place of galaxies.

Figure 5.4: (left) We plot the mass difference between counterpart halos in TianNu (with mass M^{TN}) and TianCold (with mass M^{TC}). The x axis represents the relative deviation of $\delta_\nu^{\mathrm{rec}}$ away from its expected value based on the local value of δ_c^{rec}. Here $\langle \delta_\nu^{\mathrm{rec}}(\delta_c^{\mathrm{rec}}) \rangle$ is obtained by fitting a linear relation $\delta_\nu^{\mathrm{rec}} = A\delta_c^{\mathrm{rec}} + B$. The scatter points show a subset of 8000 halos from the total 62,812 halos with TianCold mass between 10^{14} and 2×10^{14} $M_\odot$. The red line shows a best-fit linear relationship for all counterpart halos in this mass bin. (right) The slope and intercept of the best-fit linear relationship for different mass bins is plotted. Points denote the median value from 1000 bootstrap realizations of each mass bin and error bars show the corresponding 1σ scatter.

5.4.3   Neutrino Bias

In this section, we propose a new method of detecting neutrinos within galaxy surveys. This method is based on the change in halo clustering, or bias, induced by the presence of massive neutrinos. We study this effect by comparing halo catalogues between TianCold and TianNu. We exploit the fact that TianCold and TianNu have the same CDM initial conditions meaning that differences in their evolved state directly reveal the impact of neutrinos on halo clustering. Our procedure is as follows. For each halo in TianCold, we search for a "counterpart halo" in TianNu representing the same physical object evolved in the alternate cosmology. More precisely, we say that a halo in TianNu is the counterpart of a halo in TianCold if the two halos are no further separated than 100 kpc/h on the simulation grid and their masses are within 10% of each other. With this definition, we find that 98% (27 million) of halos in TianCold can be associated with a counterpart halo in TianNu.

For each pair of counterpart halos we calculate two quantities: δ_c^{rec} and $\delta_\nu^{\mathrm{rec}}$. These are the linearly reconstructed CDM and neutrino density contrasts, computed in a spherical region of radius 6.25 Mpc/h centred on the halo in TianCold. We reconstruct CDM and neutrino density fields by applying linear transformations to the total TianCold halo density field, as done in Inman et al. (2015). We do this so that the following discussion may be expressed in terms of

observable quantities only[2].

In the left panel of Figure 5.4 we plot the relative difference in mass, M^{TC}, of a halo in TianCold and its counterpart halo of mass M^{TN} in TianNu. For now, we restrict attention to only those halos of mass $10^{14} \leq M^{\mathrm{TC}}/M_\odot \leq 2 \times 10^{14}$. Since $\delta_\nu^{\mathrm{rec}}$ is correlated with δ_c^{rec} (regions of higher CDM density also correspond to regions of higher neutrino density), we rescale the x axis so that it represents the relative deviation in $\delta_\nu^{\mathrm{rec}}$ from its expected value given δ_c^{rec}. This is achieved by fitting a linear relationship, $\delta_\nu^{\mathrm{rec}} = A\delta_c^{\mathrm{rec}} + B$, and subtracting this from $\delta_\nu^{\mathrm{rec}}$. Rescaling allows us to compare the change in halos mass as we vary δ_ν with δ_c held fixed.

The most obvious feature in Figure 5.4 is that TianNu halos are systematically less massive than their TianCold counterparts. This is a feedback effect due to the gravitational backreaction of neutrinos delaying the collapse of CDM halos. More importantly, we find a positive slope between the mass difference and neutrino density, as shown by the best-fit red line in Figure 5.4. When we fix the level of CDM clustering (i.e., when we fix δ_c^{rec}), we find the mass difference is smaller in regions of higher neutrino density. Evidently, the enhanced neutrino density contrast in these regions contribute to the gravitational collapse of the halo, driving it closer to its TianCold counterpart. In regions of suppressed neutrino density, the opposite is true and the growth of TianNu halos are increasingly delayed with respect to their TianCold counterpart.

The positive slope in Figure 5.4 is indicative of a non-zero neutrino bias, b_ν. In the right panel of Figure 5.4 we show the slope and intercept of the best-fit line for different bins in halo mass. Points represent median values from 1000 bootstrap realizations of each mass bin while error bars represent the 1σ spread about the median. In analogy to the CDM bias, b_c, we expect b_ν to be a function of halo mass; this is indeed the case. Firstly, the neutrino bias goes to small numbers at low mass. This is simply a reflection of the fact that low-mass halos collapsed at earlier times so their present evolution is strongly driven by CDM with neutrinos playing little role. This is also indicated by the intercept approaching zero as halo mass is decreased. This reasoning was also used before when explaining the upturn seen on small scales in the matter power suppression of Figure 5.2. In contrast, the slope rises with increasing mass and peaks around the scale where halos are forming today. There further appears to be a turnover of the slope on cluster scales though the error bars due to small number statistics are too large to make a meaningful statement here.

The process outlined above is useful in connection to theoretical studies that predict the impact of neutrinos on halo collapse and bias (e.g., LoVerde, 2014). Observationally, however, our procedure is of little use since we do not have access to two universes with counterpart halos to compare. Instead, we propose an alternative method for which the neutrino bias can be observed from just one universe. Suppose we have a galaxy survey from which we identify masses, M, and linearly reconstructed local values of δ_c^{rec} and $\delta_\nu^{\mathrm{rec}}$. As before, we group galaxies into mass bins. Then, in each mass bin, we further group galaxies into different bins in δ_c^{rec}. We are left with a collection of galaxy bins of fixed mass and CDM density. Within each bin,

---

[2]We assume that halo masses can be determined observationally using a proxy such as luminosity.

we find the galaxy with the median value of $\delta_\nu^{\rm rec}$, and denote its mass and neutrino density as $\langle M \rangle$ and $\langle \delta_\nu^{\rm rec} \rangle$, respectively. In a similar manner as Figure 5.4, we collect all $\delta_c^{\rm rec}$ bins in a given mass bin and plot $(M - \langle M \rangle)/M$ versus $\delta_\nu^{\rm rec} - \langle \delta_\nu^{\rm rec} \rangle$. In a universe without neutrinos, we should not observe any correlation between $M - \langle M \rangle$ and $\delta_\nu^{\rm rec} - \langle \delta_\nu^{\rm rec} \rangle$. In a universe with neutrinos, we should observe a positive slope whose value depends in some way on m_ν.

We are currently in the process of testing this procedure using the halo catalogues of Tian-Cold and TianNu. There is some difficulty associated with this method due to the intrinsic stochasticity in halo mass at fixed $\delta_c^{\rm rec}$ and $\delta_\nu^{\rm rec}$. The simple method of choosing $\langle M \rangle$ based on the halo with the median $\delta_\nu^{\rm rec}$ leads to a considerable amount of scatter that complicates the analysis. Some form of smoothing or interpolative procedure for fixing a pivot point will likely resolve this issue.

5.5   Summary

We have completed the world's largest cosmological N-body simulation (TianNu) containing $\sim 2.6 \times 10^{12}$ neutrino plus 3.3×10^{11} CDM particles. The staggering number of neutrino particles is necessary to suppress shot noise due to the thermal motion of $m_\nu = 0.05$ eV neutrinos. We simulate neutrinos at the lower bound of current mass constraints so that our results represent the conservative case where neutrinos have the least impact on structure formation. We also perform a second simulation, TianCold, with identical parameters as TianNu, but containing only CDM. In each simulation, we resolve $\simeq 3 \times 10^7$ halos of mass $M \gtrsim 10^{11}$ $M_\odot/h$ in a volume comparable to an all-sky survey out to $z \approx 0.2$.

We have presented preliminary results from the analysis of our two simulations. We provide results on the suppression of the matter power spectrum on small scales and will compare these against the recent modifications made to HALOFIT by the simulations of Bird et al. (2012). We are working at testing the efficacy of measuring the neutrino dipole distortion from the cross-correlation of low- and high-mass galaxy populations. We have serendipitously discovered the presence of an additional dipole, that dominates over the neutrino signal, and appears to be related to the formation of low- and high-mass halos. If real, this dipole should be detectable in current galaxy surveys, and may be a useful probe of structure formation. For our purposes, this signal represents a contaminant that we are currently working to remove. Finally, we have compared counterpart halos in TianNu and TianCold to provide a measure of neutrino bias. We propose a new method of detecting neutrinos by observing differences in halo mass due to neutrino bias. This method differs from conventional cosmological probes, such as the matter power spectrum, that search for neutrinos by isolating them from the *sum* of the effects of all matter. The neutrino bias approach is based on the relative *difference* between neutrinos while all other matter effects are held constant. This may provide a more systematic probe of cosmological neutrinos.

Chapter 6

Conclusions and Outlook

In this thesis, we used cosmological simulations to study the role of nonlinear structure in an array of astrophysical scenarios. We have made a number of important contributions to the fields of cosmic reionization, galactic substructure evolution, and cosmic neutrinos. The main conclusions of this work are described in detail in the closing sections of Chapters 2 through 5. We provide a brief summary below in relation to the relevant fields of astrophysics.

- **Epoch of reionization**: We have performed a numerical convergence study on the small-scale opacity of the IGM during the onset of reionization. We parameterize the IGM opacity by the mean free path of ionizing radiation, λ, and clumping factor, c_l, of ionized gas. We present converged results for λ and c_l on smaller scales and earlier times than considered before. At early times, the IGM opacity is dominated by small-scale absorption systems collapsing at the Jeans mass. These systems act as important sinks of ionizing photons during the epoch of reionization. We show that hydrodynamic simulations require a CDM particle mass $m_{\rm dm} \lesssim 50\ M_\odot$ and box width $L \gtrsim 1$ Mpc to properly resolve and sample the smallest absorption systems in the IGM. These criteria are relevant to any numerical study that resolves the Jeans scale of the unheated IGM.

- **Galactic substructure evolution**: We have investigated the infall and dynamical evolution of CDM subhalos within a galactic host. We utilize the public data from a cosmological simulation with large dynamic range allowing the study of smaller subhalos than considered before. We find that low-mass subhalos, with mass ratios $\mu \lesssim 10^{-3}$, have qualitatively different evolution than high-mass subhalos, whose fate is mainly driven by dynamical friction. In particular, we find that low-mass subhalo evolution is strongly driven by concentration. Concentration is correlated with the distance at which a subhalo first becomes tidally truncated by the host as well as the rate at which mass is subsequently lost via tidal stripping and heating. Furthermore, the evolution of internal density due to mass loss can be parametrized by concentration in the $v_{\rm max} - r_{\rm max}$ plane. These results point to the existence of a "concentration bias" that may be used to unwind the evolution of ultra-faint dwarf galaxies to their infall on the Milky Way.

- **Cosmic neutrinos:** We have investigated the potential use of cosmological observations to constrain the absolute mass scale of neutrinos. First, is the dipole distortion in the matter density field caused by the bulk flow of neutrinos relative to CDM. This has the potential of being observed in weak lensing surveys or through the cross-correlation of galaxy populations of different mass. The relative velocity field of CDM and neutrinos is required for such observations. We show that this can be accurately reconstructed by applying linear transformations to an observed galaxy field. We have completed the world's largest cosmological N-body simulation containing $\simeq 3 \times 10^{12}$ neutrino plus CDM particles. We are currently working with the simulation data to forecast the ability of upcoming surveys to constrain neutrino mass. This includes the dipole distortion as well as a new method we propose that relies on the neutrino biasing of CDM halos.

6.1   Future Work

The work presented here provides a gateway to an avenue of potential research projects. For starters, a natural extension of our work on the opacity of the unheated IGM is to present converged results for the case where radiative transfer affects the thermal state of the gas. This is a nontrivial task, however, since it requires the use of self-consistent hydrodynamic simulations with radiative transfer and photoionization heating. A simple post-processing scheme applied to a static density field is no longer sufficient in this case. On the other hand, it may be sufficient to incorporate our converged results for the unheated IGM as a subgrid model in a large-scale reionization simulation with some prescription that accounts for photoevaporation as the Jeans scale is raised. In either event, it is important to quantify the total impact that small-scale absorption sinks had on the total ionizing photon budget during reionization.

Our work on galactic substructure evolution hinted at the possibility of using concentration as a predictive indicator of the tidal evolution of low-mass subhalos. This has relevance in near-field cosmology as ultra-faint dwarf galaxies are increasingly observed. In terms of galaxy formation, there is considerable interest in connecting the observed population of dwarf galaxies back to their initial infall on the Milky Way. An application of our work would be to unwind present observations of ultra-faint dwarf galaxies to their initial conditions based on the connection between concentration and tidal evolution.

We presently have ongoing work in the analysis of our TianNu simulation. This includes investigation of the neutrino dipole, matter power suppression, and neutrino biasing. On another front, we are testing a scheme to effectively simulate multiple mass eigenstates at once using a reweighing of the final velocity distribution. Neutrino cosmology is becoming an important field as upcoming observations are expected to measure structure formation with unprecedented levels of precision. Matching this precision from theoretical predictions requires the proper simulation of nonlinear neutrino structure formation. We will thus have a plethora of cosmic neutrino research opportunities in the future.

Bibliography

Abel, T., Bryan, G. L., & Norman, M. L. 2002, Science, 295, 93

Abel, T., Wise, J. H., & Bryan, G. L. 2007, ApJ, 659, L87

Agostini, M., Allardt, M., Andreotti, E., et al. 2013, Physical Review Letters, 111, 122503

Ahmad, Q. R., Allen, R. C., Andersen, T. C., et al. 2002, Physical Review Letters, 89, 011301

Ali-Haïmoud, Y., & Bird, S. 2013, MNRAS, 428, 3375

Alvarez, M. A., & Abel, T. 2012, ApJ, 747, 126

Alvarez, M. A., Bromm, V., & Shapiro, P. R. 2006, ApJ, 639, 621

Alvarez, M. A., Busha, M., Abel, T., & Wechsler, R. H. 2009, ApJ, 703, L167

Alvarez, M. A., Finlator, K., & Trenti, M. 2012, ApJ, 759, L38

Amendola, L., Appleby, S., Bacon, D., et al. 2013, Living Reviews in Relativity, 16, 6

Aubert, D., & Teyssier, R. 2010, ApJ, 724, 244

Barkana, R., & Loeb, A. 1999, ApJ, 523, 54

—. 2001, Phys. Rep., 349, 125

—. 2004, ApJ, 609, 474

Battaglia, N., Trac, H., Cen, R., & Loeb, A. 2013, ApJ, 776, 81

Becker-Szendy, R., Bratton, C. B., Casper, D., et al. 1992, Phys. Rev. D, 46, 3720

Behroozi, P. S., Wechsler, R. H., Lu, Y., et al. 2014, ApJ, 787, 156

Benson, A. J. 2005, MNRAS, 358, 551

Binney, J., & Tremaine, S. 1987, Galactic dynamics

Bird, S., Viel, M., & Haehnelt, M. G. 2012, MNRAS, 420, 2551

Blas, D., Lesgourgues, J., & Tram, T. 2011, J. Cosmology Astropart. Phys., 7, 34

Bolton, J. S., & Haehnelt, M. G. 2007, MNRAS, 382, 325

Bond, J. R., Cole, S., Efstathiou, G., & Kaiser, N. 1991, ApJ, 379, 440

Bouwens, R. J., Illingworth, G. D., Oesch, P. A., et al. 2010, ApJ, 709, L133

Boylan-Kolchin, M., Ma, C.-P., & Quataert, E. 2008, MNRAS, 383, 93

Boylan-Kolchin, M., Springel, V., White, S. D. M., & Jenkins, A. 2010, MNRAS, 406, 896

Boylan-Kolchin, M., Springel, V., White, S. D. M., Jenkins, A., & Lemson, G. 2009, MNRAS, 398, 1150

Brandbyge, J., & Hannestad, S. 2009, J. Cosmology Astropart. Phys., 5, 2

—. 2010, J. Cosmology Astropart. Phys., 1, 21

Brandbyge, J., Hannestad, S., Haugbølle, T., & Thomsen, B. 2008, J. Cosmology Astropart. Phys., 8, 20

Bromm, V., Coppi, P. S., & Larson, R. B. 2002, ApJ, 564, 23

Bryan, G. L., & Norman, M. L. 1998, ApJ, 495, 80

Bryan, G. L., Norman, M. L., O'Shea, B. W., et al. 2014, ApJS, 211, 19

Castorina, E., Sefusatti, E., Sheth, R. K., Villaescusa-Navarro, F., & Viel, M. 2014, J. Cosmology Astropart. Phys., 2, 49

Chandrasekhar, S. 1943, ApJ, 97, 255

Chiu, W. A., Fan, X., & Ostriker, J. P. 2003, ApJ, 599, 759

Choudhury, T. R., Haehnelt, M. G., & Regan, J. 2009, MNRAS, 394, 960

Ciardi, B., Scannapieco, E., Stoehr, F., et al. 2006, MNRAS, 366, 689

Ciardi, B., Stoehr, F., & White, S. D. M. 2003, MNRAS, 343, 1101

Cleveland, B. T., Daily, T., Davis, Jr., R., et al. 1998, ApJ, 496, 505

Cooray, A., & Sheth, R. 2002, Phys. Rep., 372, 1

Costanzi Alunno Cerbolini, M., Sartoris, B., Xia, J.-Q., et al. 2013, J. Cosmology Astropart. Phys., 6, 20

Couchman, H. M. P., & Rees, M. J. 1986, MNRAS, 221, 53

de Putter, R., Mena, O., Giusarma, E., et al. 2012, ApJ, 761, 12

Diemand, J., Kuhlen, M., & Madau, P. 2006, ApJ, 649, 1

—. 2007a, ApJ, 657, 262

—. 2007b, ApJ, 667, 859

Diemand, J., Kuhlen, M., Madau, P., et al. 2008, Nature, 454, 735

Dodelson, S. 2003, Modern cosmology

Eitel, K. 2005, Nuclear Physics B Proceedings Supplements, 143, 197

Emberson, J. D., Kobayashi, T., & Alvarez, M. A. 2015, ApJ, 812, 9

Emberson, J. D., Thomas, R. M., & Alvarez, M. A. 2013, ApJ, 763, 146

Fan, X., Strauss, M. A., Becker, R. H., et al. 2006, AJ, 132, 117

Finlator, K., Oh, S. P., Özel, F., & Davé, R. 2012, ArXiv e-prints, arXiv:1209.2489

Finlator, K., Özel, F., Davé, R., & Oppenheimer, B. D. 2009, MNRAS, 400, 1049

Fogli, G. L., Lisi, E., Marrone, A., et al. 2012, Phys. Rev. D, 86, 013012

Furlanetto, S. R., Zaldarriaga, M., & Hernquist, L. 2004, ApJ, 613, 1

Gan, J., Kang, X., van den Bosch, F. C., & Hou, J. 2010, MNRAS, 408, 2201

Garrison-Kimmel, S., Boylan-Kolchin, M., Bullock, J. S., & Lee, K. 2014, MNRAS, 438, 2578

Geil, P. M., & Wyithe, J. S. B. 2008, MNRAS, 386, 1683

Ghigna, S., Moore, B., Governato, F., et al. 1998, MNRAS, 300, 146

Giocoli, C., Tormen, G., & van den Bosch, F. C. 2008, MNRAS, 386, 2135

Gnedin, N. Y. 2000, ApJ, 535, 530

Gnedin, N. Y., & Fan, X. 2006, ApJ, 648, 1

Gnedin, N. Y., & Hui, L. 1998, MNRAS, 296, 44

Gnedin, N. Y., & Ostriker, J. P. 1997, ApJ, 486, 581

Greif, T. H., Johnson, J. L., Klessen, R. S., & Bromm, V. 2008, MNRAS, 387, 1021

Gunn, J. E., & Peterson, B. A. 1965, ApJ, 142, 1633

Haardt, F., & Madau, P. 1996, ApJ, 461, 20

Hahn, O., Angulo, R. E., & Abel, T. 2014, ArXiv e-prints, arXiv:1404.2280

Hahn, O., Porciani, C., Dekel, A., & Carollo, C. M. 2009, MNRAS, 398, 1742

Haiman, Z. 2011, Nature, 472, 47

Haiman, Z., Abel, T., & Madau, P. 2001, ApJ, 551, 599

Haiman, Z., Abel, T., & Rees, M. J. 2000, ApJ, 534, 11

Harnois-Déraps, J., Pen, U.-L., Iliev, I. T., et al. 2013, MNRAS, 436, 540

Hayashi, E., Navarro, J. F., Taylor, J. E., Stadel, J., & Quinn, T. 2003, ApJ, 584, 541

Hinshaw, G., Larson, D., Komatsu, E., et al. 2013, ApJS, 208, 19

Hirata, K. S., Inoue, K., Ishida, T., et al. 1992, Physics Letters B, 280, 146

Hockney, R. W., & Eastwood, J. W. 1988, Computer simulation using particles

Iliev, I. T., Mellema, G., Pen, U.-L., et al. 2006, MNRAS, 369, 1625

Iliev, I. T., Scannapieco, E., & Shapiro, P. R. 2005a, ApJ, 624, 491

Iliev, I. T., Shapiro, P. R., & Raga, A. C. 2005b, MNRAS, 361, 405

Inman, D., Emberson, J. D., Pen, U.-L., et al. 2015, Phys. Rev. D, 92, 023502

Jiang, C. Y., Jing, Y. P., Faltenbacher, A., Lin, W. P., & Li, C. 2008, ApJ, 675, 1095

Jiang, F., & van den Bosch, F. C. 2014a, MNRAS, 440, 193

—. 2014b, ArXiv e-prints, arXiv:1403.6827

Jiang, L., Cole, S., Sawala, T., & Frenk, C. S. 2015, MNRAS, 448, 1674

Johnson, J. L., Greif, T. H., & Bromm, V. 2007, ApJ, 665, 85

Kamionkowski, M., & Liddle, A. R. 2000, Physical Review Letters, 84, 4525

Kaurov, A. A., & Gnedin, N. Y. 2014, ApJ, 787, 146

Kazantzidis, S., Mayer, L., Mastropietro, C., et al. 2004, ApJ, 608, 663

Keeton, C. R., & Moustakas, L. A. 2009, ApJ, 699, 1720

Khochfar, S., & Burkert, A. 2006, A&A, 445, 403

Klypin, A., Kravtsov, A. V., Bullock, J. S., & Primack, J. R. 2001, ApJ, 554, 903

Klypin, A., Kravtsov, A. V., Valenzuela, O., & Prada, F. 1999, ApJ, 522, 82

Klypin, A. A., Trujillo-Gomez, S., & Primack, J. 2011, ApJ, 740, 102

Komatsu, E., Smith, K. M., Dunkley, J., et al. 2011, ApJS, 192, 18

Kraus, C., Bornschein, B., Bornschein, L., et al. 2005, European Physical Journal C, 40, 447

Kravtsov, A. V., Gnedin, O. Y., & Klypin, A. A. 2004, ApJ, 609, 482

Kuhlen, M., & Faucher-Giguère, C.-A. 2012, MNRAS, 423, 862

Lacey, C., & Cole, S. 1993, MNRAS, 262, 627

Lesgourgues, J., & Pastor, S. 2006, Phys. Rep., 429, 307

Lewis, A., Challinor, A., & Lasenby, A. 2000, ApJ, 538, 473

Li, Y., & Mo, H. 2009, ArXiv e-prints, arXiv:0908.0301

Loken, C., Gruner, D., Groer, L., et al. 2010, Journal of Physics Conference Series, 256, 012026

Lovell, M. R., Eke, V., Frenk, C. S., et al. 2012, MNRAS, 420, 2318

LoVerde, M. 2014, Phys. Rev. D, 90, 083518

LSST Dark Energy Science Collaboration. 2012, ArXiv e-prints, arXiv:1211.0310

Ludlow, A. D., Navarro, J. F., Springel, V., et al. 2009, ApJ, 692, 931

Madau, P., Haardt, F., & Rees, M. J. 1999, ApJ, 514, 648

Mangano, G., Miele, G., Pastor, S., et al. 2005, Nuclear Physics B, 729, 221

Massara, E., Villaescusa-Navarro, F., & Viel, M. 2014, J. Cosmology Astropart. Phys., 12, 53

McQuinn, M., Oh, S. P., & Faucher-Giguère, C.-A. 2011, ApJ, 743, 82

Mesinger, A., Ferrara, A., Greig, B., et al. 2015, Advancing Astrophysics with the Square Kilometre Array (AASKA14), 11

Mesinger, A., & Furlanetto, S. 2007, ApJ, 669, 663

Mikheyev, S. P., & Smirnov, A. Y. 1985, Sov. J. Nucl. Phys., 42, 913

Mirabel, I. F., Dijkstra, M., Laurent, P., Loeb, A., & Pritchard, J. R. 2011, A&A, 528, A149

Miralda-Escudé, J., Haehnelt, M., & Rees, M. J. 2000, ApJ, 530, 1

Moore, B., Ghigna, S., Governato, F., et al. 1999, ApJ, 524, L19

Navarro, J. F., Frenk, C. S., & White, S. D. M. 1995, MNRAS, 275, 56

—. 1997, ApJ, 490, 493

Oesch, P. A., Bouwens, R. J., Illingworth, G. D., et al. 2012, ApJ, 745, 110

Oh, S. P., & Haiman, Z. 2003, MNRAS, 346, 456

Pawlik, A. H., Schaye, J., & van Scherpenzeel, E. 2009, MNRAS, 394, 1812

Peñarrubia, J., Benson, A. J., Walker, M. G., et al. 2010, MNRAS, 406, 1290

Peñarrubia, J., Navarro, J. F., & McConnachie, A. W. 2008, ApJ, 673, 226

Peebles, P. J. E. 1980, The large-scale structure of the universe

Peebles, P. J. E., & Dicke, R. H. 1968, ApJ, 154, 891

Pieri, L., Bertone, G., & Branchini, E. 2008, MNRAS, 384, 1627

Planck Collaboration, Ade, P. A. R., Aghanim, N., et al. 2015, ArXiv e-prints, arXiv:1502.01589

Pontecorvo, B. 1958, Sov. Phys. JETP, 6, 429

Prochaska, J. X., O'Meara, J. M., & Worseck, G. 2010, ApJ, 718, 392

Pueblas, S., & Scoccimarro, R. 2009, Phys. Rev. D, 80, 043504

Pullen, A. R., Benson, A. J., & Moustakas, L. A. 2014, ArXiv e-prints, arXiv:1407.8189

Reed, D. S., Bower, R., Frenk, C. S., Jenkins, A., & Theuns, T. 2007, MNRAS, 374, 2

Ricotti, M., & Ostriker, J. P. 2004, MNRAS, 352, 547

Ricotti, M., Ostriker, J. P., & Gnedin, N. Y. 2005, MNRAS, 357, 207

Ringwald, A., & Wong, Y. Y. Y. 2004, J. Cosmology Astropart. Phys., 12, 5

Sales, L. V., Navarro, J. F., Abadi, M. G., & Steinmetz, M. 2007, MNRAS, 379, 1475

Santos, M. G., Ferramacho, L., Silva, M. B., Amblard, A., & Cooray, A. 2010, MNRAS, 406, 2421

Scherrer, R. J., & Bertschinger, E. 1991, ApJ, 381, 349

Schneider, P. 2006, Extragalactic Astronomy and Cosmology

Shapiro, P. R., & Giroux, M. L. 1987, ApJ, 321, L107

Shapiro, P. R., Giroux, M. L., & Babul, A. 1994, ApJ, 427, 25

Shapiro, P. R., Iliev, I. T., & Raga, A. C. 2004, MNRAS, 348, 753

Shull, J. M., Harness, A., Trenti, M., & Smith, B. D. 2012, ApJ, 747, 100

Slater, C. T., & Bell, E. F. 2013, ApJ, 773, 17

Smith, R. E., Peacock, J. A., Jenkins, A., et al. 2003, MNRAS, 341, 1311

So, G. C., Norman, M. L., Reynolds, D. R., & Wise, J. H. 2014, ApJ, 789, 149

Sobacchi, E., & Mesinger, A. 2014, MNRAS, 440, 1662

Spergel, D. N., Bean, R., Doré, O., et al. 2007, ApJS, 170, 377

Springel, V. 2005, MNRAS, 364, 1105

Springel, V., White, S. D. M., Tormen, G., & Kauffmann, G. 2001, MNRAS, 328, 726

Springel, V., Wang, J., Vogelsberger, M., et al. 2008, MNRAS, 391, 1685

Storrie-Lombardi, L. J., McMahon, R. G., Irwin, M. J., & Hazard, C. 1994, ApJ, 427, L13

Taffoni, G., Mayer, L., Colpi, M., & Governato, F. 2003, MNRAS, 341, 434

Taylor, J. E., & Babul, A. 2004, MNRAS, 348, 811

Tegmark, M., Silk, J., Rees, M. J., et al. 1997, ApJ, 474, 1

The Exo-200 Collaboration, Albert, J. B., Auty, D. J., et al. 2014, Nature, 510, 229

Tormen, G. 1997, MNRAS, 290, 411

Trac, H., Cen, R., & Loeb, A. 2008, ApJ, 689, L81

Trenti, M., Stiavelli, M., Bouwens, R. J., et al. 2010, ApJ, 714, L202

Tseliakhovich, D., & Hirata, C. 2010, Phys. Rev. D, 82, 083520

van den Bosch, F. C., & Jiang, F. 2014, ArXiv e-prints, arXiv:1403.6835

van den Bosch, F. C., Tormen, G., & Giocoli, C. 2005, MNRAS, 359, 1029

Viel, M., Haehnelt, M. G., & Springel, V. 2010, J. Cosmology Astropart. Phys., 6, 15

Villaescusa-Navarro, F., Bird, S., Peña-Garay, C., & Viel, M. 2013, J. Cosmology Astropart. Phys., 3, 19

Wang, H. Y., Jing, Y. P., Mao, S., & Kang, X. 2005, MNRAS, 364, 424

Wang, Y., & Xing, Z.-z. 2015, ArXiv e-prints, arXiv:1504.06155

Warren, M. S., Abazajian, K., Holz, D. E., & Teodoro, L. 2006, ApJ, 646, 881

Wechsler, R. H., Bullock, J. S., Primack, J. R., Kravtsov, A. V., & Dekel, A. 2002, ApJ, 568, 52

Weinberg, D. H., Bullock, J. S., Governato, F., Kuzio de Naray, R., & Peter, A. H. G. 2013, ArXiv e-prints, arXiv:1306.0913

Wetzel, A. R. 2011, MNRAS, 412, 49

Wetzel, A. R., Deason, A. J., & Garrison-Kimmel, S. 2015, ArXiv e-prints, arXiv:1501.01972

Wise, J. H., & Abel, T. 2008, ApJ, 685, 40

Wise, J. H., & Cen, R. 2009, ApJ, 693, 984

Wise, J. H., Turk, M. J., Norman, M. L., & Abel, T. 2012, ApJ, 745, 50

Wolfenstein, L. 1978, Phys. Rev. D, 17, 2369

Xia, J.-Q., Granett, B. R., Viel, M., et al. 2012, J. Cosmology Astropart. Phys., 6, 10

Yang, X., Mo, H. J., Zhang, Y., & van den Bosch, F. C. 2011, ApJ, 741, 13

Yoshida, N., Abel, T., Hernquist, L., & Sugiyama, N. 2003, ApJ, 592, 645

Yoshida, N., Oh, S. P., Kitayama, T., & Hernquist, L. 2007, ApJ, 663, 687

Zahn, O., Zaldarriaga, M., Hernquist, L., & McQuinn, M. 2005, ApJ, 630, 657

Zel'dovich, Y. B. 1970, A&A, 5, 84

Zemp, M., Diemand, J., Kuhlen, M., et al. 2009, MNRAS, 394, 641

Zentner, A. R., Berlind, A. A., Bullock, J. S., Kravtsov, A. V., & Wechsler, R. H. 2005, ApJ, 624, 505

Zhang, P., Zheng, Y., & Jing, Y. 2015, Phys. Rev. D, 91, 043522

Zheng, Y., Zhang, P., & Jing, Y. 2015, Phys. Rev. D, 91, 043523

Zhu, H.-M., Pen, U.-L., Chen, X., & Inman, D. 2014a, ArXiv e-prints, arXiv:1412.1660

Zhu, H.-M., Pen, U.-L., Chen, X., Inman, D., & Yu, Y. 2014b, Physical Review Letters, 113, 131301